Report
R-19-15
May 2020

Reactive transport modelling of montmorillonite dissolution

Report for the safety evaluation SE-SFL

Andrés Idiart
Marcelo Laviña
Fidel Grandia
Arnau Pont

SVENSK KÄRNBRÄNSLEHANTERING AB

SWEDISH NUCLEAR FUEL
AND WASTE MANAGEMENT CO

Box 3091, SE-169 03 Solna
Phone +46 8 459 84 00
skb.se

SVENSK KÄRNBRÄNSLEHANTERING

ISSN 1402-3091
SKB R-19-15
ID 1668830
May 2020

Reactive transport modelling of montmorillonite dissolution

Report for the safety evaluation SE-SFL

Andrés Idiart, Marcelo Laviña, Fidel Grandia, Arnau Pont
Amphos 21 Consulting S.L.

Summary

A study of the alteration of the bentonite backfill of the BHA vault in the SFL repository by the interaction with cementitious materials is presented. Two sets of 1D reactive transport models of bentonite degradation in the BHA vault are developed and implemented using iCP, an interface between Comsol Multiphysics and Phreeqc. The first set considers only the bentonite system, treating concrete as a boundary condition. The second set explicitly considers the interaction between the concrete and bentonite barriers. The BHA vault is one of the two main vaults of the proposed repository for long-lived low- and intermediate-level waste in Sweden (for storage of legacy waste and waste from non-nuclear facilities). The goal of the work is to assess the extent of montmorillonite dissolution in the bentonite barrier as a result of the interaction with the cementitious fluids from the concrete barrier over a time span of 100 000 years. The analysis starts with an idealized case in which only montmorillonite is considered to gain system understanding. Thereafter, a reference case is formulated, conceptualized and implemented based on what is thought to be a plausible scenario. In addition, a number of sensitivity analyses are presented to assess the impact of several uncertain parameters on the results, including among others the reactive surface area of montmorillonite in compacted bentonite. Finally, analytical models, based on the shrinking core model, that predict the dissolution depth, are also discussed and compared with reactive transport results. The implications of the results and the model outcomes and limitations in the context of repository performance are discussed. All the models that consider the most probable setup of the system predict a significant dissolution of montmorillonite, of between 20 and 70 % of the initial montmorillonite mass. However, recent studies of the reactive surface area of montmorillonite in compacted bentonite in the dry density range of interest to repository conditions suggest that this parameter may be lower than expected. Results of the reactive transport models that assume reactive surface areas derived from these studies indicate a significant reduction of montmorillonite dissolution.

Sammanfattning

Det föreslagna slutförvaret, SFL, för långlivat, lågt- och medelaktivt avfall som ska förvara historiskt avfall och avfall från icke-nukleära anläggningar i Sverige, utgörs av två bergssalar, en av dessa är BHA-salen. I denna rapport presenteras en studie av den bentonitomvandling (med fokus på mineralet montmorillonit) som kan förväntas ske till följd av interaktioner mellan bentonit- och betongbarriären som omsluter avfallsbehållarna i BHA-salen. För studien har två uppsättningar av endimensionella reaktiva transportmodeller utvecklats och implementerats med hjälp av iCP, ett gränssnitt mellan programmen Comsol Multiphysics och Phreeqc. I den första modelluppsättningen behandlas bentonitdomänen explicit medan betongstrukturens inverkan studeras genom implementering av randvillkor. I den andra modelluppsättningen behandlas både betong- och bentonitdomänen explicit för att studera fullständig interaktion. Syftet är att bedöma andelen montmorillonit i bentonitbarriären som omvandlas till följd av interaktionen med betongjämnviktad formationsvätska under tidsperioden 100 000 år. För systemförståelse inleds studien med ett idealiserat fall där enbart montmorillonit beaktas i frånvaro av sekundära mineraler. Därefter formuleras, konceptualiseras och implementeras ett referensfall som kan anses vara en mer trolig utveckling. Utöver detta har känslighetsanalyser genomförts för att studera parameterosäkerhet. Slutligen jämförs numeriska resultat med analytiska lösningar för penetrationsdjup. Implikationer av resultaten samt eventuella modellbegränsningar diskuteras utifrån förvarets tänkta funktion. Modellerna med realistiska antaganden predikterar en relativt omfattande omvandling av montmorillonit i bentonitbarriären på i storleksordningen 20–70 % av den ursprungliga massan efter 100 000 år. Nyligen genomförda studier tyder på att den reaktiva ytan för montmorillonit i kompakterad bentonit (vid den torrdensitet som förväntas under förvarshållanden) kan vara mycket lägre än vad som tidigare antagits. Resultaten från de reaktiva transportmodellerna där detta beaktats visar en signifikant reduktion av andelen montmorillonit som löses upp.

Contents

1 Introduction

SKB plans to dispose of long-lived low- and intermediate-level waste (LILW) in a deep geological repository, named SFL. The total capacity of SFL is estimated to approximately 16 000 m^3. About one third of the waste volume originates from nuclear power plants in the form of neutron-irradiated components and control rods. The remainder comes from AB SVAFO and Studsvik Nuclear AB, who manage the legacy waste and the waste from hospitals, industry and research. Possible repository concepts for SFL have been evaluated and Elfwing et al. (2013) proposed a repository concept to be analysed in an evaluation of post-closure safety (SE-SFL). This study focusses on the repository concept denoted as BHA. The main component of the engineered barrier system is a bentonite backfill that surrounds a concrete structure containing the waste (see Section 4).

Understanding of the degradation rates and long-term performance of the bentonite and concrete structures are of key importance for assessment of the long-term (10^5–10^6 years) safety of the SFL repository. Concrete degradation can induce a high-pH plume (pH > 11) that could impair the performance of bentonite in the BHA vault (e.g. Karnland and Birgersson 2006).

Montmorillonite is the main mineral forming the bentonite that is planned to be used in SFL, with a content above 80 wt% (MX-80 bentonite). The stability of this mineral decreases in contact with high pH fluids, meaning that dissolution kinetics significantly increases with pH (e.g. Cama et al. 2000, Gaucher and Blanc 2006). In addition, the dissolution rate also depends strongly on temperature. Even with the exhaustive research conducted in recent years to determine the rate of dissolution of montmorillonite, inconsistencies between published rates remain in literature. This causes uncertainty in the predictive models of the long-term stability of bentonite barriers. A recent and comprehensive review of clay mineral dissolution kinetics can be found in Cama and Ganor (2015). Moreover, the reactive surface area of montmorillonite that is used to ultimately calculate the dissolved mass is also subject to uncertainties in compacted bentonite systems.

A large body of literature has been produced in the last decades concerning the modelling of alkaline perturbation of bentonite and other clayey materials. Reviews by Gaucher and Blanc (2006), Savage et al. (2007), and Bildstein and Claret (2015) are comprehensive studies of the present level of knowledge and main uncertainties in this field. Most of the studies published in the past on bentonite alteration by alkaline fluids have focused on the bentonite system, disregarding the interaction with a cementitious barrier (Savage et al. 2002, 2010, Gaucher et al. 2004, Watson et al. 2007, 2009, Lehikoinen 2009, Fernández et al. 2010). In those studies, the cementitious system is typically replaced by a fixed (concrete-equilibrated porewater) concentration boundary condition. This is also considered in the first part of the present work and is presented here as the simplified analysis (Section 6).

Early attempts are summarized in Savage et al. (2002) and references therein. In that work, classical transition-state-theory (TST) was used to simulate the kinetic dissolution of montmorillonite, based on Cama and Ayora (1998). A similar kinetic rate law was used by Fernández et al. (2010) to study the interaction of a Mg-saturated FEBEX bentonite and an alkaline solution. Watson et al. (2009) further studied the kinetic dissolution by comparing the results obtained with different rate expression: a TST model, the rate expression by Sato et al. (2004) and that of Yamaguchi et al. (2007). Lehikoinen (2009) modelled the evolution of the bentonite buffer of the Finish repository concept for spent fuel using reactive transport and assuming a kinetic rate of montmorillonite dissolution based on Rozalén et al. (2008). Marty et al. (2014) presented a systematic study of the interaction between a Callovo-Oxfordian clay formation and a high-pH concrete using an expression of the montmorillonite kinetic rate that takes into account the dependence of pH, temperature and the degree of saturation.

Other research studies have focused on the prediction of the formation of the hyperalkaline plume, ultimately reaching the bentonite (e.g. Soler et al. 2011, Grandia et al. 2010, Koskinen 2014, Sidborn et al. 2014), or the degradation of cementitious systems by clayey porewaters (Olmeda et al. 2017).

More recently, the simultaneous interaction between bentonite or clayey materials and cement-based materials such as concrete have been given more attention (De Windt et al. 2004, 2008, Gaucher et al. 2005, Luna et al. 2006, Trotignon et al. 2006, Marty et al. 2009, 2014, Kosakowski and Berner 2013, Soler 2013, Liu et al. 2014, Mon et al. 2017, Idiart et al. 2020). Previous efforts of SKB to

model montmorillonite dissolution have focused on the evolution of bentonite of the Silo of the SFR repository, including the concrete barrier (Gaucher et al. 2005, Cronstrand 2016). Whereas Gaucher et al. (2005) modelled montmorillonite dissolution at thermodynamic equilibrium, the more recent work of Cronstrand (2016) considers kinetically controlled dissolution based on the rate proposed by Rozalén et al. (2008).

The overall concrete degradation sequence is well-known (Miller et al. 2000, Olmeda et al. 2017, Marty et al. 2014). Starting from the intact OPC cementitious material after hydration, the pH decreases following, first, sodium and potassium alkali leaching from the porewater. This is followed by portlandite dissolution and progressive decalcification of the initially high Ca/Si ratio C-S-H gels. This concrete degradation sequence is also observed as a result of the interaction with bentonite (De Windt et al. 2004, Gaucher et al. 2005). Other primary minerals of the cementitious matrix are also dissolved as a result of the interaction with bentonite: hydrogarnet (Gaucher et al. 2005), hydrotalcite (De Windt et al. 2004) and monocarboaluminate (Marty et al. 2014). The higher sulphate content in the clayey materials with respect to concrete can lead to the reprecipitation of ettringite (Marty et al. 2014, Gaucher et al. 2005). Secondary minerals expected to form are calcite (De Windt et al. 2004), magnesium phyllosilicates (Read et al. 2001), saponites (Marty et al. 2014) or sodium phillipsite (Gaucher et al. 2005).

2 Objectives and scope

The main objective of the present study is to predict the long-term (100 000 years) stability of montmorillonite under repository conditions, i.e. at 15 ºC and exposed to a hyperalkaline plume originating from the cementitious domains (waste domain and concrete structure). The model must consider relevant parameterization of the engineered barrier in terms of mineralogical composition, physical properties (porosity, dry density, diffusivity), kinetic and thermodynamic data, and surface area.

First, a set of models are developed that focus on the bentonite barrier, treating the cementitious system as a boundary condition. Upper bounds of montmorillonite dissolution depth are expected to be obtained with this assumption. The reason is that the diffusion resistance of the concrete barriers is not considered in the model and the fact that a finite volume of cement hydrates available for dissolution is not taken into account.

Under more realistic conditions, the cementitious waste domain should act as a barrier for alkaline fluids to reach the bentonite backfill. Thus, a second set of models is also developed here, where the cement-based materials are also included, focusing on both sides of the concrete-bentonite interface.

For these two concepts of the system, an idealized case, where only montmorillonite is considered in the bentonite backfill, and a reference case, considering more realistic conditions, are proposed and implemented. The reference case is based on what is thought to be a plausible scenario according to up-to-date knowledge of the system (geometry, physical properties of the barriers, geochemical model of bentonite, secondary minerals, etc). Given the relatively high level of uncertainty in some of these parameters and variables, a set of sensitivity analyses is proposed to assess the impact on the results for both models.

3 Methodology

Due to the strong dependence of the dissolution kinetic rate of montmorillonite on pH, the alteration of bentonite in the BHA vault will be mainly driven by the interaction with concrete porewater. On the other hand, interaction with circumneutral-pH groundwater over a time span of 100 000 years is not expected to impair the stability of montmorillonite, since the dissolution kinetics is too slow. To simulate the interaction of bentonite with an alkaline plume, a 1D reactive transport model of the BHA bentonite backfill has been developed and implemented in iCP (Nardi et al. 2014), an interface between Comsol (2015) and Phreeqc (Parkhurst and Appelo 2013). The reactive transport code PHAST (Parkhurst et al. 2010) has also been used as a verification exercise. The simulated geometry depends on the conceptualization of the system. The full analysis considers explicitly the cement-based materials (waste domain and concrete structure) together with the bentonite backfill. The model assumes both kinetically controlled and thermodynamic equilibrium chemical reactions.

Solute transport is diffusion-driven, based on a Fickian approach with a single bulk porosity. This assumption is valid since the repository is expected to be water saturated in a time scale that is much shorter than the expected dissolution rates of montmorillonite. Once saturated, solute transport is mainly driven by diffusion due to the very low permeability of the bentonite backfill. Degradation of the concrete domains determines the alkaline water interacting with the bentonite backfill.

As a simplified analysis, the cementitious system is replaced by a fixed concentration boundary condition, thus only representing the bentonite domain explicitly in the model. The composition of the cementitious porewater at the boundary is determined by equilibrium with portlandite.

The dissolution of montmorillonite is set as a kinetically controlled reaction. The implemented dissolution rate is the so-called ‘Sato-Oda’ rate expression (Nakabayashi 2014), which considers the dependency on pH, temperature, and the proximity to thermodynamic equilibrium. In the full analysis, all chemical reactions in the cement-based materials are considered under thermodynamic equilibrium.

The dissolution of bentonite minerals depends on several factors. The relative importance of these factors, especially those that are subject to a high degree of uncertainty, is studied through a set of sensitivity cases. The parameters that have been analysed are the effective diffusion coefficient of aqueous species in the bentonite barrier and concrete domain, the reactive montmorillonite surface area, the set of primary and secondary minerals (see e.g. Savage et al. 2007), the concrete porewater composition, bentonite chemical composition and boundary condition at the rock-bentonite interface. A total of twenty-one (21) reactive transport simulation cases have been implemented and the results of the simplified and full analyses are presented in Section 6 and Section 7, respectively.

Table 3-1 and Table 3-2 list the different cases and present their differences with respect to the conceptual model proposed as reference case (Section 4), both for the simplified and full analysis. Table 3-3 and Table 3-4 show the mineralogical phase assemblage implemented in each simulation case.

Table 3-1. Backfill only models (simplified analysis): set of simulation cases and main differences with respect to the simplified reference case (case 2). Boundary conditions are detailed in Section 6.

Nº	Model Description	D_e (m^2/s) in bentonite	Specific Surface Area (m^2/g)	Mineral assemblage	Left boundary condition	Right boundary condition
1	Idealized case: montmorillonite-only (no secondary minerals allowed to form)	1.2×10^{-10}	800	B	Portlandite equilibrated water	Closed boundary
2	Simplified reference case	1.2×10^{-10}	800	A	Portlandite equilibrated water	Closed boundary
3	Reduced effective diffusion coefficient (D_e)	1.0×10^{-11}	800	A	Portlandite equilibrated water	Closed boundary
4	Reduced specific surface area (SSA)	1.2×10^{-10}	30	A	Portlandite equilibrated water	Closed boundary
5	Reduced specific surface area (SSA = 0.03 m^2/g) (Terada et al. 2019)	1.2×10^{-10}	0.03	A	Portlandite equilibrated water	Closed boundary
6	Reduced D_e and SSA	1.0×10^{-11}	30	A	Portlandite equilibrated water	Closed boundary
7	Fixed groundwater concentration at right rock-bentonite interface	1.2×10^{-10}	800	A	Portlandite equilibrated water	SFL groundwater composition
8	Fixed C-S-H porewater composition at concrete–bentonite interface	1.2×10^{-10}	800	A	C-S-H equilibrated water	Closed boundary
9	Including C-S-H phases as crystalline analogues in the set of secondary minerals	1.2×10^{-10}	800	C	Portlandite equilibrated water	Closed boundary
10	No reactions concerning illite	1.2×10^{-10}	800	D	Portlandite equilibrated water	Closed boundary
11	Addition of Soler and Mäder (2010) secondary phases	1.2×10^{-10}	800	E	Portlandite equilibrated water	Closed boundary
12	Montmorillonite dissolution under thermodynamic equilibrium	1.2×10^{-10}	Thermodynamic equilibrium	A	Portlandite equilibrated water	Closed boundary

Table 3-2. Concrete–bentonite models (full analysis): set of simulation cases and main differences with respect to the full reference case (case 14). Boundary conditions are detailed in Section 4 and Table 7-1.

Nº	Model Description	D_e (m^2/s) in concrete	Mineral assemblage	Concrete domains chemical description	Bentonite backfill chemical description
13	Idealized case: montmorillonite-only (no secondary minerals)	3.50×10^{-12}	b	Full case composition	Only mineral description
14	Full reference case (considering concrete–bentonite interaction)	3.50×10^{-12}	f	Full case composition	Full case composition
15	Full reference case (considering concrete–bentonite interaction and SSA = 0.03 m^2/g) (Terada et al. 2019)	3.50×10^{-12}	f	Full case composition	Full case composition
16	Reduced effective diffusion coefficient (D_e)	1.00×10^{-12}	f	Full case composition	Full case composition
17	Increased effective diffusion coefficient (D_e)	3.50×10^{-11}	f	Full case composition	Full case composition
18	Alkali leached concrete	3.50×10^{-12}	f	Alkali leached concrete	Full case composition
19	No waste domain	3.50×10^{-12}	f	No waste domain considered	Full case composition
20	No bentonite exchanger	3.50×10^{-12}	f	Full case composition	No exchanger included
21	Alternative secondary zeolites	3.50×10^{-12}	g	Full case composition	Change in secondary phases

Table 3-3. Description of minerals included in each simulation case.

ID	Set of minerals
a	Simplified reference case (see Table 3-4)
b	Only Montmorillonite, no secondary minerals allowed to precipitate
c	Crystalline C-S-H phases instead of amorphous gels
d	No illite in primary or secondary mineral paragenesis
e	Set of minerals presented in Soler and Mäder (2010)
f	Full reference case (see Table 4-6)
g	Set of zeolites presented in Soler (2013)

Table 3-4. List of minerals included in each of the simulation cases, as included in the ThermoChimie version 9b thermodynamic database (Giffaut et al. 2014).

Simplified reference case	Crystalline C-S-H phases	No illite	Set from Soler and Mäder (2010)	Full reference case	Soler (2013) secondary zeolites
(a)	(c)	(d)	(e)	(f)	(g)
Calcite	Calcite	Calcite	Calcite	Calcite	Calcite
Gypsum	Gypsum	Gypsum	Gypsum	Gypsum	Gypsum
Portlandite	Portlandite	Portlandite	Portlandite	Portlandite	Portlandite
C-S-H 1.6	Jennite	C-S-H 1.6	Hillebrandite	C-S-H 1.6	C-S-H 1.6
C-S-H 1.2	Tobermorite	C-S-H 1.2	C-S-H 1.6	C-S-H 1.2	C-S-H 1.2
C-S-H 0.8	Gyrolite	C-S-H 0.8	Foshagite	C-S-H 0.8	C-S-H 0.8
Ettringite	Ettringite	Ettringite	C-S-H 1.2	Ettringite	Ettringite
C_3AH_6	C_3AH_6	C_3AH_6	Tobermorite	C_3AH_6	C_3AH_6
Brucite	Brucite	Brucite	C-S-H 0.8	Brucite	Brucite
SiO_2 (am)	SiO_2 (am)	SiO_2 (am)	Gyrolite	SiO_2 (am)	SiO_2 (am)
Illite Al	Illite Al	Analcime	Okenite	Illite Al	Illite Al
Analcime	Analcime	Heulandite Ca	Gismondine	Analcime	Analcime
Heulandite Ca	Heulandite Ca	Heulandite Na	Scolecite	Heulandite Ca	Clinochlore
Heulandite Na	Heulandite Na	Clinochlore	Wairakite	Heulandite Na	Clinopt. Ca
Clinochlore	Clinochlore	Clinopt. Ca	Stilbite	Clinochlore	Clinopt. Na
Clinopt. Ca	Clinopt. Ca	Clinopt. Na	Mordenite Ca	Clinopt. Ca	Clinopt. K
Clinopt. Na	Clinopt. Na	Phillipsite Ca	Ettringite	Clinopt. Na	Mordenite Ca
Phillipsite Ca	Phillipsite Ca	Phillipsite Na	C_3AH_6	Phillipsite Ca	Stilbite
Phillipsite Na	Phillipsite Na	Saponite Ca	Brucite	Phillipsite Na	Natrolite
Saponite Ca	Saponite Ca	Saponite Na	SiO_2 (am)	Saponite Ca	Gismondine
Saponite Na	Saponite Na	Saponite K	Illite Al	Saponite Na	Saponite Ca
Saponite K	Saponite K	Saponite Mg	Analcime	Saponite K	Saponite Na
Saponite Mg	Saponite Mg		Heulandite Ca	Saponite Mg	Saponite K
			Heulandite Na	Syngenite	Saponite Mg
			Clinochlore	C_4AH_{13}	Syngenite
			Clinopt. Ca	Monocarbo.	C_4AH_{13}
			Clinopt. Na	Hydrotalcite	Monocarbo.
			Phillipsite Ca	Hydrotalcite C	Hydrotalcite
			Phillipsite Na	Monosulpho.	Hydrotalcite C
			Saponite Ca	Strätlingite	Monosulpho.
			Saponite Na		Strätlingite
			Saponite K		
			Saponite Mg		

Clinopt., monocarbo. and monosulpho. stand for clinoptilolite, monocarboaluminate and monosulphoaluminate, respectively.

4 Description of conceptual model – reference case

4.1 Geometry and material properties

A cross-sectional representation of the BHA vault is shown schematically in Figure 4-1. The model considered in this work is a 1D description of this system, representing a line across the entire right half of the vault, starting at the mid vertical symmetry plane. The 1D geometry includes the waste domain, the concrete structure containing the waste, and the bentonite backfill. The geometry is limited by the host rock on the right side.

The thickness of the bentonite backfill (2.3 m) and the concrete structure (0.5 m) considered in the model corresponds to the geometry of Figure 4-1. On the other hand, the thickness of the waste domain is set following a criterion of maintaining the waste-to-concrete volume ratio (per meter depth). From the dimensions in Figure 4-1, the volume (per meter depth) of the concrete structure containing the waste is 23.4 m^3, while the volume of the waste is 111 m^3. Thus, the waste-to-concrete volume ratio is 4.74. In the 1D model, this is equivalent to 2.37 m-thick waste domain, i.e. 4.74 times larger than the 0.5 m-thick concrete structure. Conceptual model dimensions are presented in Figure 4-2.

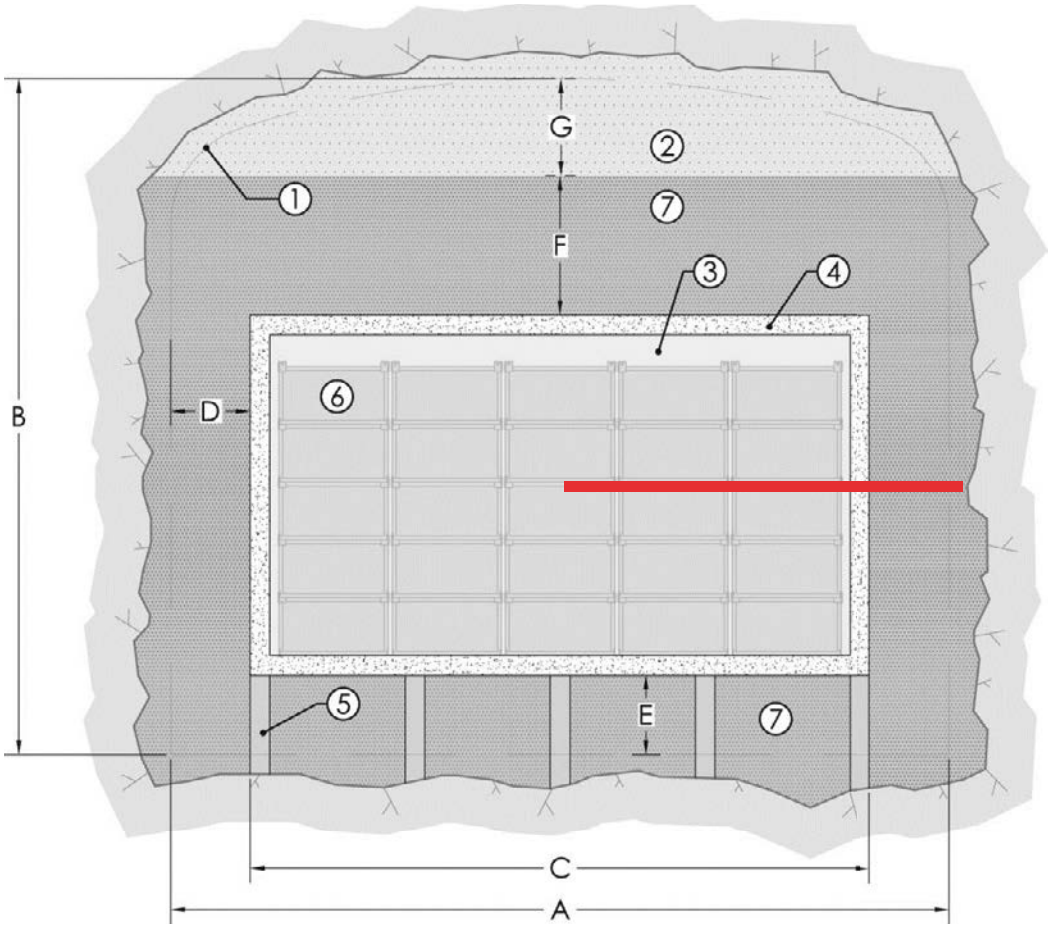

Figure 4-1. *Schematic cross-sectional layout of BHA. Legend: 1) Theoretical tunnel contour. 2) Bentonite pellets. 3) Grout. 4) Concrete structure (0.5 m). 5) Granite pillars. 6) Waste packages. 7) Bentonite blocks. Approximate dimensions: A = 20.6 m, B = 18.5 m, C = 16 m, D = 2.3 m, E = 2.4 m, F = 4 m, G = 3.7 m. Adapted from SKB (2019).*

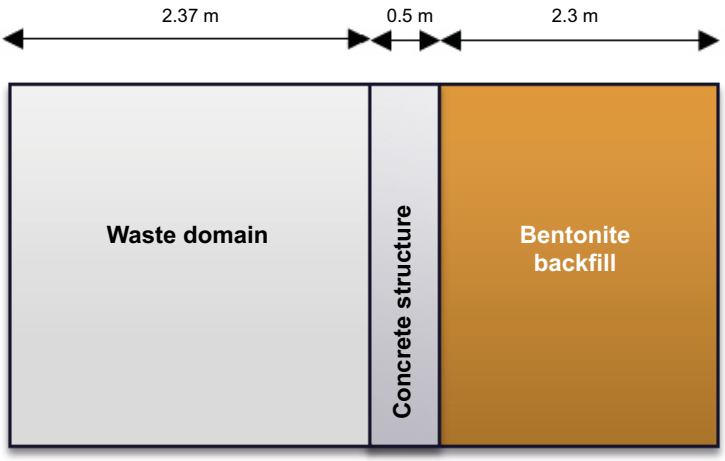

Figure 4-2. *Schematic conceptual model including geometric description and dimensions.*

This 1D geometry setup ensures a correct waste-to-concrete volume ratio in the system and represents a conservative assumption in terms of volume/thickness ratio of the bentonite backfill. The bentonite backfill thickness used corresponds to the lateral walls (the smallest thickness of the bentonite barrier). However, the bentonite layer on top and at the bottom of the vault are 4 and 2.4 m respectively. Thus, the 1D simplification will over-estimate the mass fraction of montmorillonite dissolved (on the BHA-vault scale) during bentonite backfill degradation.

The physical properties of the 3 materials used in the modelling study are presented in Table 4-1. These data are taken from SKB (2011) and Ochs and Talerico (2004) for bentonite, and Idiart and Shafei (2019) for waste and concrete. It is noted that the feedback between mineral dissolution/precipitation reactions and physical properties (i.e. porosity, diffusivity) is not considered in the model. This simplification is thought to be justified by the fact that changes in porosity and related properties due to mechanical stresses will probably also play an important role. Therefore, considering porosity changes only due to chemical alteration disregarding mechanical effects would not give a complete description of a much more complex problem. Nonetheless, the evolution of porosity that would result from the mineral alteration predicted by the model is monitored and is reported in order to give an idea of the magnitude of porosity changes due to geochemical reactions in the studied system.

Table 4-1. Physical properties of the 3 modelled domains; from SKB (2011) and Ochs and Talerico (2004) for bentonite and Idiart and Shafei (2019) for concrete and waste domains.

Material	Porosity, φ_0	D_e (m^2/s)	D_p (m^2/s)
Bentonite	0.423	1.20×10^{-10}	2.84×10^{-10}
Concrete	0.11	3.50×10^{-12}	3.18×10^{-11}
Waste	0.3	3.50×10^{-10}	1.17×10^{-9}

The chemical setup is based on the use of the thermodynamic database ThermoChimie version 9b (Giffaut et al. 2014). Redox equilibrium is not computed for this system since (1) S^{VI}–S^{-II} redox pair is decoupled in the database, and (2) Fe is not considered in the simulations. All chemical reactions have been calculated assuming thermodynamic equilibrium except for the dissolution of the following primary minerals: montmorillonite, illite, quartz, and feldspar. All simulations consider a fully water saturated and isothermal system, with a constant temperature of 15 ºC, as expected under SFL repository conditions (SKB 2019).

The mineralogical phase assemblage of the concrete structure (Table 4-2) is taken from the description of the backfill of the BHK vault in SFL, corresponding to an OPC with a water-to-cement ratio of 0.47 (Idiart et al. 2019). This composition is calculated as a result of a cement hydration model based on thermodynamic modelling. It is noted that, even though the chemical setup used here is almost equivalent, some differences arise due to the change of temperature (from 25 to 15 ºC), of thermodynamic database (CEMDATA to ThermoChimie v9b), or of modelling strategy of some components.

The change in modelling strategy concerns the C-S-H phases. These gels were modelled as a solid solution in Idiart et al. (2019), while using ThermoChimie C-S-H is represented as three single equilibrium phases with different Ca/Si ratios. In the present model, the initial composition has a C-S-H with a Ca/Si ratio of 1.6, slightly different from the solid solution model used in Idiart et al. (2019). This implies a small reduction in portlandite content to maintain the mass balance of Ca. The change in thermodynamic database mainly impacts one of the primary minerals. In particular, all monosulphoaluminate dissolves to form ettringite, as this last mineral is more stable if the data included in ThermoChimie v9b are considered. The differences in stoichiometry between these two minerals lead to an aluminium remnant that is consumed by hydrogarnet precipitation. The last modification concerns the reduction of temperature from 25 ºC to 15 ºC, which impacts the porewater composition and increases the pH.

The waste domain is assumed here to be composed of the same concrete composition as the hosting concrete structure. The chemical assemblage of the waste domain is equivalent to that of the concrete structure. However, the difference between the waste and concrete domains is that the amount of concrete per unit volume of waste domain is lower than that in the concrete structure. A concrete volume fraction of 0.477 is calculated in the waste domain from Pękala et al. (2015), while obviously, the volume fraction in the concrete domain is 1. The same initial concrete porewater is assumed in both domains.

MX-80 bentonite is basically composed of montmorillonite (84 wt%) and minor amounts of quartz, K-feldspar and mica (SKB 2011). The composition of montmorillonite in the MX-80 bentonite has been determined in dedicated studies (e.g. Neaman et al. 2003, Carlson 2004, Savage et al. 2010) and is characterised by the predominance of Na in the interlayer water. According to Savage et al. (2010), the chemical-structural composition of montmorillonite is:

$$Na_{0.18}Ca_{0.1}(Al_{1.64}Mg_{0.36})(Si_{3.98}Al_{0.02})O_{10}(OH)_2 \quad (4\text{-}1)$$

The thermodynamic data and solubility constant used in this study correspond to those included in ThermoChimie v9b (see Appendix A). The mineralogical phase assemblage of bentonite backfill is presented in Table 4-3. The chemical composition of MX-80 bentonite is based on that reported by SKB (2011), which is in turn based on the experimental characterization by Karnland (2010).

The cation exchange capacity and the initial composition of the cation exchanger of bentonite are also taken from SKB (2011). This cation concentration and the selectivity coefficients (log K) (Bradbury and Baeyens 2002) for bentonite initial setup is presented in Table 4-3. This model is intended to represent an initially sodium-dominated bentonite that interacts with the calcium leached from the cementitious system, ultimately leading to a calcium-dominated bentonite.

To define the set of primary minerals based on the used thermodynamic database, some of the phases identified have been grouped together, such as calcite and siderite (as calcite), or quartz and cristobalite (as quartz). Calcite and gypsum dissolve/precipitate under thermodynamic equilibrium. In turn, montmorillonite, illite, quartz, and feldspar dissolution is kinetically controlled. Table 4-4 shows the references of the kinetic rate laws implemented as well as the reactive surface area considered in the simulations.

The initial bentonite porewater composition is given in Table 4-5 and compared to that of the concrete domains. The porewater composition is taken from the work by Sena et al. (2010), re-equilibrated with the primary minerals and exchangeable cations in Table 4-3 at 15 ºC using the thermodynamic database ThermoChimie version 9b (Giffaut et al. 2014).

Table 4-2. Mineralogical phase assemblages of the concrete and waste domains (adapted from Idiart et al. 2019). The chemical composition of the minerals and their equilibrium constants are given in Appendix A.

Primary minerals	Concentration (mol/L_{medium})	Concentration (M)	Volume fraction (-)	Concentration (mol/L_{medium})	Concentration (M)	Volume fraction (-)
	Concrete domain			**Waste domain**		
Equilibrium phases						
Portlandite	1.372	12.473	0.045	0.654	2.181	0.022
C3AH6	0.165	1.495	0.025	0.078	0.262	0.012
CSH 1.6	1.261	11.464	0.107	0.602	2.005	0.051
Hydrotalcite OH	0.016	0.144	0.004	0.008	0.025	0.002
Monocarboaluminate	0.033	0.302	0.009	0.016	0.053	0.004
Ettringite	0.027	0.244	0.019	0.013	0.043	0.009
Porosity			0.11			0.3
Inert mineral Volume			0.682			0.601
Exchanger composition			**Equiv. conc. (%)**			**Equiv. conc. (%)**
$CaXa_2$	0.0429	0.3902	68.84	0.0205	0.0682	68.84
K_2Xa_2	0.0166	0.1506	26.58	0.0079	0.0263	26.58
Na_2Xa_2	0.0029	0.0260	4.58	0.0014	0.0045	4.58

Table 4-3. Mineralogical phase assemblage of the bentonite backfill (from SKB 2011). The chemical composition of the minerals and their equilibrium constants are given in Appendix A. Selectivity coefficients from Bradbury and Baeyens (2002).

Primary minerals	Weight (%)	Concentration (mol/L_{medium})	Concentration (M)	Volume fraction (-)
Equilibrium phases				
Calcite	1	0.157	0.373	0.006
Gypsum	1	0.092	0.217	0.007
Kinetic reactants				
Montmorillonite	84	3.573	8.468	0.501
Illite	4	0.157	0.371	0.022
Quartz	4	1.050	2.483	0.024
Feldspar*	4	0.227	0.569	0.025
Exchanger composition	**Log K**			**Equiv. conc. (%)**
Na_2X_2	0	0.8871	2.0972	75
CaX_2	0.4	0.0414	0.0979	7
KX	0.6	0.1892	0.4473	16
MgX_2	0.34	0.0118	0.0279	2

* Considered as albite in the simulations, a Na-rich mineral of the feldspar family that is included in ThermoChimie v9b.

Table 4-4. Dissolution rate sources and specific surface area implemented for each kinetically dissolving primary mineral.

Primary mineral	Dissolution rate reference	Specific surface area (m^2/g)
Montmorillonite	Nakabayashi (2014)	800
Illite	Köhler et al. (2013)	0.6867
Quartz	Knauss and Wolery (1988)	0.0067
Feldspar	Sverdrup and Warfvinge (1995)	0.6701

Table 4-5. Porewater compositions of cementitious domains (adapted from Idiart et al. 2019) and bentonite porewater composition (adapted from Sena et al. 2010).

	Bentonite porewater	Concrete porewater	Waste porewater
pH	7.637	13.605	13.605
Temperature (°C)	15	15	15
Ionic strength (M)	0.434	0.260	0.260
Solutes (totals)	**Concentration (M)**		
Al	2.295×10^{-10}	2.084×10^{-04}	2.084×10^{-04}
C	2.865×10^{-03}	6.808×10^{-07}	6.808×10^{-07}
Ca	1.038×10^{-02}	1.606×10^{-03}	1.606×10^{-03}
Cl	1.375×10^{-01}	1.000×10^{-10}	1.000×10^{-10}
K	1.696×10^{-02}	2.257×10^{-01}	2.257×10^{-01}
Mg	3.582×10^{-03}	3.684×10^{-10}	3.684×10^{-10}
Na	3.770×10^{-01}	4.005×10^{-02}	4.005×10^{-02}
S	1.408×10^{-01}	1.560×10^{-04}	1.560×10^{-04}
Si	1.334×10^{-04}	2.906×10^{-05}	2.906×10^{-05}

Understanding the role of secondary minerals that may form as a result of cement-bentonite interaction is very important to determine the geochemical conditions under which montmorillonite dissolves. This is because the aqueous composition of the bentonite porewater affected by the alkaline plume is to a large extent governed by the set of minerals that form in the altered region. In the concrete domain, dissolution of primary minerals is expected to lead to the precipitation of calcite, Mg-bearing phases, saponites and zeolites (Gaucher et al. 2005, Marty et al. 2014).

For the bentonite domain, Savage et al. (2007) presented a detailed discussion about the role of secondary minerals. Figure 4-3 shows the groups of minerals that are expected to form when a hyperalkaline source reaches the bentonite and their sequence in space and time (Savage et al. 2007). This sequence of mineralogical groups has been translated to the specific mineral phases conforming the secondary minerals. Given the importance of the secondary minerals included in the simulations, several sensitivity cases accounting for different secondary minerals have been performed.

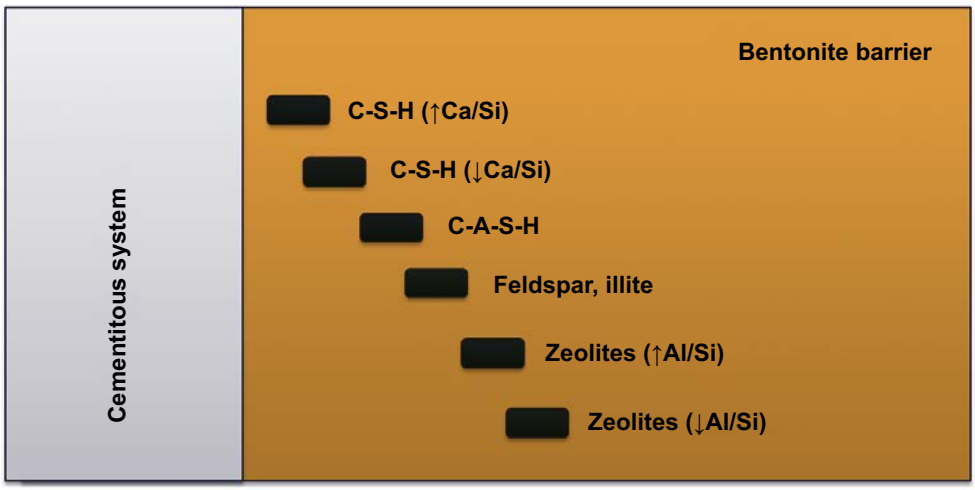

Figure 4-3. *Conceptual scheme of the groups of minerals expected to form in the bentonite barrier following interaction with cementitious alkaline waters. pH values decrease from the cement source (left) towards the bentonite barrier (right). Adapted from Savage et al. (2007). C-S-H: calcium silicate hydrates. C-A-S-H: calcium aluminium silicate hydrates. ↑ Ca/Si: high Ca/Si ratio. ↓ Ca/Si: low Ca/Si ratio. ↑ Al/Si: high Al/Si ratio. ↓ Al/Si: low Al/Si ratio.*

Table 4-6 presents a list of the secondary minerals that are allowed to precipitate if supersaturation of the solution is reached in the reference case. All secondary minerals are considered to form or redissolve under thermodynamic equilibrium. The list in Table 4-6 is inspired by the conceptual model presented in Savage et al. (2007) and is also based on a review of existing experimental data. In general, these secondary minerals form when their solubility products are attained due to the release of ions from primary mineral dissolution (essentially montmorillonite, but also quartz) and the inflow of the alkaline plume. However, some of these minerals share similar chemical compositions and compete for ions (i.e. zeolites, clay minerals), and kinetic and structural ordering effects control the potential precipitation of secondary minerals. In addition, the chemical composition of both cementitious and bentonite porewaters has a certain influence on the nature and amount of the precipitates.

Compared with other modelling studies, poorly crystalline or amorphous phases have been primarily selected in this work since these are kinetically favoured. For example, amorphous C-S-H gels are selected instead of their crystalline equivalents (jennite, tobermorite, gyrolite), and $SiO_{2(am)}$ instead of chalcedony or quartz. On the other hand, zeolites are commonly found as alteration products of ultramafic igneous rocks in equilibrium with moderately alkaline solutions with pH values of approximately 9 to 10. The high calcium-sodium ratio of cementitious porewater once alkalis are leached favours the formation of minerals such as analcime and heulandite. Depending on the pH evolution, other similar zeolite phases (e.g., clinoptilolite, phillipsite) and clay minerals (saponite, secondary Al-rich illite) could also form. Zeolites and clays could replace each other if saturated conditions evolve with time. Additional phases such as brucite and clinochlore (Mg end-member of chlorite group) have been added to prevent an unrealistic excess of magnesium in solution due to the continuous dissolution of montmorillonite. Finally, secondary cement-based minerals have also been included (Table 4-6).

Table 4-6. Secondary minerals allowed to precipitate in the reference case. The chemical composition of the minerals and their equilibrium constants are presented in Appendix A.

Secondary minerals		
Concrete minerals	*Zeolites*	*Clayey minerals*
Portlandite	Analcime	Saponite-Na
CSH 1.6	Heulandite-Ca	Saponite-K
CSH 1.2	Heulandite-Na	Saponite-Mg
CSH 0.8	Phillipsite-Ca	Illite-Al
C_3AH_6	Phillipsite-Na	Saponite-Ca
C_4AH_{13}	Clinoptilolite-Ca	
Brucite	Clinoptilolite-Na	
Ettringite	*Others*	
Hydrotalcite	Calcite	
Hydrotalcite-CO3	SiO_2(am)	
Monocarboaluminate	Gypsum	
Monosulphoaluminate	Syngenite	
Strätlingite	Clinochlore	

One of the important chemical reactions in the bentonite – cement system is the dissolution of montmorillonite. The dissolution kinetic rate law used in this study is based on the work by Sato et al. (2004) and Oda et al. (2014). The 'Sato rate law' describes the dependence of the dissolution rate on pH (i.e. OH^-) and temperature (T) with two different terms or reaction paths:

$$R_{Sato} = 4.74 \cdot 10^{-6} e^{-39.54/RT} \frac{177 e^{20.36/RT} a_{OH-}}{1 + 177 e^{20.36/RT} a_{OH-}} + 1.70 e^{-69.66/RT} \frac{0.0297 e^{23.51/RT} a_{OH-}}{1 + 0.0297 e^{23.51/RT} a_{OH-}} \qquad (4\text{-}2)$$

where R_{Sato} is the dissolution rate ($mol \cdot m^{-2} \cdot s^{-1}$), R is the universal gas constant (8.31×10^{-3} $kJ \cdot mol^{-1} \cdot K^{-1}$), T is temperature (288.15 K in the present study), and a_{OH-} (M) is the activity of OH^-. The rate expression given in Equation (4-2) is plotted as a function of pH in Figure 4-4 for a constant temperature of 15 °C. Note that this rate expression shows an increase in the rate with increasing pH values and that this increase is larger the higher the temperature. At 15 °C, the increase of the rate for an increase in pH from 8 to 13 is less than one order of magnitude.

The resulting rate is significantly faster than other rates proposed in the literature (e.g. Rozalén et al. 2008, 2009) as shown in Figure 4-5. Later, Oda et al. (2014) included in the Sato et al. (2004) rate law the dependence of the rate on the proximity to thermodynamic equilibrium of the dissolution reaction. The 'Oda term' is given by:

$$R_{Oda} = \left[1 - e^{p\left(\frac{\Delta Gr}{\sigma RT}\right)^q}\right] \quad (4\text{-}3)$$

where R_{Oda} (-) is the rate term and p, q and σ are fitting parameters. The original fitting parameters were modified by Nakabayashi (2014), being $\sigma = 2$, $p = 2.56 \times 10^{-5}$ and $q = 3$. In this way, the resulting kinetic rate law is quite similar to other rates (Figure 4-5):

$$R_{Sato-Oda} = R_{Sato} \cdot R_{Oda} \quad (4\text{-}4)$$

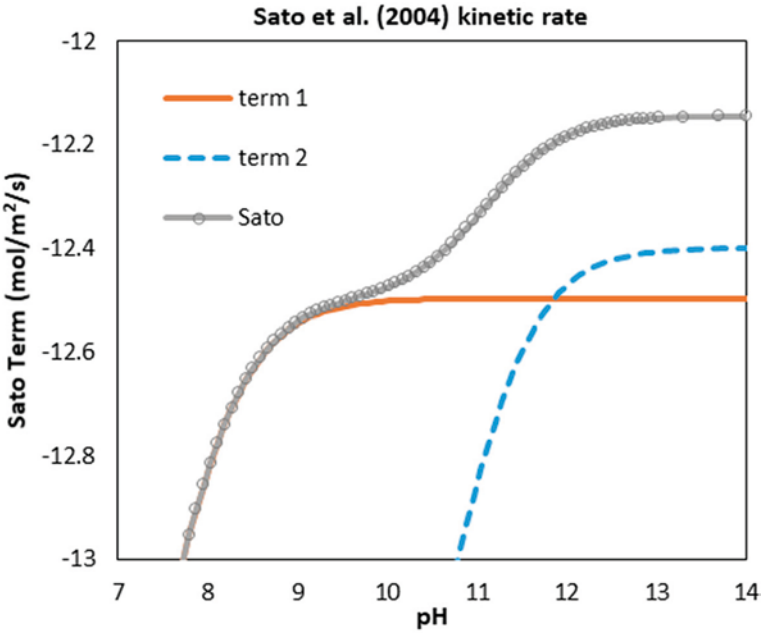

Figure 4-4. *Evolution of the Sato term with pH based on Sato et al. (2004) rate law for montmorillonite dissolution for a temperature of 15 ºC. The relative impact of the two terms of Equation (4-2) is shown. At highly alkaline pH the second term governs the dissolution.*

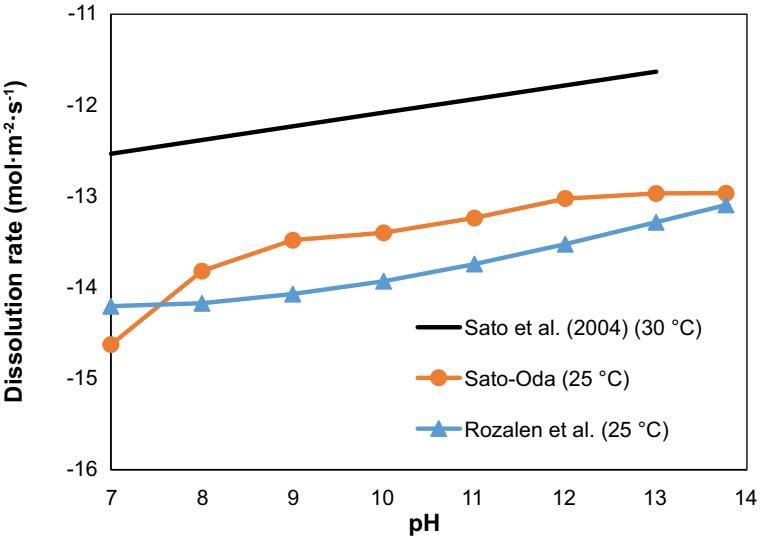

Figure 4-5. *Dissolution rates as a function of pH using Sato et al. (2004), Sato-Oda (with modifications by Nakabayashi 2014) and Rozalén et al. (2008) rate laws, considering a ΔGr= −65 J·K⁻¹·mol⁻¹.*

In the present study, there are 3.573 moles of montmorillonite per litre of bentonite (Table 4-3). The time needed to dissolve all montmorillonite of 1 litre of bentonite can be calculated using Equations (4-2) to (4-4) provided that the pH and the saturation index of the pore solution with respect to montmorillonite are fixed at the dissolution front. In that case, the time to dissolve montmorillonite is given by $t_{mmt} = m_0/R$, where m_0 is the initial amount of bentonite (3.573 moles/litre bentonite) and R is the dissolution rate (mol/year). The results of these calculations are summarized in Figure 4-6 for different pH and saturation index values at 15 ºC. A surface area of 800 $m^2 \cdot g^{-1}$ is *a priori* assumed as an unfavourable scenario, but two sensitivity cases with lower values will be presented. This figure illustrates two important aspects of the Sato-Oda rate law:

1) The dependence of the rate on the value of pH is important. The time needed to dissolve all montmorillonite from one litre of bentonite is reduced by 27.6 times when increasing the pH from 7.0 to 13.0, independent of the value of the saturation index. However, that time is only 4.2 times faster when increasing the pH from 8.0 to 12.0.
2) The impact of an increase in the undersaturation of the pore solution with respect to montmorillonite on the time needed for complete dissolution is quite significant. For instance, if the saturation index drops from a value of −0.5 to −1.8 or −3.0 the time is reduced by a factor of 46.7 or 216, respectively.

The calculations presented in Figure 4-6 consider a fixed value of the saturation index of the pore solution, which can only be maintained if (1) a given set of secondary minerals precipitate continuously in time and (2) if solutes from the dissolution of accessory minerals or from an external supply are also continuously available.

Available experimental data of montmorillonite dissolution when exposed to different NaOH solutions at different temperatures have confirmed that the pH dependence of the dissolution rate is weaker the lower the temperature (Figure 4-7). At 15 ºC, there increase of the rate for an increase of the pH from 8 to more than 13 is very small (by a factor of 2).

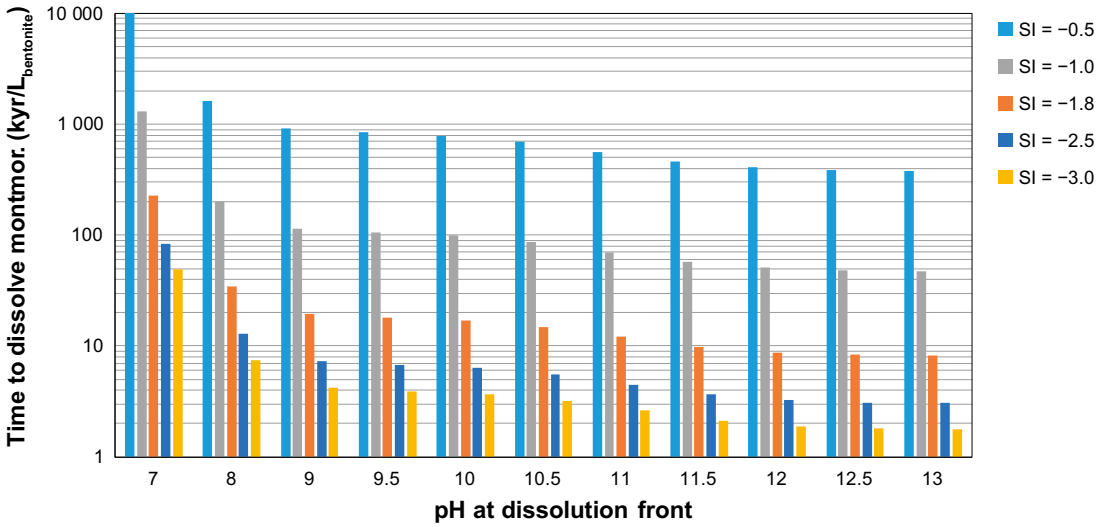

Figure 4-6. *Time needed to dissolve all montmorillonite from one litre of bentonite according to the Sato-Oda rate law (in thousands of years) as a function of pH and the proximity of the pore solution to thermodynamic equilibrium with montmorillonite (SI = saturation index). A fixed temperature of 15 ºC is considered in all calculations.*

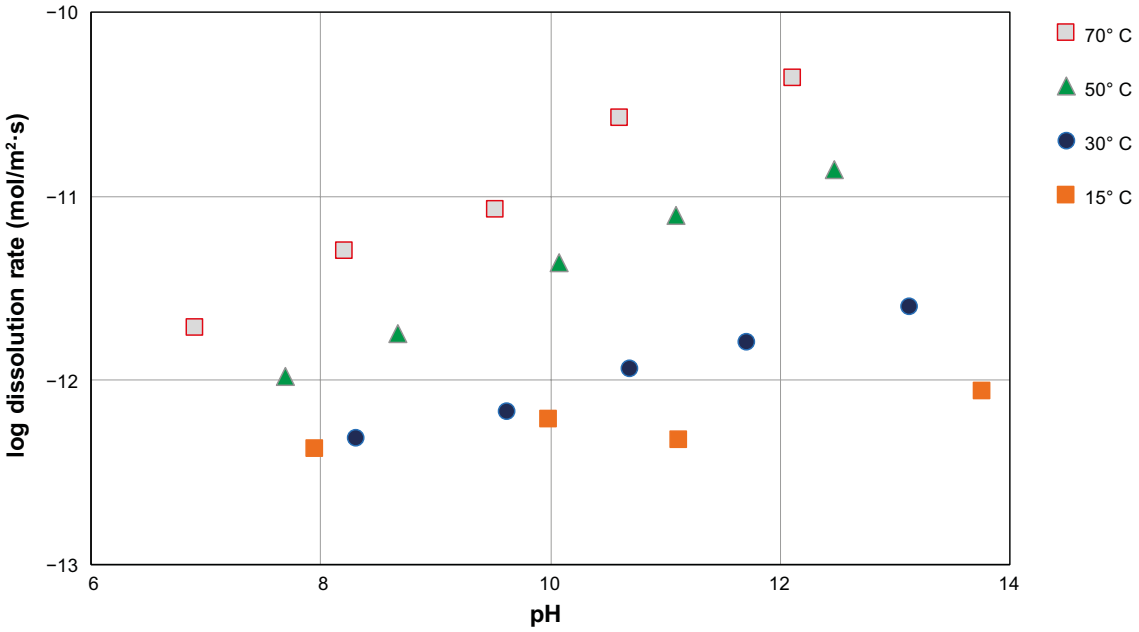

Figure 4-7. *Relation between the dissolution rates of montmorillonite (in log scale, mol·m^{-2}·s^{-1}) and the pH of NaOH solutions at different temperatures (15, 30, 50, and 70 ºC). Experimental results from Sato et al. (2004) and Sato and Oda (2015).*

4.2 Review of montmorillonite reactive surface area

The dissolution rates are multiplied by a reactive surface area to calculate the mass of dissolved montmorillonite. In this study, a reactive surface area of 800 m^2·g^{-1} is considered in the idealized and reference cases, which is in the range of the total surface area, i.e. including the interlayer surfaces (Karnland 2010, Bradbury and Baeyens 2011). The total surface area can be measured by e.g. the EGME (ethylene glycol monoethyl ether) method (Kiviranta and Kumpulainen 2011). The reactive surface area is considered constant throughout the simulation, i.e. no changes with porosity or mass fraction is considered in any of the dissolution rates. To analyse the impact of this parameter on the results a sensitivity case is proposed using a lower value of reactive surface area of 30 m^2·g^{-1}, closer to BET measurements of Na-dominated bentonites (Karnland et al. 2006, Kaufhold et al. 2010, Bradbury and Baeyens 2011). However, recent research works suggest that this value might be several orders of magnitude smaller.

The reactive surface area of montmorillonite has been given special attention in recent years. The total surface area (~800 m^2/g in some bentonites) can be subdivided in the basal surface area and the edge surface area (ESA). Experimental measurement of the surface area by N_2 gas adsorption with the Brunauer-Emmett-Teller technique (N_2-BET) only characterizes the external surfaces (Kaufhold et al. 2010), i.e. the sum of external basal surfaces and edge surfaces, with no access to the inter-layer space (Bergaya 1995). It is also noted that these measurements are made on dry samples, which is not representative of the microstructure of water saturated compacted bentonite (Tournassat et al. 2015). Several studies suggest that the reactive surface area for montmorillonite dissolution is limited to the edge surfaces. Bosbach et al. (2000) and Bickmore et al. (2001) studied dissolution of clay minerals (hectorite and nontronite, respectively) under acidic conditions and experimentally showed that dissolution proceeds exclusively at the edge surfaces, the basal surface being unreactive. This was experimentally confirmed in montmorillonite subject to alkaline conditions by Yokoyama et al. (2005) and Kuwahara (2006). Yokoyama et al. (2005) suggested that, based on long-term atomic force microscopy (AFM) observations, dissolution occurs at edge surfaces, so that the ESA should be used to calculate the dissolution rate for montmorillonite under alkaline conditions. They also determined that the dissolution rates of individual particles with different morphologies, as estimated by AFM, are similar to the rates that can be estimated from bulk dissolution experiments. Kuwahara (2006) showed that dissolution rates normalized to the ESA are independent of the particle size, whereas the dissolution rates normalized to the total surface area depend on the particle size.

Marty et al. (2015) proposed a reactive surface area for montmorillonite that is independent of the compaction state (i.e. dry density), but based on the ESA, which is claimed to better represent the reactive surface area than that measured by BET. Based on the works of Yokoyama et al. (2005) and Tournassat et al. (2003), Marty et al. (2015) proposed a reactive surface area of 8.5 $m^2 g^{-1}$, while they previously measured by AFM an ESA of 6.2 $m^2 g^{-1}$ for montmorillonite purified from MX-80 bentonite in a non-compacted system (Marty et al. 2011).

These studies suggest that more knowledge about how the available edge surface area for montmorillonite dissolution (reactive surface area) changes upon variations in dry density is needed. Satoh et al. (2013) recently compared the rate previously determined by Sato et al. (2004) for a montmorillonite suspension and their own measurements for compacted systems. Their results show a decrease of 1 to 2 orders of magnitude of the reactive surface area depending on the dry density under similar chemical and thermodynamic conditions.

Terada et al. (2019) recently published their work on the estimation of the reactive surface area in bentonite at different densities. They performed a series of numerical models based on Monte Carlo analysis, together with a series of montmorillonite dissolution experiments at various densities. They furthermore derived an analytical expression with the corresponding suggested parameterization. Their research clearly shows a decrease in reactive surface area with increasing dry density of bentonite. They ascribe the decrease in reactive surface area to the so-called physical masking effect (Tournassat et al. 2015), which consists in the reduction of the number of available edge surfaces due to contact with planar surfaces of neighboring particles. According to Terada et al. (2019) it is generally observed that montmorillonite dissolution occurs at edge surfaces.

Their Monte Carlo analysis is based on a simple geometrical description of montmorillonite particles by assuming infinitely thin disc shaped particles with constant diameter (450 nm) and assigning a constant thickness (1 nm) *a posteriori*. Two different inter-particle potentials have been used: (1) based on the quadrupole potential that includes surface charge and electric double layer, used for low-density conditions and (2) a rigid-body potential to study high-density conditions. Their analysis shows a good agreement in the intermediate density range. In any case, the dry densities of interest under repository conditions (> 1 000 kg/m^3) are much larger than the intermediate density range studied in Terada et al. (2019). In fact, the most important discrepancy between models is found under highly dilute conditions, where the quadrupole model yields "house of cards" particle aggregates, whereas the rigid-body potential leads to an isotropic distribution.

The masking model is also based on purely geometrical considerations. It introduces a masking parameter indicating the threshold distance between the edge of a particle and the planar surface of a neighboring particle below which the edge surface is masked and does not contribute to the reactive surface area. This masking parameter is largely unknown and is studied by means of a sensitivity analysis (ranging between 4.5 and 36 nm).

Montmorillonite dissolution has been studied experimentally in clays with a dry density ranging from 5 to 205 kg/m^3. Changes in reactive surface area obtained from the Monte Carlo analysis were studied for dry densities between 5 and 1 200 kg/m^3. At very low dry densities, the edge surfaces are virtually not masked. The effective ESA at a dilution limit as well as the maximum reactive surface area has been estimated from geometric considerations (disc-shaped particles of 450 nm in diameter) and assuming a particle density of 2 400 kg/m^3. This results in a maximum ESA of 3.7 m^2/g, which is somewhat lower than the values reported e.g. by Tournassat et al. (2003, 2016), ranging between 5.3 and 25 m^2/g depending on the bentonite and the preparation conditions.

Experimental procedures are missing, so it is not possible to evaluate if the changes in volume measured by AFM occur under constant chemical conditions, which is needed to derive the reactive surface area at different densities from the experimental data. In any case, the comparison between modelled and experimental results in terms of effective ESA is valid only if dissolution of montmorillonite occurs exclusively at edge surfaces and under constant chemical conditions.

They furthermore proposed a simple analytical expression to calculate the montmorillonite reactive surface area (RSA) that is valid in a large range of montmorillonite dry densities:

$$RSA = \frac{RSA_0}{\left(\frac{\rho_b}{\rho_b^*}\right)^{\frac{1}{3}} + \left(\frac{\rho_b}{\rho_b^*}\right)} \tag{4-5}$$

In this equation, ρ_b is montmorillonite dry density, ρ_b^* is the dry density at which phase transition occurs (16.8 kg/m^3) and RSA_0 is the effective RSA for a dilution limit (3.7 m^2/g). A value of 0.03 m$^2\cdot$g^{-1} is obtained for a dry density of 1 586 kg/m^3.

One limitation of the work by Terada et al. (2019) is the perhaps simplistic representation of montmorillonite particles as infinitely thin circular discs with a constant diameter and with a constant thickness of 1 nm assigned *a posteriori*. Possible effects of heterogeneous particles structures are not discussed. Another limitation is that it only focuses on montmorillonite and the effect of dry density. However, in compacted bentonite there is a non-negligible fraction of accessory minerals (silicates, carbonates, gypsum, feldspar, etc). The impact of the presence of these minerals in the microstructure on the reactive surface area of montmorillonite is not discussed in this work and remains uncertain. These limitations may lead to an underestimation of the reactive surface area if applied to compacted bentonite.

In Section 6, the simplified reference case is computed with a reduced reactive surface area of 0.03 m$^2\cdot$g^{-1} (case 5), whereas in Section 7 the equivalent case using the whole domain is presented (case 15).

5 Numerical model setup

The conceptual model described in Section 4 is implemented as a one-dimensional (1D) reactive transport model using iCP (Nardi et al. 2014). This section presents the details of the numerical implementation.

The geometry is composed of 2.37 m of waste domain, 0.5 m of concrete structure and 2.3 m of bentonite backfill (Section 4). The finite element size in each of these domains is 0.12, 0.05 and 0.05 m, respectively, resulting in a total of 76 elements for the entire model (Figure 5-1.).

The analysed period in all the simulations is 100 000 years. Temporal discretization considers constant communication time steps of 0.5 years between the solute transport step (in Comsol) and the chemical reactions step (in PhreeqC). This time step is in turn automatically subdivided into smaller time steps by the transport solver in Comsol and the kinetic solver in PhreeqC (see Nardi et al. 2014 for more details). The time step size for the present setup is a compromise between the computational cost of reducing the finite element size in each simulation and the Von Neumann criterion establishing maximum time step size, Δt (s) as function of the finite element size, Δx (m), and the diffusion coefficient, D (m^2/s):

$$\Delta t \leq \frac{\Delta x^2}{3D} \tag{5-1}$$

Closed (i.e. zero concentration-gradient) boundary conditions are imposed in each of the two boundaries of the model. The left boundary represents the symmetry plane of the vault, while the right side, i.e. the bentonite-rock interface is also considered a closed boundary (the effect of a constant groundwater composition boundary condition is shown not to be significant, see case 7).

The 'Sato-Oda' rate law has been implemented in the geochemical simulator PhreeqC v3 (Parkhurst and Appelo 2013).

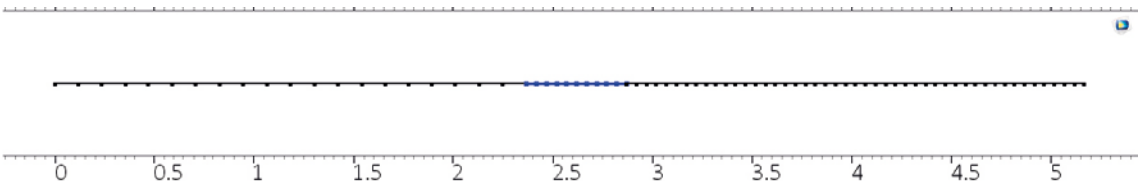

Figure 5-1. *Finite element mesh used in the iCP simulations. Dimension expressed in meters.*

6 Simplified analysis (only bentonite backfill)

As a simplified analysis, a first model accounting exclusively for the bentonite backfill has been used (cases 1–12 in Table 3-1). The influence of the cementitious domains is represented by the left boundary condition of the model, considering a fixed concrete porewater composition in equilibrium with portlandite, as presented in Table 6-1. The physical and mineralogical properties of bentonite are the same as used in the full analysis, although the exchanger is not specifically modelled here (see below). This leads to some differences in the initial bentonite porewater composition (presented in Table 6-1 together with the groundwater composition) compared to Table 4-5. Secondary minerals allowed to precipitate are also slightly different as shown in Section 3. The bentonite domain thickness, 2 m, is also slightly different, as extracted from Elfwing et al. (2013), instead of the 2.3 m for the full model (SKB 2011).

A pH of 12.83 results from equilibrating the pore solution with portlandite at 15 ºC. However, it is noted that the impact of this increase in pH on the dissolution rate is smaller than the impact of decreasing the temperature from 25 to 15 ºC (Sato et al. 2004). For example, the pH in equilibrium with portlandite at 15 and 25 ºC is 12.835 and 12.484, respectively. The kinetic rates from Sato et al. (2004) are 0.7×10^{-12} and 1.5×10^{-12} mol·m^{-2}·s^{-1}, respectively.

The assumed composition of the exchangeable cations in the interlayer of montmorillonite is not sodium-dominated, but calcium-dominated. The reason behind this assumption is that cation exchange reactions are expected to be much faster than montmorillonite dissolution in this system with fixed concrete porewater composition (e.g. Fernández et al. 2009). Therefore, the time scales of these two processes are considered to be uncoupled. In this context, calcium leaching from the cementitious system will rapidly affect the composition of exchangeable cations to a calcium-dominated system before significant dissolution of montmorillonite occurs.

Table 6-1. Concrete porewater composition in equilibrium with portlandite (adapted from Idiart and Shafei 2019). Bentonite porewater composition (adapted from Sena et al. 2010) and groundwater composition corresponding to the old meteoric end member from Pękala et al. (2015).

	Concrete porewater	Bentonite porewater	Groundwater
pH	12.835	7.19	8.64
Temperature (°C)	15	15	15
Ionic strength (M)	0.066	0.227	0.007
Solutes (totals)	**Concentration (M)**		
Al	5.54×10^{-07}	4.11×10^{-10}	1.21×10^{-06}
C	1.00×10^{-05}	2.70×10^{-03}	6.91×10^{-04}
Ca	2.43×10^{-02}	1.85×10^{-02}	5.26×10^{-04}
Cl	5.55×10^{-05}	1.38×10^{-01}	4.54×10^{-03}
K	7.60×10^{-05}	1.14×10^{-03}	7.60×10^{-05}
Mg	2.53×10^{-08}	8.86×10^{-03}	1.48×10^{-04}
Na	4.79×10^{-03}	1.57×10^{-01}	4.79×10^{-03}
S(6)	3.29×10^{-03}	3.60×10^{-02}	3.73×10^{-04}
Si	4.52×10^{-05}	1.34×10^{-04}	1.42×10^{-04}

The results of the set of 1D reactive transport simulations of bentonite degradation (Table 3-1) are presented as spatial distribution profiles at given times and time evolution of integrated values for the entire bentonite domain.

For a better interpretation of the obtained results, global or equivalent values are also presented to quantify the amount of montmorillonite remaining in the entire backfill thickness. The equivalent amount of montmorillonite resulting from the 1D reactive transport simulation is calculated at each time using the following equation:

$$M_{mass} = A \cdot \int_0^L \frac{[C_m]_i + [C_m]_{i-1}}{2} \cdot \varphi_0 \, dx \qquad (6\text{-}1)$$

where L is the backfill thickness, A (1 m^2) is the cross-section, and $[C_m]_i$ and $[C_m]_{i-1}$ are the concentration of montmorillonite (in moles per litre of water) at $x = x_1$ and $x = x_1 + \Delta x$, respectively.

A summary of the results and comparison between different simulation cases (idealized case, the simplified reference case, and the sensitivity cases) presented in Section 3 are shown in Figure 6-16 and Figure 6-17. Furthermore, Appendix B contains a validation of the model through a qualitative comparison of the results presented by Cronstrand (2016) with those obtained with iCP considering a similar setup.

6.1 Results of idealized case (#1)

The first case presented in Table 3-1 considers a setup with no accessory or secondary minerals (case 1). Thus, only kinetically controlled montmorillonite dissolution is considered in this idealized case. Given that it is well-known that the role of accessory and secondary minerals is quite important to determine the spatial extent of concrete–bentonite interactions, this case may be regarded as an academic exercise which aim is to gain system understanding.

In this case, the montmorillonite dissolution front reaches a depth of 0.3 m from the left boundary after 100 000 years, while no effect of the alkaline plume is observed between 0.8 and 2.0 m (Figure 6-1). Even though the pH in the backfill at later times is practically equal to the value imposed as boundary condition (12.8), as shown in Figure 6-2, the saturation index is very low in most of the backfill (lower than −0.1 for more than half of the backfill), and thus the dissolution proceeds very slowly (Equations 4-2 to 4-4). The reason why the saturation index is close to zero is due to the absence of other minerals. Preventing the formation of secondary minerals leads to a situation in which the pore solution is rapidly equilibrated with montmorillonite, with very little dissolution needed to reach this equilibrium. This idealized case is not realistic and is also not conservative. Indeed, more montmorillonite dissolution is expected in the case that the saturation index is maintained far from equilibrium as a result of precipitation of secondary minerals. This is studied in detail in the following simulation cases.

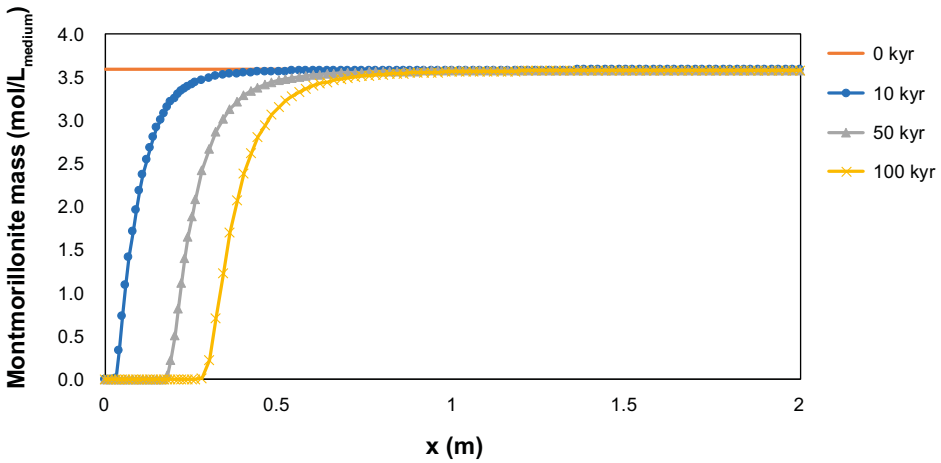

Figure 6-1. *Profiles of montmorillonite mass (mol/litre medium) at different times for the idealized case of only montmorillonite.*

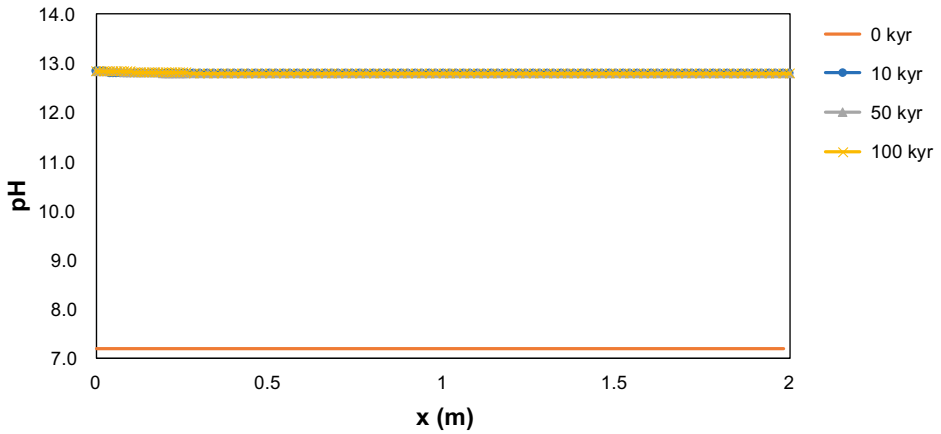

Figure 6-2. *Profiles of pH values of the pore solution at different times for the idealized case of only montmorillonite.*

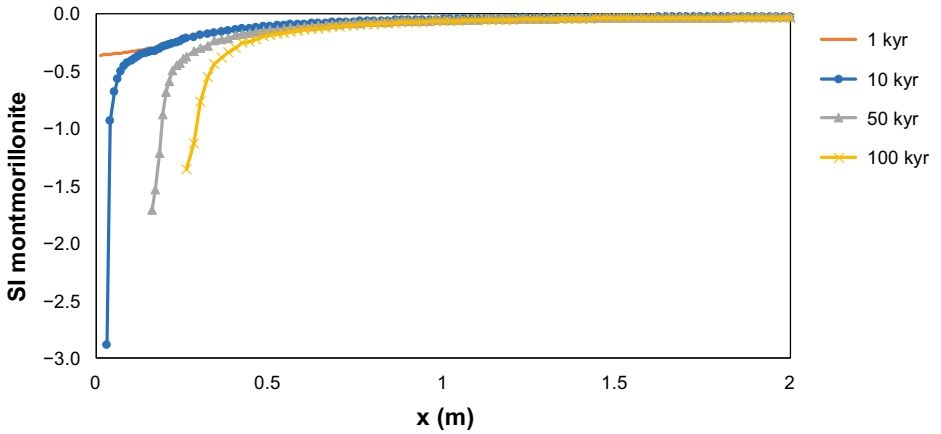

Figure 6-3. *Profiles of saturation index (SI) of montmorillonite in the pore solution at different times for the idealized case of only montmorillonite.*

6.2 Results of simplified reference case (#2)

The results of the simplified reference case (case 2) are presented in Figure 6-4 to Figure 6-11. Overall, the results obtained indicate a significant degradation of the bentonite barrier after 100 000 years of interaction with cementitious water.

Figure 6-4 presents 1D profiles of the evolution of pH of the bentonite pore solution. pH profiles are a good indicator to analyse the extent of dissolution of the bentonite backfill components and its mineralogical variations. After 3 000 years, pH increases up to a value of 9 in the entire backfill porewater, while after 50 000 years, pH is already higher than 10. The pH at the boundary with the cementitious water is fixed to 12.83 (equilibrium with portlandite at 15 ºC). However, pH values higher than 12 are restricted to the vicinity of the left boundary and increase very slowly inside the backfill as locally montmorillonite dissolves completely.

The spatial distribution profiles of dissolution/precipitation of the different mineral phases is shown in Figure 6-5 and Figure 6-6 after 50 000 and 100 000 years, respectively. The spatial sequence of secondary minerals at the end of the simulation is presented schematically in Figure 6-7. Zeolites with different Al/Si ratios form first (mainly calcium heulandite, but also analcime and sodium phillipsite), followed by illite and C-S-H phases. The latter phases have increasing Ca/Si ratio closer to the cementitious source. Ettringite also forms in the presence of sulphate.

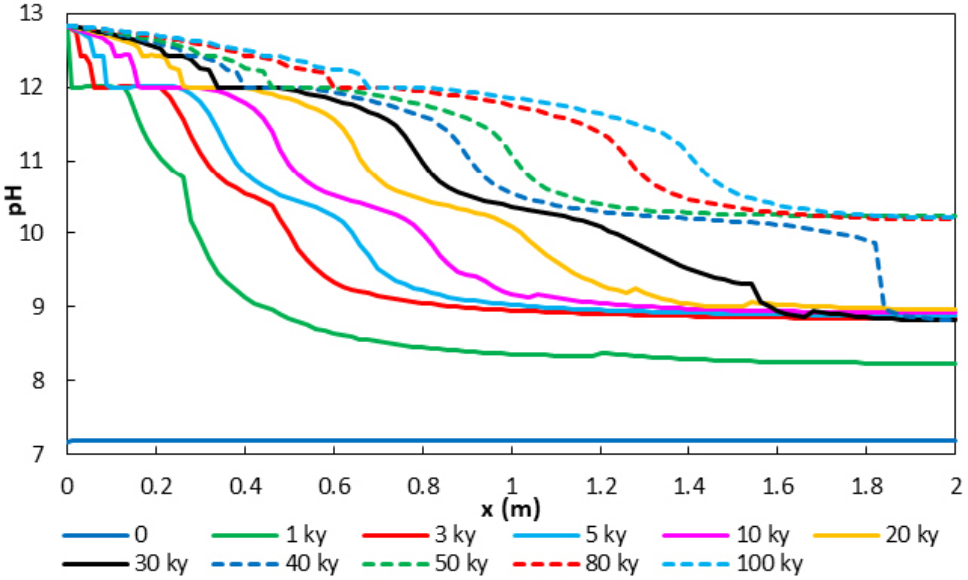

Figure 6-4. *Profiles of pH values of the porewater at different times.*

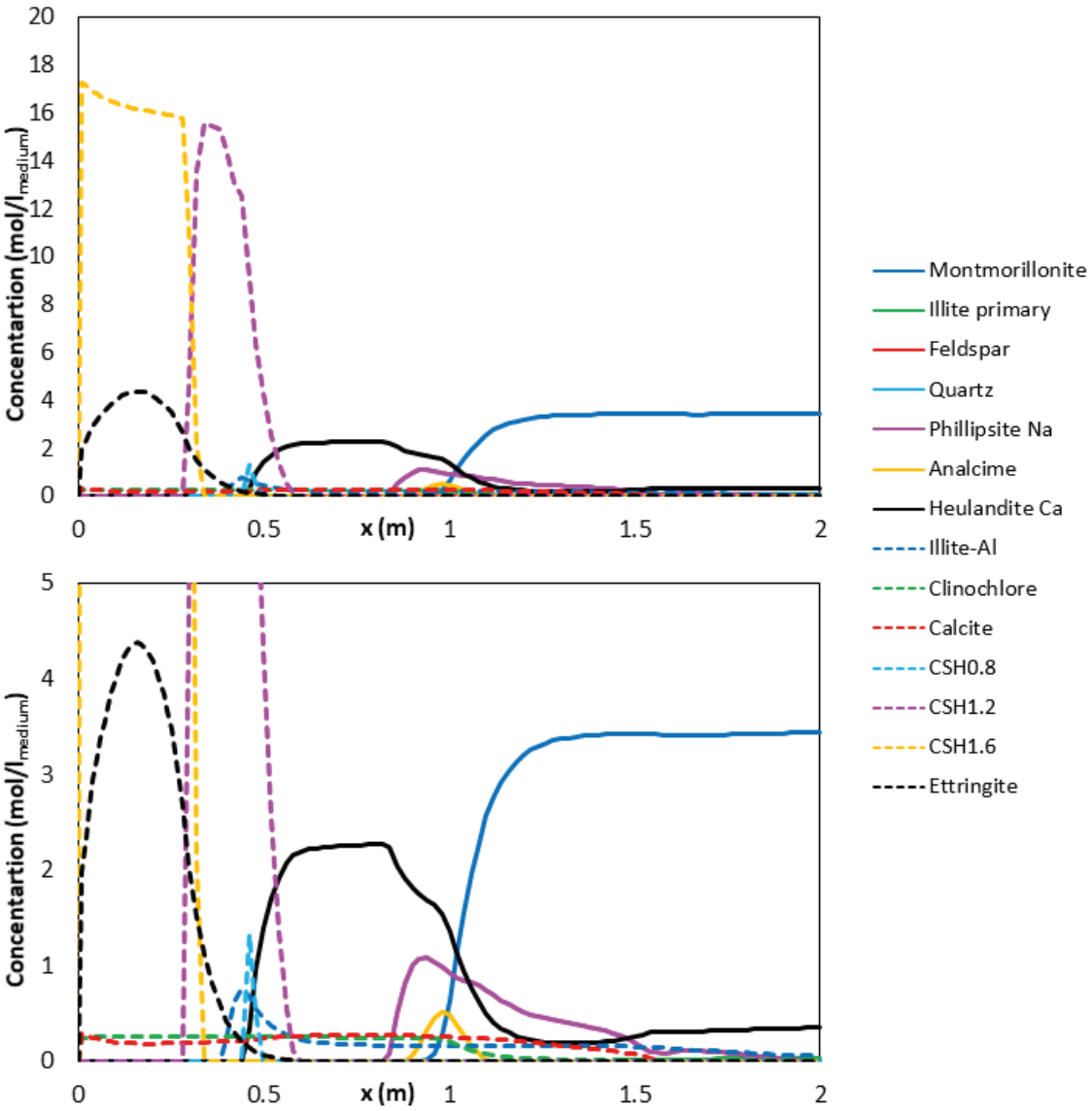

Figure 6-5. *Profile of mineral phase concentration (mol/litre of medium) after 50 000 years. Complete distribution (top) and close-up view of the lower part (bottom).*

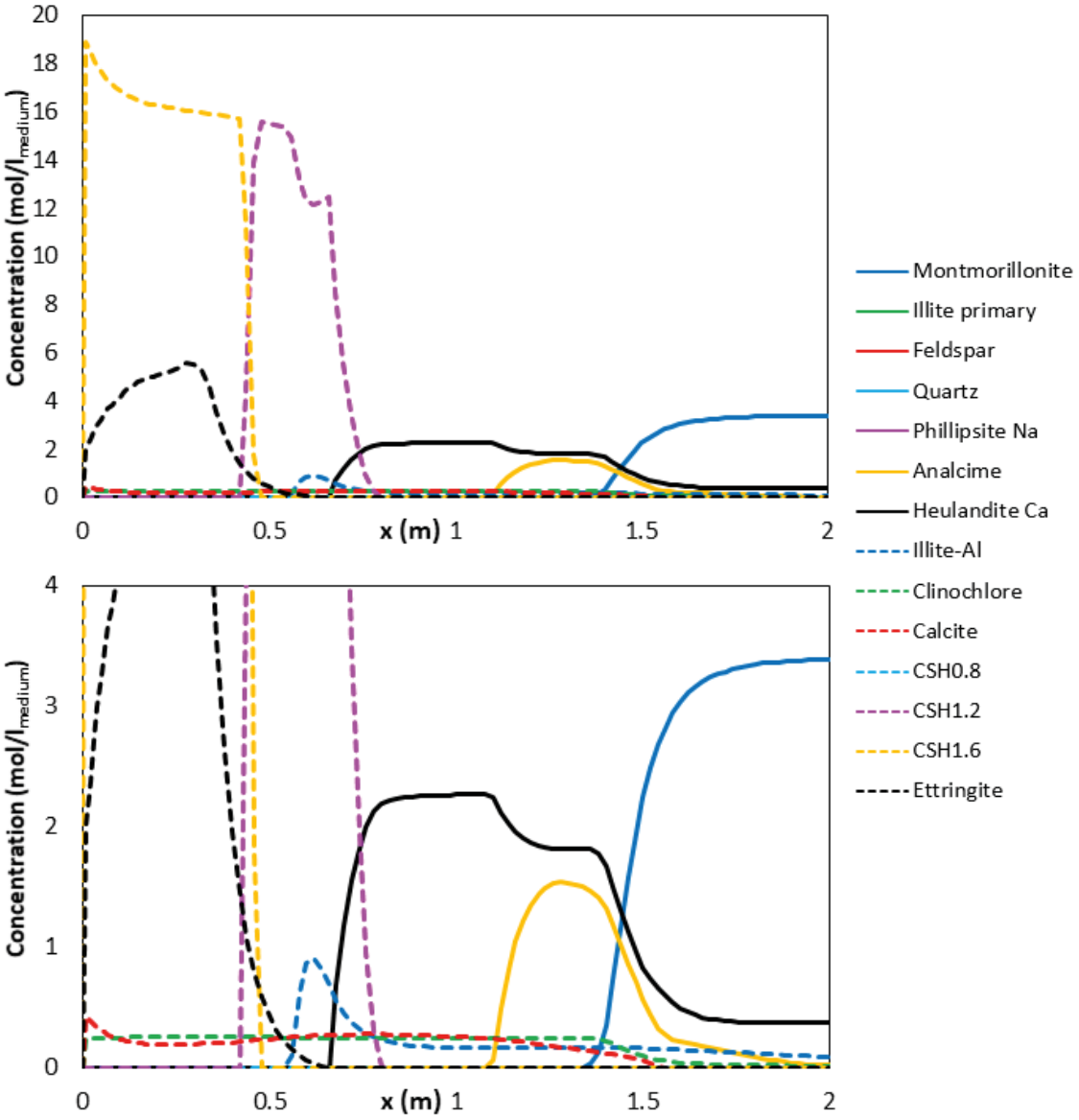

Figure 6-6. *Profile of mineral phase concentration (mol/litre of medium) after 100 000 years. Complete distribution (top) and close-up view of the lower part (bottom).*

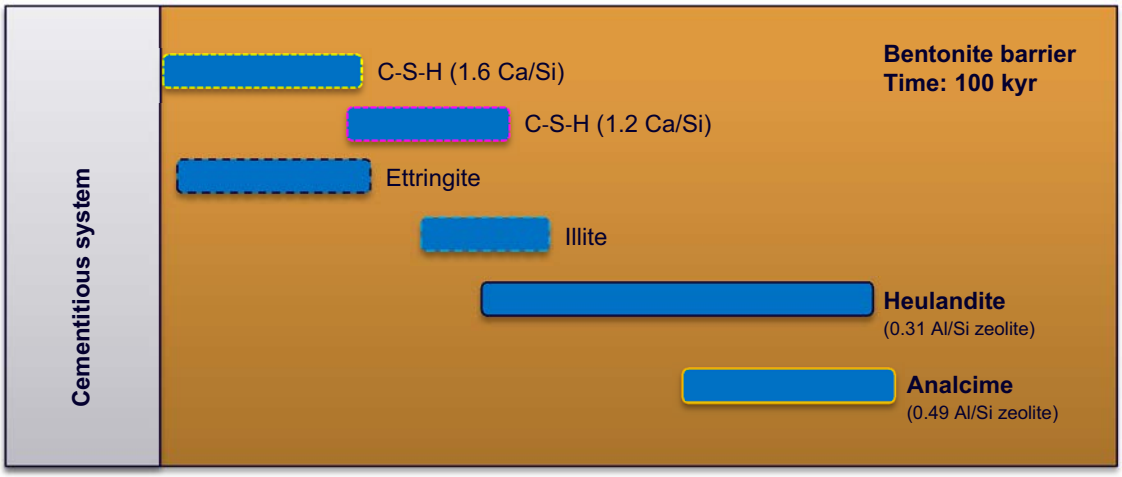

Figure 6-7. *Sequence of secondary minerals formed in the bentonite barrier after 100 000 years, as identified from Figure 6-6.*

All primary minerals except montmorillonite have completely dissolved across the entire thickness of the backfill after 100 000 years. At this time, montmorillonite is only significantly present in the last half meter of the bentonite backfill. On the right boundary (interface with the rock), montmorillonite concentration is around 80 % of its initial value.

Sodium phillipsite (Al/Si = 0.33) is stable during the first ~60 000 years and then dissolves, being replaced by more stable zeolites such as calcium heulandite (Al/Si = 0.31) and analcime (Al/Si = 0.49). A very high concentration of C-S-H phases and ettringite precipitate closer to the cementitious source (i.e. up to 0.8 m from the source). Ettringite has already been identified as a potential secondary mineral in other studies provided that there is a source of sulphate (Watson et al. 2013, Soler 2013, 2016). Clinochlore forms from the release of Mg during montmorillonite dissolution, while a small amount of calcite reprecipitates. The large amount of C-S-H gels and ettringite precipitating in the first centimetres of the backfill is due to the aggressive boundary condition considered in the simulation (fixed concentration, i.e. an infinite source of cementitious leachates). It is noted that porosity is not updated during the simulation (see Section 4).

The concentration of aqueous species after 100 000 years is shown in Figure 6-8. The extremely low concentration of potassium is governed by the solubility of Al-rich illite at alkaline pH values, while magnesium concentrations are controlled by clinochlore. Sodium and chloride concentrations in the entire backfill are close to the boundary condition value (4.79×10^{-3} M and 5.55×10^{-5} M, respectively). Calcium and silica concentrations are mainly controlled by the formation of C-S-H phases with different Ca/Si ratios. Finally, sulphate concentrations are higher near the cementitious source and decrease with the distance from this source, controlled by ettringite formation in the bentonite backfill.

The spatial distribution of the montmorillonite concentration profile at different times is shown in Figure 6-9. After 100 000 years, the dissolution depth has reached an average of 1.5 m. In the same figure, the dissolution of the barrier as a non-linear and time-dependent process is also illustrated. After 20 000 years, half of the final travel distance of the montmorillonite dissolution front has already been reached.

Figure 6-10 shows the temporal evolution of the normalized mass of montmorillonite. The normalized mass is the ratio between the remaining and initial mass of montmorillonite in the backfill. Bentonite degradation is a non-linear process, showing first a very high dissolution rate. In only 6 800 years, the bentonite backfill has been reduced by 25 %, and after 32 000 years a value of 50 % of the primary barrier material is attained.

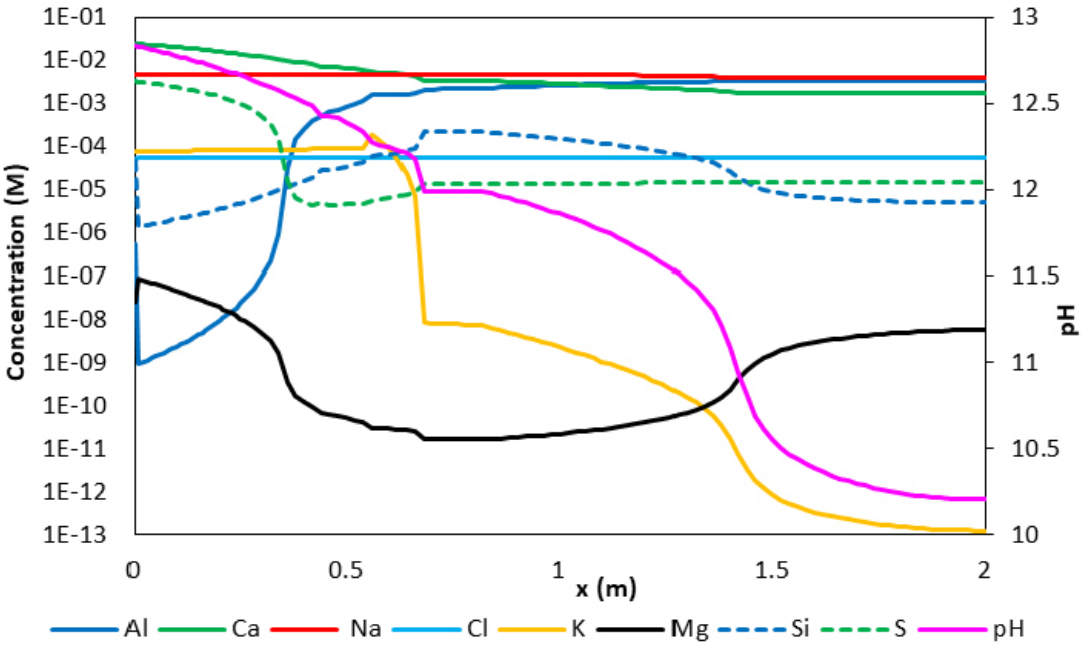

Figure 6-8. *Aqueous species concentration (M) and pH values in the backfill after 100 000 years.*

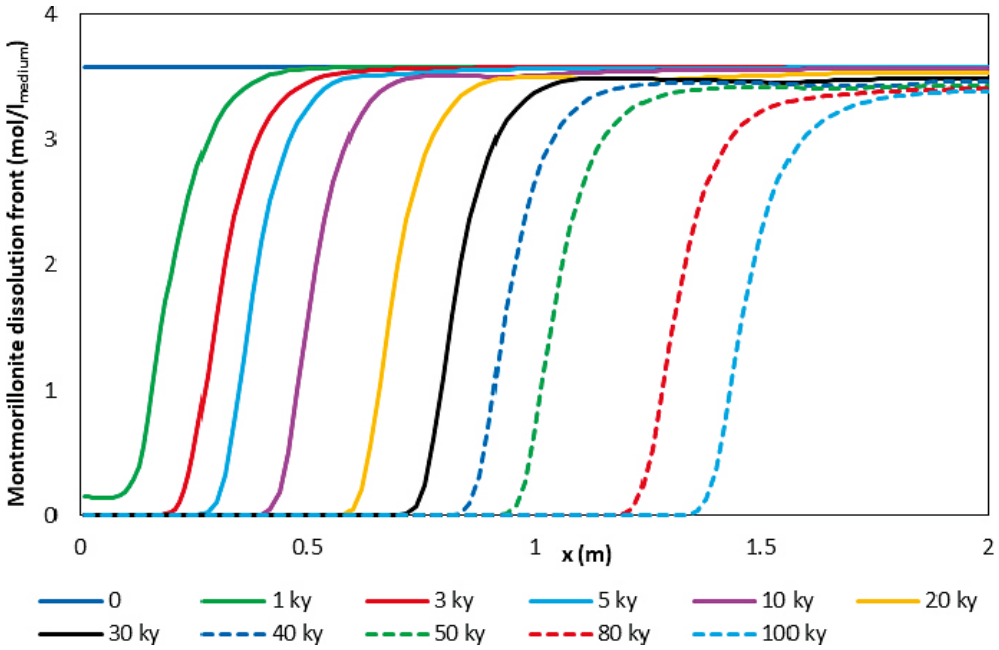

Figure 6-9. *Montmorillonite dissolution front at different times (mol/litre of medium) predicted in the simplified reference case.*

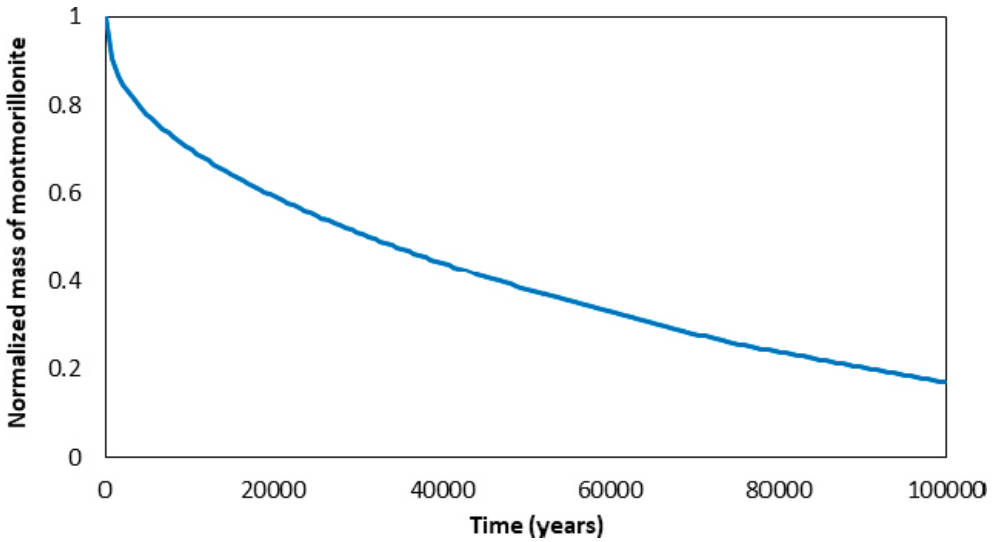

Figure 6-10. *Normalized mass or mass fraction of montmorillonite (remaining mass divided by initial mass) in the bentonite backfill as a function of time (years). The integrated value of the remaining mass of montmorillonite at each time step is normalized with the initial value.*

If the progress of the dissolution front (defined as the distance from the cementitious source at which montmorillonite concentration is half of the initial value) is plotted as a function of the square root of time, a linear evolution may be observed (Figure 6-11). This relation suggests that the rate limiting factor for dissolution is diffusion and not the kinetics rate law used in the simulation (Equation 4-4).

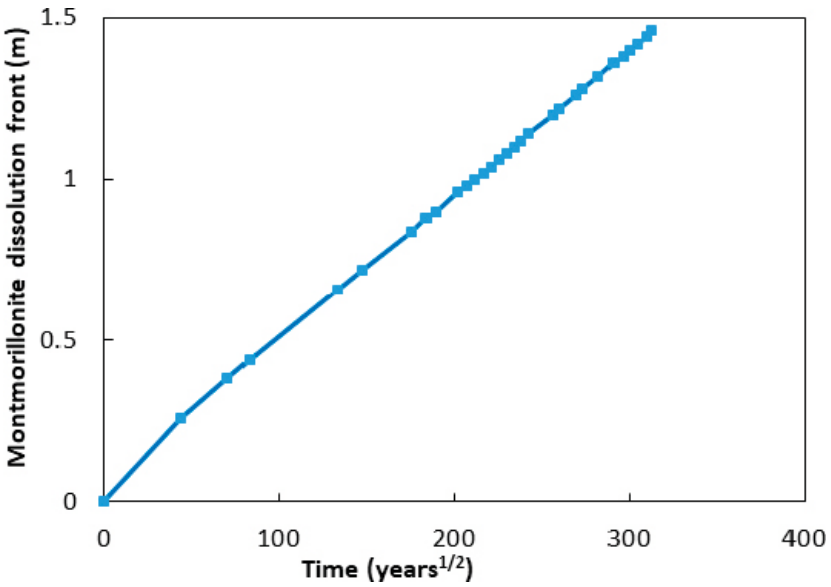

Figure 6-11. *Evolution of the dissolution front (defined as the distance at which the montmorillonite concentration is half of its initial value) plotted against the square root of time (years$^{1/2}$).*

6.3 Effect of the diffusion coefficient in bentonite (#3)

The diffusive character of the dissolution process for the reference case for an effective diffusion coefficient of 1.2×10^{-10} m^2/s can be clearly observed in Figure 6-11. An additional simulation (case 3) is performed using a diffusion coefficient that is one order of magnitude smaller, i.e. 1.2×10^{-11} m^2/s. The results after 100 000 years in terms of montmorillonite dissolution depth are presented in Figure 6-16 and compared to the rest of the simulation cases. The model predicts that the montmorillonite dissolution depth reaches 0.5 m, compared to 1.5 m in the reference case. The values of these dissolution depths are in relatively good agreement with the results obtained by Gaucher et al. (2004) for MX-80 bentonite when assuming a diffusion coefficient of 1×10^{-11} m^2/s and 1×10^{-10} m^2/s, respectively. The montmorillonite mass loss in the backfill after 100 000 years is 28.5 % (Figure 6-17), compared to 75.7 % in the reference case. These results indicate a dissolution rate that is ~3 times slower than the reference case.

Given that the dissolution process is governed by diffusion (see previous section) changes in the effective diffusion coefficient lead to significant changes in the rate of dissolution. In fact, the results indicate that a decrease of the diffusion coefficient by a factor of 10 leads to a 3 times slower advance of the dissolution front. The latter value is very close to the square root of 10, i.e. 3.16, which would result from a purely diffusive system. As expected, the chemical processes occurring in this case are equivalent to the ones observed in the reference case.

6.4 Effect of reactive surface area (#4 to #6)

Another potentially important parameter affecting the results is the reactive surface area used in the montmorillonite dissolution rate law. This value is fixed to 800 m^2/g in the reference case. However, the reactive surface area value has some uncertainty. Two sensitivity cases using a reactive surface area of 30 m^2/g have been implemented (cases 4 and 6). This value is close to typical BET surface area measurements, see e.g. Karnland (2010). This implies a reduction of 26 times of the reactive surface area compared to the reference case. The difference between these two sensitivity cases is that the effective diffusion coefficient is either 1.2×10^{-10} m$^2 \cdot$s^{-1} (as in the reference case) or 1.2×10^{-11} m$^2 \cdot$s^{-1} (as case 3). A lower reactive surface area leads to a reduction in the dissolution depth. As shown in Figure 6-16, after 100 000 years, the montmorillonite dissolution front is predicted to be much less steep than in the reference case or case 3. In other words, the reduced dissolution rate makes the alkaline plume diffuse into the backfill before it is consumed in the dissolution reaction. However, the montmorillonite mass loss in the backfill as a function of time (Figure 6-17) shows that after 100 000 years, the difference

compared with the reference case is less than 4 %. In turn, combining a low reactive surface area with a low effective diffusion coefficient (case 6) leads to the same results as for case 3. Thus, it may be concluded that the total montmorillonite mass dissolved is not sensitive to the reactive surface area in the range 30 to 800 m^2/g. The main impact of the reactive surface area is a broader distribution of the dissolution front across the backfill thickness.

As stated in Section 4.2, the value of the montmorillonite reactive surface area has been analysed in several research works, suggesting that its value might be several orders of magnitude smaller than previously thought due to its localization at the particle edges and due to the masking effect. For this reason, the reference case has also been computed using the reactive surface area value 0.03 m^2/g (case 5) obtained with the analytical expression derived by Terada et al. (2019). Figure 6-16 and Figure 6-17 show that the lower reactive surface area significantly reduces the mass of montmorillonite dissolved after 100 000 years compared to case 4. In turn, the results indicate that the system becomes much more sensitive to the value of the reactive surface area as it decreases well below 30 m^2/g.

6.5 Effect of boundary conditions

6.5.1 Host-rock boundary condition (#7)

The boundary condition imposed on the right-hand side boundary of the model in the reference case is a no concentration gradient (closed boundary). In case 7, this boundary condition is modified to consider a fixed concentration corresponding to the composition of groundwater. The chemical composition of the groundwater used in this sensitivity case is presented in Table 6-1. It is the same composition as used in other near-field studies of SFL (see e.g. Idiart and Shafei 2019), although equilibrated at 15 ºC.

The results of this sensitivity case in terms of the mass of montmorillonite dissolved and travel distance of the dissolution front are similar to those obtained for the reference case (Figure 6-16 and Figure 6-17), although dissolution is slightly reduced. The dissolution front is located 1.4 m from the cementitious source after 100 000 years, around 10 cm closer to the cementitious source than in the reference case. This reduction is a result of partial out diffusion of the alkaline plume along the bentonite-rock interface. In terms of mineral phase assemblage, more differences are observed. The influence of groundwater on the right boundary is observed as a replacement of small amounts of montmorillonite by illite and clinochlore. A small amount of quartz also remains there, as opposed to the reference case. In addition, calcite and phillipsite precipitate in the dissolution front at higher rates than in the reference case. The spatial distribution of these mineral phases is presented in Figure 6-12 after 100 000 years.

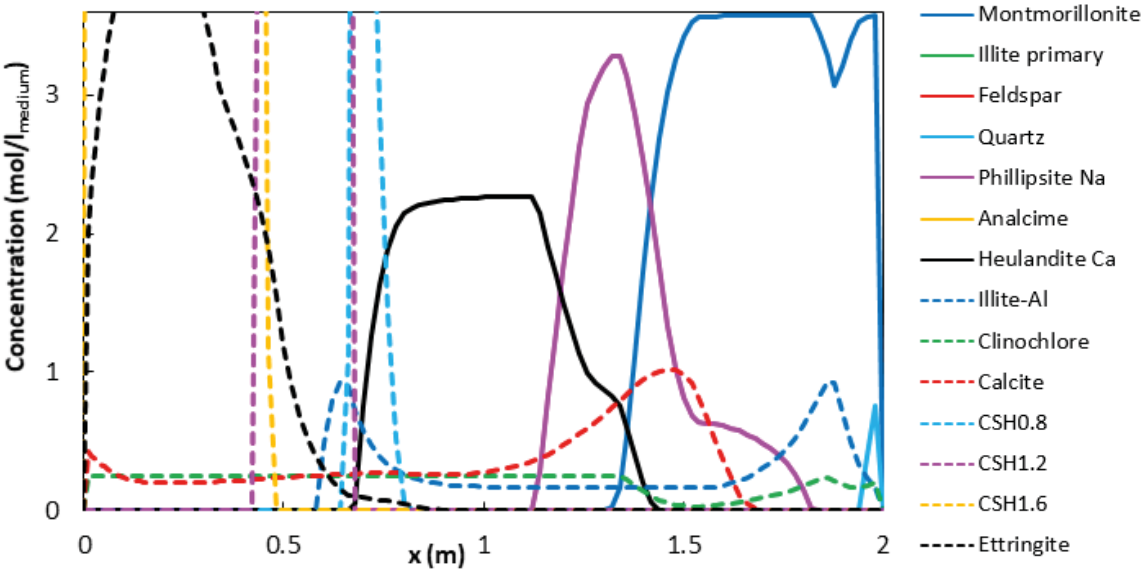

Figure 6-12. *Profile of mineral phase concentrations (mol/litre of medium) after 100 000 years in case 7.*

6.5.2 Concrete porewater boundary condition (#8)

The mass of montmorillonite that dissolves in the reference case (case 2) is substantial. This is mainly due to the aggressive (highly alkaline) boundary condition assumed as the cementitious source in the simulation. To study the influence of this boundary condition, an additional simulation has been implemented assuming a less aggressive scenario. Namely, a fixed concentration boundary condition is still used, although the composition of the concrete porewater is not in equilibrium with portlandite but with a C-S-H gel (Ca/Si ratio = 1.2). This water has a lower pH value, a reduced concentration of calcium and a higher concentration of silica. Both porewater compositions are presented and compared in Table 6-2.

After 100 000 years, the montmorillonite dissolution depth in case 8 is greatly reduced compared to the reference case (1.5 m) to 0.7 m (Figure 6-13). Moreover, a significant amount of quartz remains in the backfill. This is a result of the less alkaline nature of the cementitious source considered in this case. In terms of secondary phases, the main difference with the reference case is the lack of ettringite and C-S-H gels with high Ca/Si ratios (only C-S-H with Ca/Si = 0.8 forms). In addition, the only zeolite that forms is calcium heulandite.

Table 6-2. Concrete porewater compositions used as boundary conditions for reference case (equilibrated with portlandite) and case 8 (equilibrated with a C-S-H gel, Ca/Si ratio = 1.2).

	Concrete porewater in equilibrium with portlandite	Concrete porewater in equilibrium with C-S-H 1.2 gel
pH	12.83	11.42
Temperature (°C)	15	15
Solutes (totals)	**Concentration (M)**	
Al	5.54×10^{-7}	5.54×10^{-7}
C	1.00×10^{-5}	1.00×10^{-5}
Ca	2.43×10^{-2}	2.68×10^{-3}
Cl	5.55×10^{-5}	5.55×10^{-5}
K	7.60×10^{-5}	7.60×10^{-5}
Mg	2.53×10^{-8}	2.53×10^{-8}
Na	4.79×10^{-3}	4.79×10^{-3}
S(6)	3.29×10^{-3}	3.29×10^{-3}
Si	4.52×10^{-5}	2.23×10^{-3}

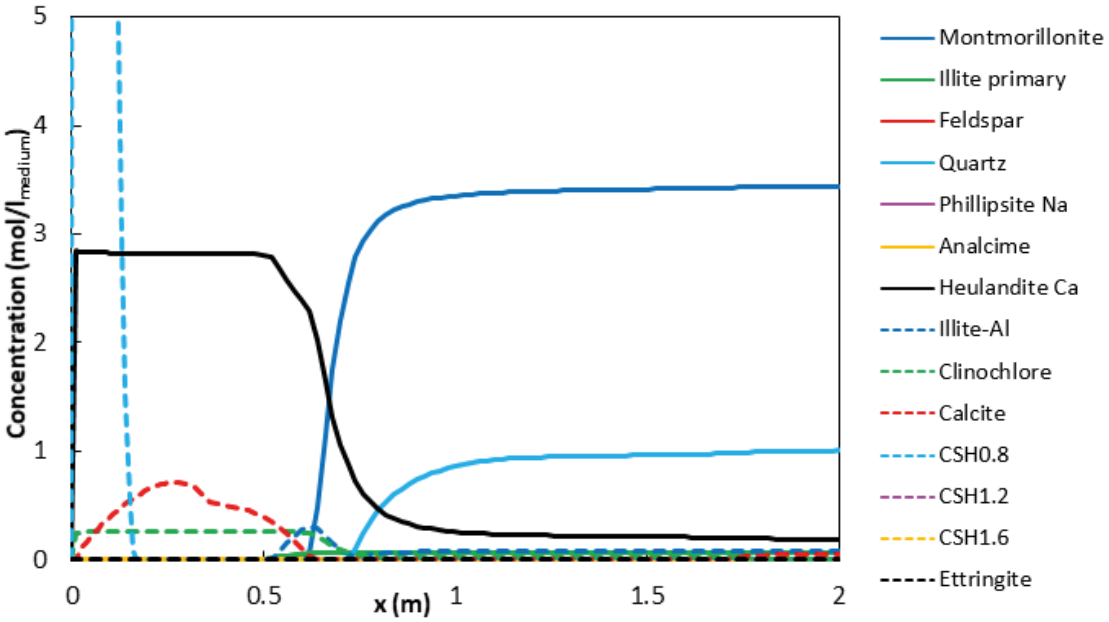

Figure 6-13. Profile of mineral phase concentration (mol/litre of medium) after 100 000 years in case 8.

6.6 Effect of secondary minerals formed (#9 to #11)

Three sensitivity cases (cases 9 to 11 in Table 3-1) have been implemented with different mineral assemblages from that used in the simplified reference case presented in Section 6.2. As expected, the mineral dissolution processes are different in each case, but all simulations follow approximately the alteration sequence presented by Savage et al. (2007) and summarized in Figure 4-3.

The analysis is focused on the dissolution of montmorillonite and its relation to the set of minerals allowed to precipitate. The results of these sensitivity cases, as summarized in Figure 6-16 and Figure 6-17, clearly show that the dissolution depth is directly influenced by the set of secondary minerals. The minerals that form as a result of the reactions in the alkaline plume determine the proximity of the bentonite porewater to equilibrium with montmorillonite. This is especially important for the kinetic rate law used in this study (Equation 4-4), which depends directly on the saturation index of montmorillonite *via* the 'Oda term'.

In general, precipitation of secondary minerals consumes not only part of the ions diffusing from the cementitious source, but also those released by montmorillonite dissolution. Therefore, formation of secondary minerals helps maintain the far-from-equilibrium geochemical conditions that favour a faster dissolution rate. On the other hand, preventing secondary mineral formation in the simulations, as in the idealized case 1 (Section 6.1) leads to a situation in which the release of ions from montmorillonite dissolution quickly equilibrates the porewater with that mineral. As a result, dissolution is greatly reduced, as shown in Figure 6-16. The dissolution depth in this case is less than 0.4 m, compared to 1.5 m in the simplified reference case.

An intermediate situation between the reference case (case 2) and the idealized case (case 1) is predicted when the set of secondary minerals selected leads to a smaller mass (in moles) of precipitated minerals. The results of cases 9, 10 and 11 show that, compared to the reference case, the lesser the moles of secondary minerals formed, the smaller the dissolution depth. For instance, including crystalline C-S-H phases (jennite, tobermorite, and gyrolite) in the simulation (case 9) leads to a lower mass of secondary minerals formed compared to the reference case, and thus to a smaller dissolution depth (1.1 m instead of 1.5 m with only amorphous C-S-H phases). On the other hand, excluding illite from primary and secondary minerals has a small impact on montmorillonite dissolution (Figure 6-16). Finally, adding crystalline C-S-H as well as C-A-S-H secondary phases, as proposed by Soler and Mäder (2010), leads to an intermediate situation between the reference case and case 9, with a dissolution depth of around 1.3 m. Obviously, all of these simulation cases lead to larger dissolution depths when compared to the idealized case 1 (Section 6.1).

6.7 Thermodynamics versus kinetics dissolution (#12)

The results of the reference case (case 2) show a linear relation between the montmorillonite dissolution depth and the square root of time (Figure 6-11), suggesting that the rate limiting factor for dissolution is diffusion and not the kinetics rate. This is due to the large reactive surface area assumed in case 2 (800 m^2/g). The last sensitivity case (case 12) considers montmorillonite dissolution under thermodynamic equilibrium with the aim of verifying this hypothesis. The results of case 12 are compared with the results of the simplified reference case (case 2) in Figure 6-14 and Figure 6-15. A very good agreement is found between the two simulations, indicating that the kinetics of montmorillonite dissolution is not governing the evolution of the dissolution depth in this particular setup. Instead, diffusion is the main controlling process.

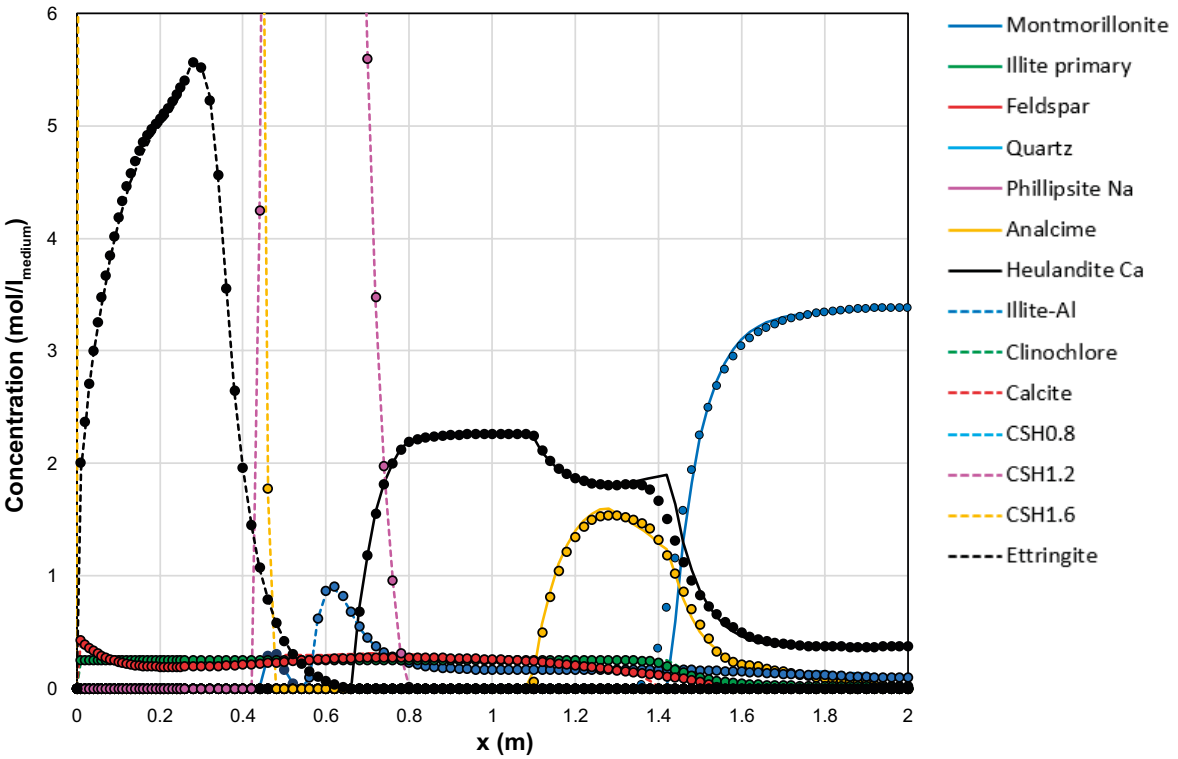

Figure 6-14. *Profile of mineral phase concentration (mol/litre of medium) after 100 000 years. Results corresponding to the reference case 2 (dots) and case 12 (solid and dashed lines).*

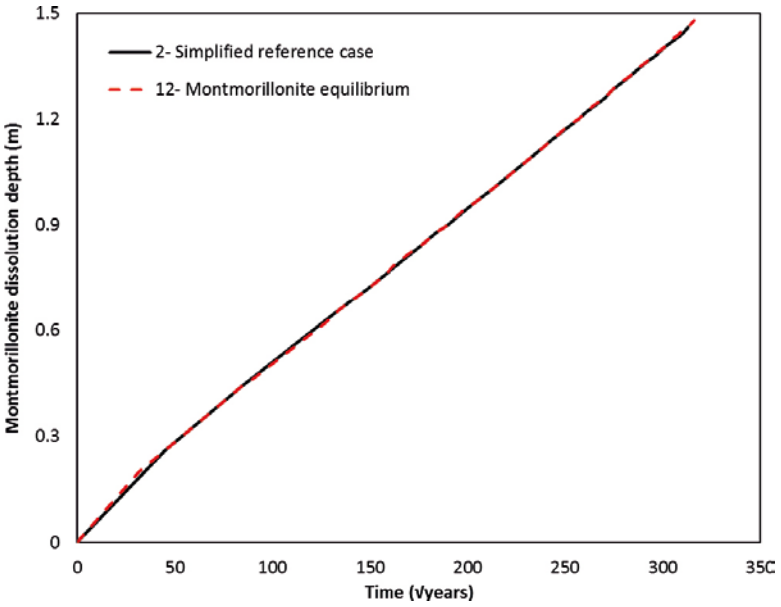

Figure 6-15. *Evolution of the dissolution front (defined as the distance at which the montmorillonite concentration is half of its initial value) plotted against the square root of time (years$^{1/2}$): reference case (case 2) and case 12 (montmorillonite under thermodynamic equilibrium).*

6.8 Summary of results

This section summarizes the differences between the cases simulated with the simplified setup (only bentonite backfill) in terms of montmorillonite dissolution. Figure 6-16 and Figure 6-17 show the montmorillonite profile after 100 000 years, and the evolution of the normalized mass of montmorillonite, respectively.

As previously underlined, the largest differences are predicted when changing three principal characteristics of the model: effective diffusion coefficient, concrete porewater boundary condition and the set of secondary minerals. The degradation process is mainly driven by diffusion; the value of the effective diffusion coefficient of different aqueous species in bentonite is of major importance. Decreasing the value of the diffusion coefficient by one order of magnitude reduces the montmorillonite mass loss from 75.7 % (case 2) to 28.5 % (case 3). The fixed concrete porewater composition used as left boundary condition is also a main matter of concern. When assuming a less aggressive porewater (in equilibrium with C-S-H 1.2 instead of portlandite) the final montmorillonite degradation profile reaches half the depth of the reference case. The set of secondary minerals is also important mainly due to the nature of the dissolution rate law (Sato-Oda) selected for this work. Although the set of minerals adopted in the reference case is thought to be a realistic one, large differences in the total degradation may result when secondary mineral assemblages that lead to smaller precipitation are implemented. Differences between cases for which the right boundary condition or the montmorillonite reactive surface area are changed, are of a lower magnitude in terms of montmorillonite mass loss, except for case 5, where the reactive surface area is very small.

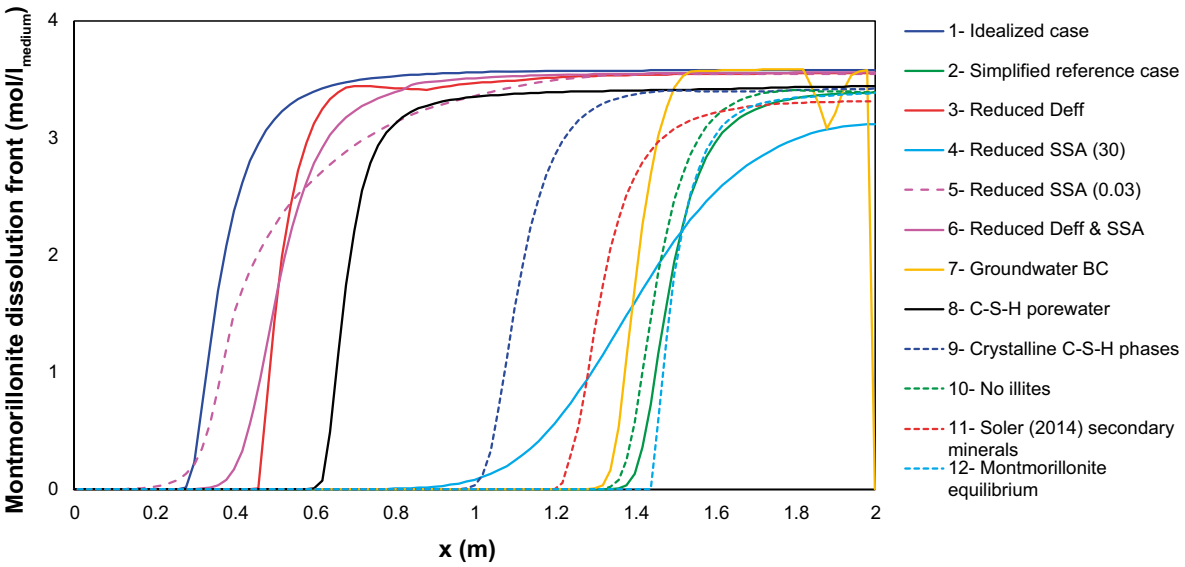

Figure 6-16. *Montmorillonite dissolution front (mol/litre of medium) after 100 000 years: comparison between the idealized, reference, and sensitivity cases for the simplified analysis.*

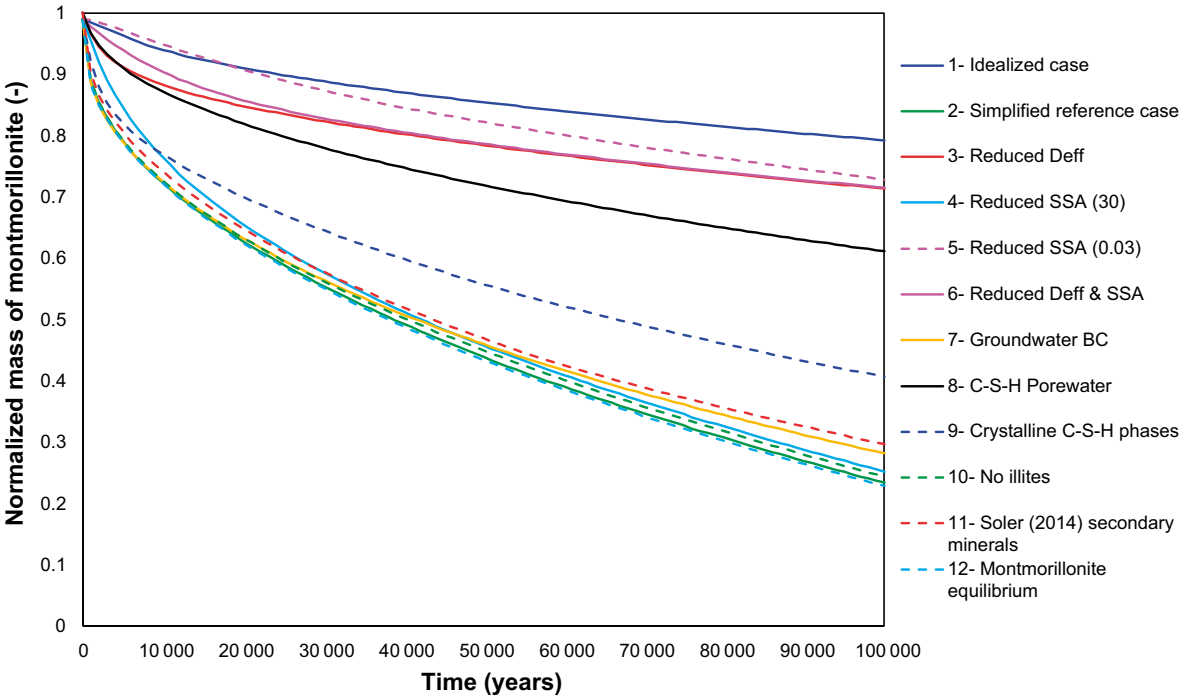

Figure 6-17. *Normalized mass or mass fraction of montmorillonite (remaining mass divided by initial mass) in the bentonite backfill as a function of time (years): comparison of all simulated (simplified analysis) cases.*

7 Full analysis (concrete–bentonite interaction)

The results of the full analysis that explicitly considers the interaction between bentonite and concrete are presented and discussed here (see also Section 3). Figure 7-13 gives a summary of the results and a comparison between the different simulation cases (in Table 3-2). The results of the 1D reactive transport simulations are presented in the form of spatial distribution profiles at given times, temporal evolution of variables at a fixed point, or time evolution of integrated values for the entire bentonite backfill. The equivalent mass of montmorillonite is calculated at a given time using Equation 6-1, with a value of L of 2.3 m (Section 4).

7.1 Results of idealized case (#13)

As pointed out in Section 6.6, formation of secondary minerals is one of the key factors affecting montmorillonite dissolution. As in the simplified analysis, the first simulation considers an idealized case (case 13) in which the formation of secondary phases is not allowed. Therefore, only montmorillonite is included in the bentonite paragenesis, with cation exchange reactions as in the full reference case (case 14). The concrete and waste domains are treated similarly as in the full reference case, i.e. formation of secondary minerals is included.

In this case, the montmorillonite dissolution depth after 100 000 years is less than 0.10 m (Figure 7-1), with only 6.5 % of the initial montmorillonite mass predicted to dissolve. This corresponds to ~4.5 times less than in the full reference case (case 14), see Figure 7-13. The absence of secondary minerals in the bentonite backfill results in a fast equilibration of the bentonite porewater with this mineral and thus the decrease in the dissolution kinetic rate. This is observed in Figure 7-2, showing the evolution of the saturation index in the backfill at different distances from the interface. Negative values indicate that the pore solution is under saturated with respect to montmorillonite and thus dissolution proceeds. Positive values indicate super saturation of the pore solution, although in this work montmorillonite is only allowed to dissolve. The saturation indexes in this figure are small and not very far from equilibrium. As shown in Figure 4-6, the time needed to dissolve all montmorillonite completely from 1 litre of bentonite assuming a SI = −0.5 is larger than 100 000 years independently of the pH of the pore solution. Thus, the results of case 13 are as expected.

In the concrete domain, a more advanced dissolution of primary C-S-H gel (CSH1.6) is observed compared to in the full reference case (Section 7.2), with high concentrations of medium and low Ca/Si ratio C-S-H gels and potassium saponite (Figure C-1 in Appendix C).

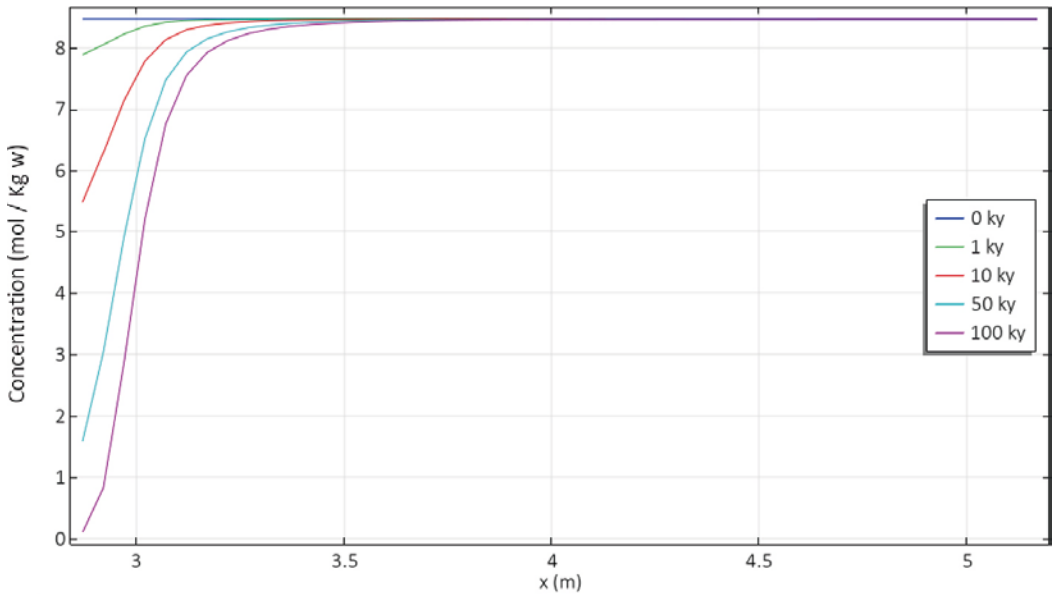

Figure 7-1. *Profiles of montmorillonite concentration (mol/kgw) in the bentonite backfill at different times.*

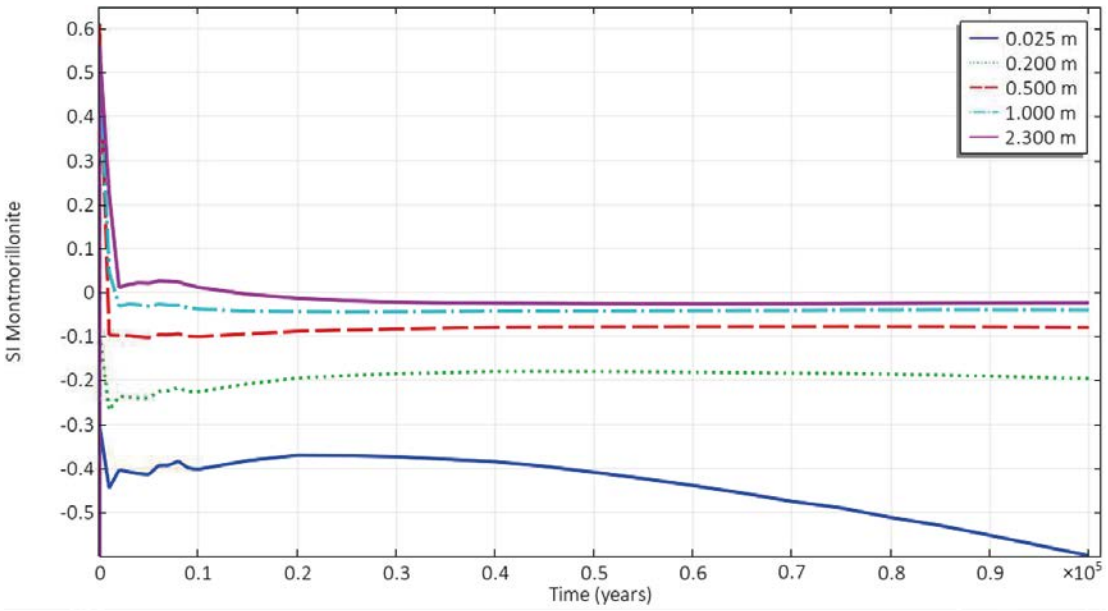

Figure 7-2. *Evolution of the saturation index of montmorillonite, SI (-) at different points in the bentonite backfill, at distances of 0.025, 0.2, 0.5, 1.0 and 2.3 m from the concrete-bentonite interface.*

7.2 Results of full reference case (#14)

Simulation results are presented in Figure 7-3 to Figure 7-12. Overall, the results obtained indicate a degradation of 30 % of the total montmorillonite mass in the bentonite barrier after 100 000 years of interaction with the concrete barrier. Figure 7-3 presents 1D profiles of the evolution of pH of the modelled domains. pH profiles are good indicators of chemical variations in the different domains. The homogeneous pH value in the waste domain for the simulated period indicates that the system works as a mixer, due to a high diffusivity. After 1 000 years, the pH in the vicinity of the concrete-bentonite interface reaches a value of 11.6 on the bentonite side, indicating an increase of 4 pH units. At the same time, on the concrete side pH decreases to a value of 11.9, revealing alkali leachate and portlandite depletion. In the waste domain and the left part of the concrete structure, pH values decrease from 13.6 to 12.8 in the first 30 000 years and are subsequently maintained in time (as portlandite has not been completely dissolved). For the bentonite backfill, pH increases in the entire domain to a value above 8 after 40 000 years and to a value above 10 for the first 0.1 m next to the concrete–bentonite interface (coinciding with full montmorillonite dissolution).

pH values at the concrete–bentonite interface are shown in Figure 7-4. The boundary condition imposed in the simplified analysis (Section 6) is presented together with the results of the full analysis. Two temporal evolution profiles are shown for the interface, corresponding to the values obtained on the concrete side and the bentonite side of this interface. After approximately 15 000 years, the pH on both sides of the interface is practically the same and slowly decreases with time. At early times, diffusion and alkali leaching from concrete lead to a quick change in both domains. From that time on, the remaining portlandite in the concrete structure leads to pH values around 11 at both sides of the concrete–bentonite interface. The boundary condition used in the simplified model (pH = 12.83) is in good agreement with the pH value obtained at late times at the left boundary of the cementitious domains (x = 0 in Figure 7-3). At this boundary, concrete mineralogy remains unaltered throughout the studied period. The pH value of 12.8 is far from the values obtained at the concrete–bentonite interface, which demonstrates the importance of including the concrete–bentonite interaction in the model.

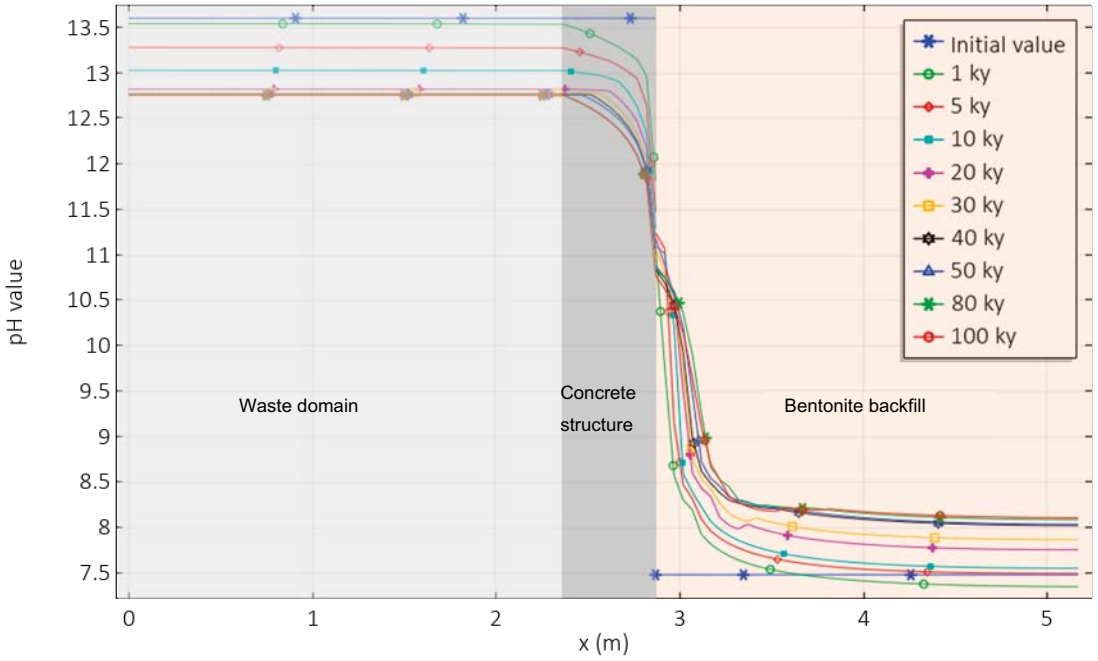

Figure 7-3. *Profiles of pH value at different times.*

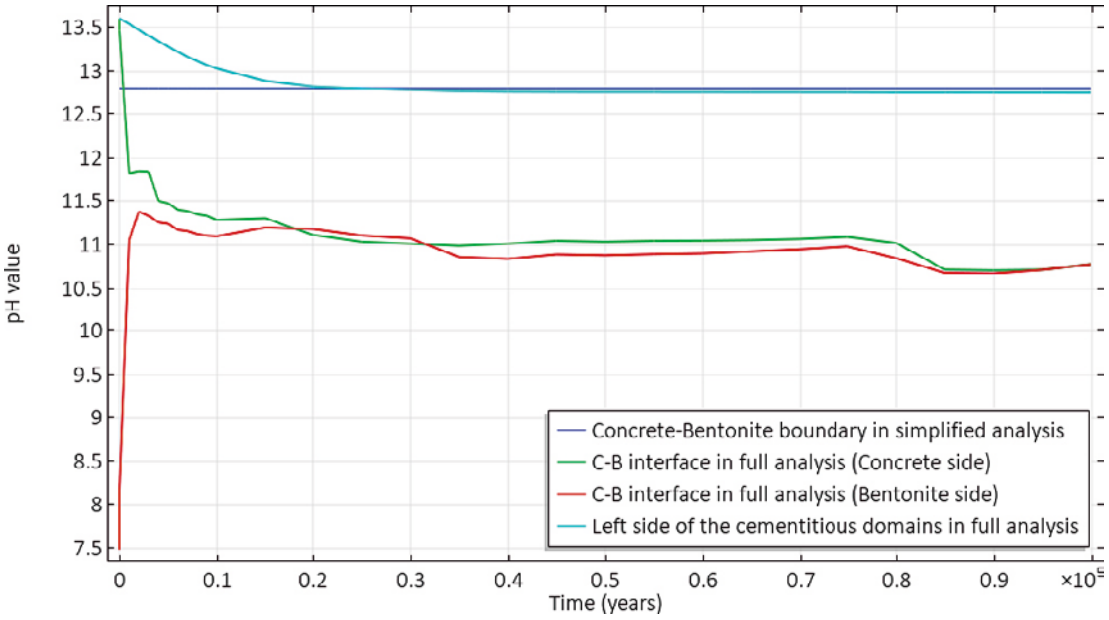

Figure 7-4. *Time evolution of porewater pH values at the concrete-bentonite interface. Comparison between results from the full analysis at both sides of the interface and at the left boundary and the value imposed as boundary condition in the simplified analysis.*

Figure 7-5 to Figure 7-8 present the mineralogical phase assemblages after 100 000 years of interaction. In Figure 7-5, only the main minerals characterizing each system are shown, for clarity. In the concrete structure, portlandite is almost completely depleted, while it remains in the entire waste domain. Primary C-S-H gel (Ca/Si = 1.6) is barely affected, only being replaced by the C-S-H gel with lower Ca/Si ratio (1.2) in the first 0.1 m closest to the concrete–bentonite interface. Bentonite evolution is characterized by the montmorillonite dissolution front, with 0.25 m of complete depletion after 100 000 years. The travel distance of the illite and quartz dissolution fronts is similar to that of the montmorillonite dissolution front, although some reprecipitation of illite appears near the concrete–bentonite interface.

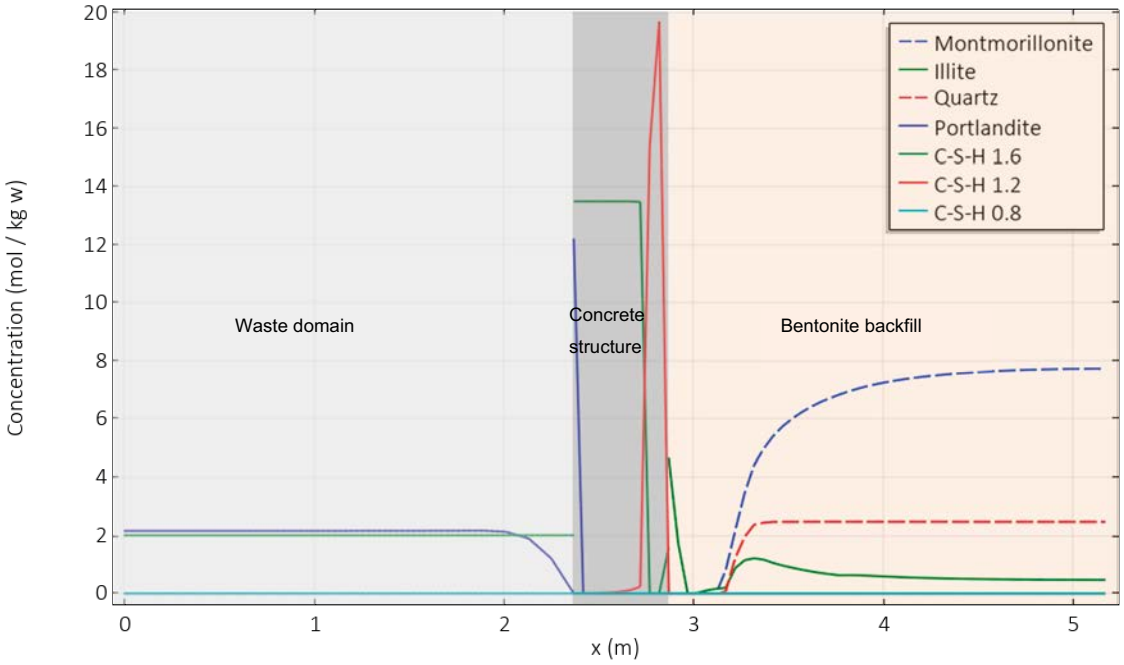

Figure 7-5. *Profiles of mineral phase concentration (mol/ kgw) after 100 000 years. Complete distribution of main minerals in the model.*

The complete set of (primary and secondary) minerals after 100 000 years in the cementitious domains is shown in Figure 7-6. Only the last meter of these domains next to the bentonite backfill is presented, as no mineral changes occur in the remaining section of the waste domain (Figure 7-5). Apart from some portlandite dissolution, no more differences are observed in the waste domain. In turn, ettringite formation is predicted in the entire concrete structure as a result of in-diffusion of sulphate from the bentonite backfill (gypsum is present as accessory mineral). Major changes are also observed at the concrete–bentonite interface, in a region of 0.1 m, where dissolution of all primary minerals has led to the precipitation of small amounts of calcite and potassium saponite.

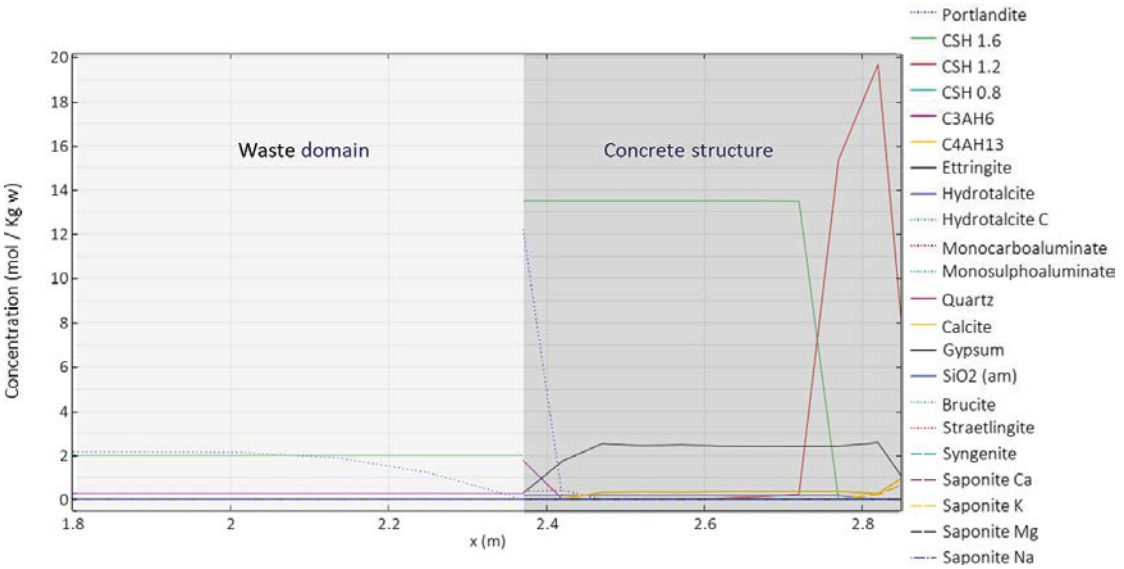

Figure 7-6. *Profiles of mineral phase concentration (mol/ kgw) after 100 000 years in the cementitious domains close to the concrete-bentonite interface. The waste domain is only partly shown.*

Figure 7-7 presents spatial distribution profiles of the different mineral phases in the bentonite backfill after 100 000 years. Zeolites (sodium phillipsite and calcium heulandite) are present in the entire backfill, although at higher concentrations in the first centimetres from the concrete–bentonite interface, where primary minerals are completely dissolved. Near the interface, a significant precipitation of calcite and chlorite (clinochlore) is predicted. It is noted that Nakabayashi (2014) predicted a similar precipitation pattern of sodium phillipsite across the entire bentonite thickness with montmorillonite also present in the entire domain. During the first ~10 000 years, gypsum precipitation before its depletion is observed (not shown), and also a relatively fast increase in phillipsite concentration, as a result of the fast sodium-to-calcium exchange in the smectite interlayer.

The sequence of secondary minerals present at the end of the simulation is shown schematically in Figure 7-8. The sequence includes the formation of zeolites with different Al/Si ratios followed by illite. This is followed by the formation of calcite and clinochlore. Compared with the results of the simplified analysis (Figure 6-7), the main difference is the absence of ettringite and C-S-H gels in the full analysis (Figure 7-8). This is due to the more aggressive boundary condition used in the simplified analysis, in which the boundary porewater has a pH of 12.83 and is in equilibrium with these cementitious phases.

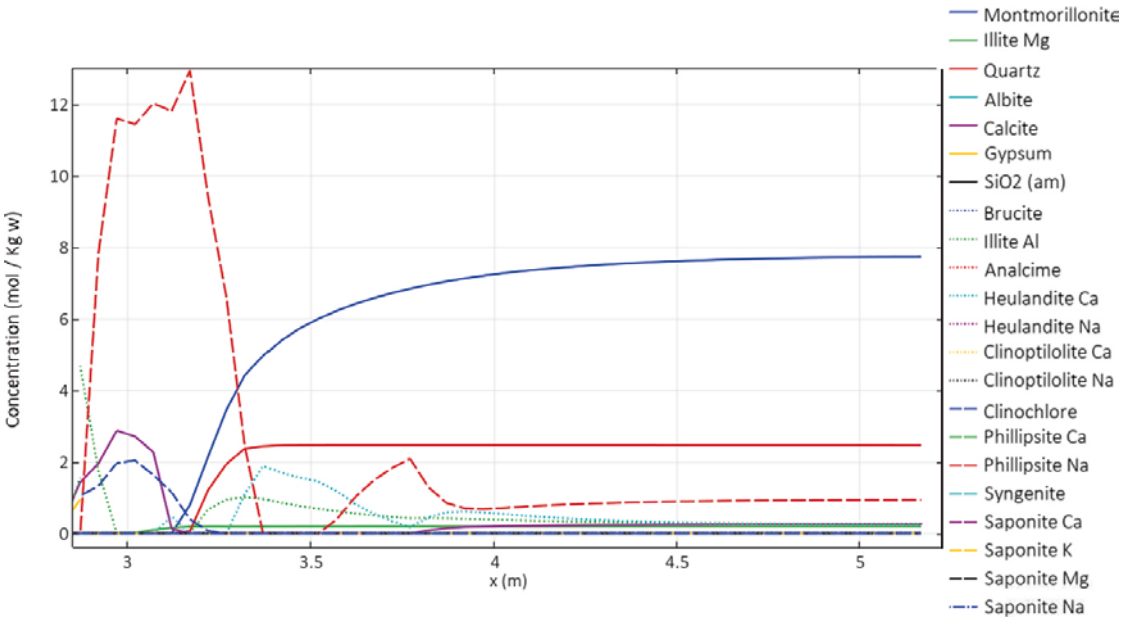

Figure 7-7. *Profiles of mineral phase concentration (mol/kgw) after 100 000 years in the bentonite backfill.*

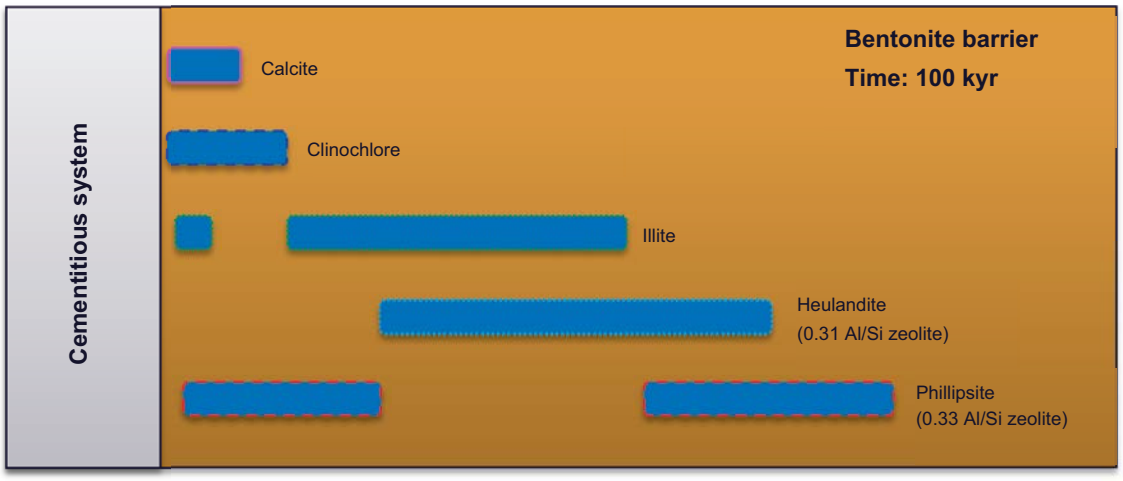

Figure 7-8. *Sequence of secondary minerals formed in the bentonite backfill after 100 000 years, as identified from Figure 7-6.*

As discussed in Section 4, the dissolution rate of montmorillonite does not only depend on pH (Figure 7-3 and Figure 7-4) but also on the proximity to equilibrium between phases (pore solution and mineral). This proximity is represented by the saturation index (SI) of montmorillonite, which is shown in Figure 7-9 together with the concentration of montmorillonite. In this figure, the saturation index is only plotted where the montmorillonite concentration is higher than zero. In this way, the minimum saturation index at which montmorillonite is dissolving can be more clearly identified. It may be observed that the saturation index ranges between −0.34 and −1.0 away from the concrete–bentonite interface and between −1.5 and −3.7 at the dissolution front. The sensitivity of the dissolution rate to these changes in the saturation index is depicted in Figure 4-6.

The concentration of aqueous (total) species at the end of the simulation period are presented together with pH values in Figure 7-10. Chloride, potassium, and sodium are homogeneously distributed in the model. The calcium concentration in the waste domain is uniform, while in the bentonite backfill spatial variations are very small. Between these two domains, the concentration of Ca in the concrete structure varies smoothly, dependent also on the C-S-H composition in the concrete structure. After 100 000 years, the sulphate concentration is much lower than initially due to the formation of ettringite. The aluminium profile is conditioned by a large number of phases (ettringite, saponites, and zeolites). The magnesium concentration is low in the cementitious domains and much larger where montmorillonite is present. The discontinuity at the concrete–bentonite interface is due to clinochlore precipitation occurring only on the bentonite side.

Figure 7-11a presents the evolution of the normalized mass of montmorillonite throughout the studied period, i.e. the equivalent mass of montmorillonite remaining (calculated using Equation 6-1) normalized with the initial montmorillonite mass of the bentonite backfill. The process is initially non-linear, reaching a total mass loss of 17 % in the first 20 000 years. Thereafter, an approximate linear trend is observed. After 100 000 years 70 % of the initial montmorillonite mass is predicted to remain. Extrapolation of this linear trend indicates that full montmorillonite dissolution in the backfill would be reached after ~530 000 years, provided that there is a sufficient supply of alkalinity.

The progress of the montmorillonite dissolution front is plotted as a function of the square root of time in Figure 7-11b. Although not far from being linear, the process in this full analysis is shown to not solely be governed by diffusion in the bentonite. The time needed for solutes to diffuse in the concrete barriers towards the concrete–bentonite interface, as well as the alkalinity of the plume reaching the bentonite backfill, are not constant in time (Figure 7-4).

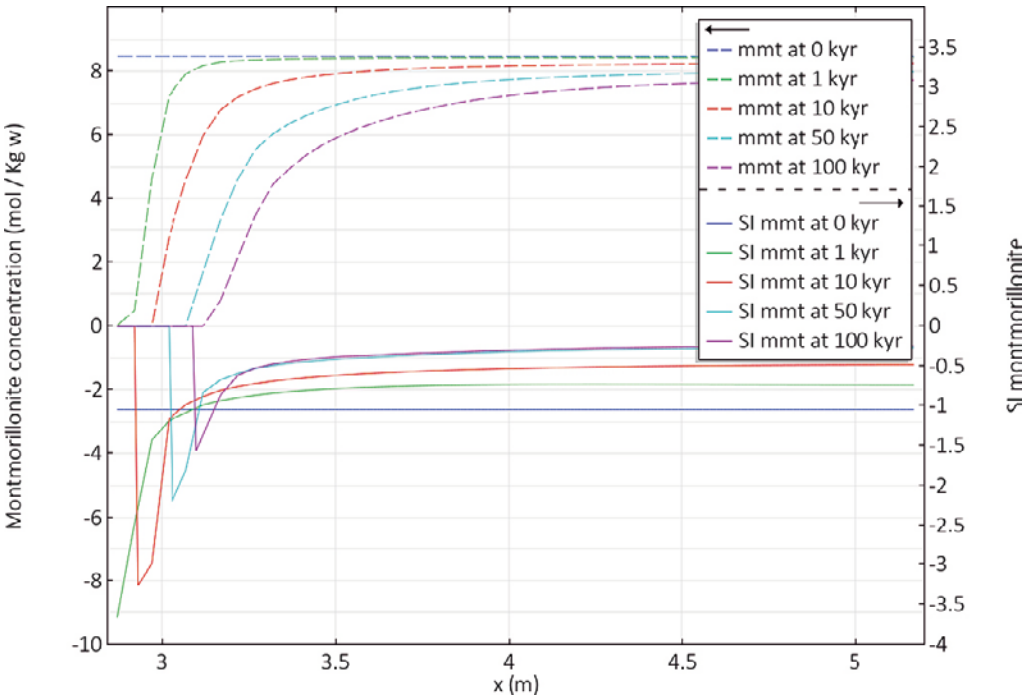

Figure 7-9. *Profiles of montmorillonite concentration (mol/kgw) and saturation index (-) at different times (0, 1, 10, 50, and 100 thousand years).*

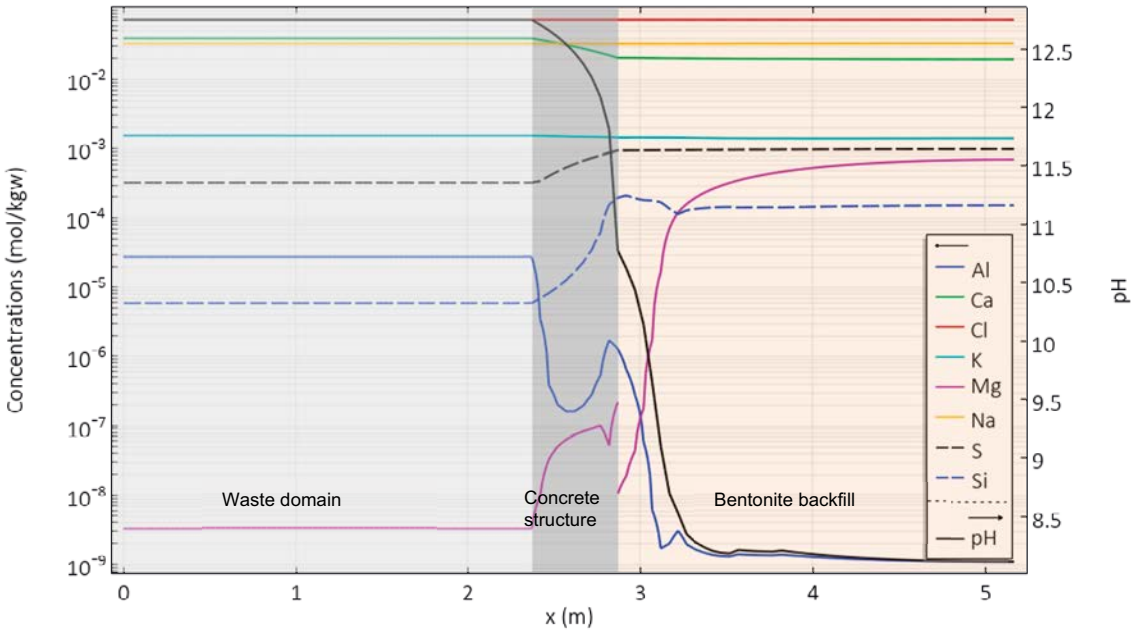

Figure 7-10. *Aqueous species concentration (M) and pH values in the model after 100 000 years.*

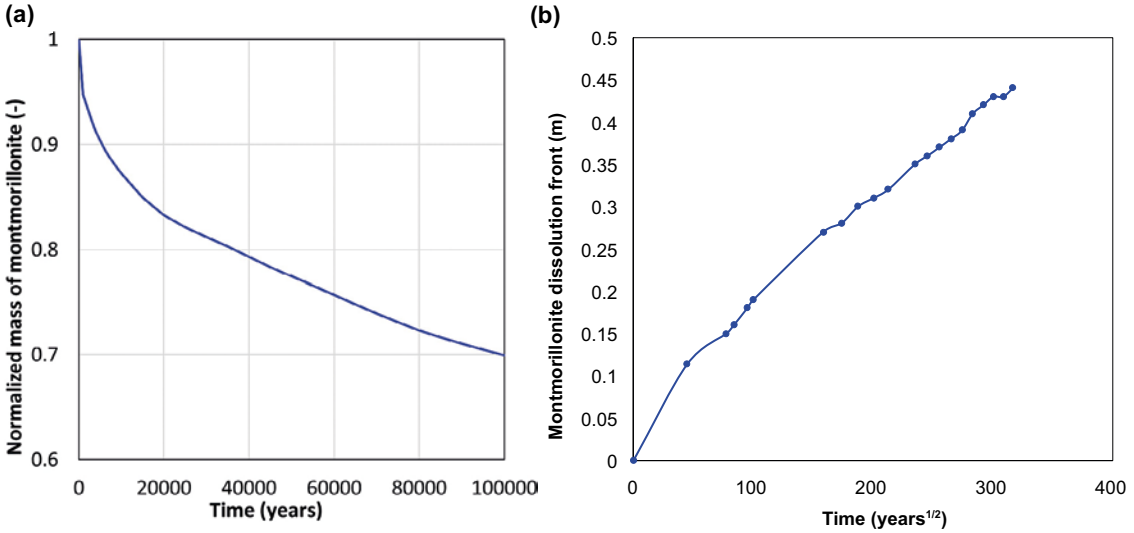

Figure 7-11. *(a) Normalized mass or mass fraction of montmorillonite (remaining mass divided by initial mass) in the bentonite backfill as a function of time (years). (b) Evolution of the dissolution front (defined as the distance at which the montmorillonite concentration is half of its initial value) plotted against the square root of time (years$^{1/2}$).*

Even though the reactive transport simulations presented here do not consider porosity changes due to mineral volume changes, the evolution of porosity can still be monitored. The results of the simplified and full reference cases are depicted in Figure 7-12 in terms of porosity profiles in the modelled domains at the time clogging is first observed in the concrete–bentonite interface. Porosity clogging is predicted by both models due to precipitation of calcite in the full analysis and the formation of cementitious phases in the simplified analysis. This occurs after 2 000 and 300 years, respectively, i.e. a very short period. As stated in Section 4, hydro-chemo-mechanical couplings are expected to play an important role in determining porosity changes.

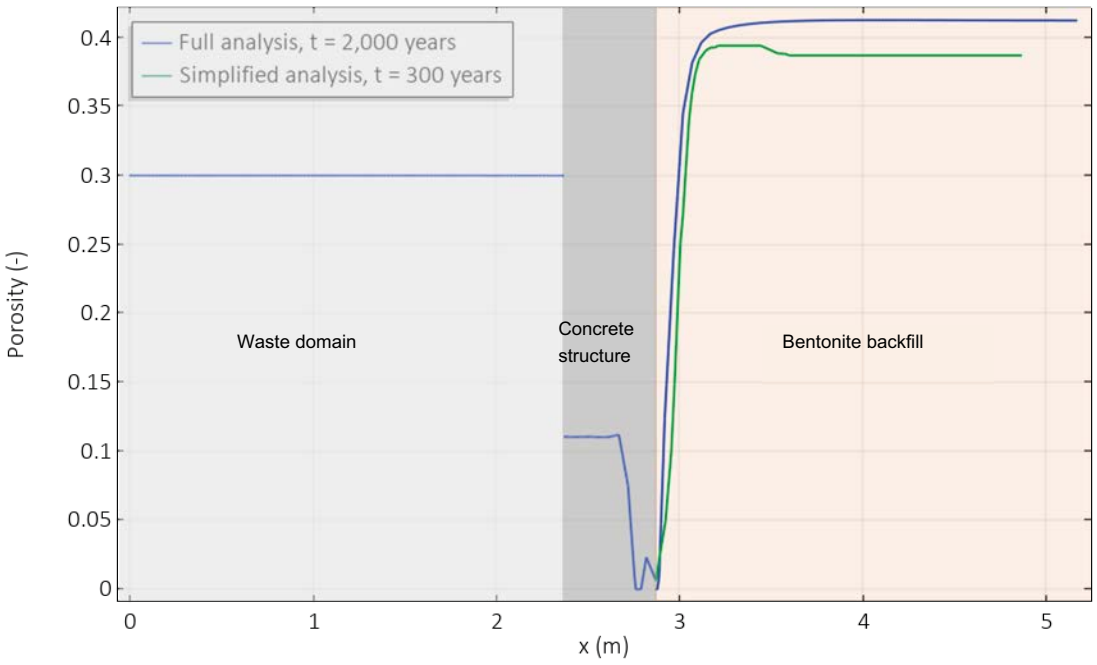

Figure 7-12. *Porosity profiles for the full reference case (case 14) at 2 000 years and the simplified reference case (case 2) at 300 years.*

7.3 Effect of montmorillonite reactive surface area (#15)

As with case 5, the reference case has been simulated using the reduced reactive surface area value (0.03 m^2/g) obtained with the correlation presented by Terada et al. (2019). Again, the model predicts a quite significant reduction of the total mass of montmorillonite dissolved after 100 000 years. Even less montmorillonite is predicted to dissolve compared to the idealized case (case 13), preserving more than 95 % of the initial mass (Figure 7-13).

7.4 Effect of the diffusion coefficient in concrete (#16 and #17)

Figure 7-11b highlights the importance of the diffusion rate in the different modelled domains for the degradation process. As presented in Figure 7-3, the waste domain acts as a mixer due to the higher diffusivity of solutes compared to in the concrete structure (a 100 times higher diffusion coefficient, Table 4-1). The concrete structure, the domain with the lowest solute diffusivity (lowest value of D_e), limits the supply of alkalinity to the bentonite backfill and thus controls the dissolution rate of montmorillonite. Therefore, case 16 ($D_e = 1.0 \times 10^{-12}$ m^2/s) and case 17 ($D_e = 3.5 \times 10^{-11}$ m^2/s) in Table 3-2 study the sensitivity of the results to changes in the solute diffusivity in the concrete structure. Changing the diffusivity in the concrete structure ($D_e = 3.50 \times 10^{-12}$ m^2/s in the reference case) affects mainly the montmorillonite dissolution depth, with small influence on the chemical degradation sequence.

In case 16 (D_e is 3.5 times smaller than in the full reference case) ~ 78 % of the montmorillonite mass in the bentonite backfill remains at the end of the studied period (Figure 7-13). In other words, montmorillonite degradation is 30 % less with respect to the reference case. Results (not shown) indicate that 50 % of the initial mass of portlandite is preserved in the concrete domain, while it is almost entirely depleted in the reference case. Moreover, some brucite and sodium phillipsite precipitation next to the concrete–bentonite interface is observed. On the bentonite side, the main difference is that no calcium heulandite precipitates in case 16 after 100 000 years, while calcite and clinochlore are present in small concentrations.

In case 17 (D_e is 10 times larger than in the full reference case) ~40 % of the montmorillonite mass in the backfill is dissolved after 100 000 years (Figure 7-13). Not only montmorillonite dissolution is larger, but also concrete degradation is accelerated. In the concrete structure, ettringite has dissolved in favour of straetlingite in the first 0.35 m from the concrete–bentonite interface, while CSH1.6 is replaced by CSH1.2 in the entire thickness of the cementitious domains (not shown). The chemical description of the alteration in the bentonite backfill is equivalent to that of the reference case, but with increased travel distances of the dissolution and precipitation fronts: 0.65 m of montmorillonite have been entirely dissolved, in contrast to 0.25 m in the reference case.

7.5 Effect of concrete composition

7.5.1 Alkali-leached concrete (#18)

The initial concrete porewater is modified in this case to represent an alkali-leached concrete. Solute concentration in equilibrium with portlandite is imposed, as it is the main mineral buffering the pH after alkalis are leached out. The initial porewater composition is extracted from the reference case results at the time alkalis are leached, leading to a pH value of 12.8 (equivalent to the boundary condition used in the simplified analysis, Table 7-1). As expected, assuming a lower initial alkalinity of the cementitious system results in a higher degradation of the cementitious domains (due to the reduced buffering capacity) and a reduced depletion of montmorillonite from the backfill.

Overall, the degradation of the montmorillonite mass in the bentonite backfill is reduced from 30 % in the full reference case to ~25 % after 100 000 years (Figure 7-13). Differences compared to the reference case are due to a much faster dissolution of montmorillonite during the first thousands of years in the reference case. However, after alkalis are leached in the reference case, the rate of montmorillonite dissolution is similar in both cases (the slope of the curves in Figure 7-13 is approximately the same after 20 000 years). In case 18, portlandite is almost fully dissolved in the concrete structure, while only a slight decrease (0.1 m) of high Ca/Si ratio C-S-H gel is observed (Figure C-2 in Appendix C). In the bentonite backfill, the main difference is a sharper montmorillonite dissolution front (steeper concentration gradient) in case 18 (Figure C-2) compared to the reference case (Figure 7-7). Given that the dissolution depth is the same, the sharper front is an indication of less degradation than in the reference case.

Table 7-1. Concrete porewaters used in the reference case in the simplified analysis (boundary condition: porewater in equilibrium with portlandite), the reference case in the full analysis (initial porewater), and case 18 (alkali leached: initial porewater in equilibrium with portlandite).

	Reference case in simplified analysis	Reference case in full analysis	Case 18 (alkali leached)
pH	12.83	13.61	12.85
Temperature (°C)	15	15	15
Solutes (totals)	**Concentration (M)**		
Al	5.54×10^{-7}	2.08×10^{-4}	3.48×10^{-5}
C	1.00×10^{-5}	6.81×10^{-7}	6.53×10^{-8}
Ca	2.43×10^{-2}	1.61×10^{-3}	2.64×10^{-2}
Cl	5.55×10^{-5}	1.00×10^{-10}	7.71×10^{-2}
K	7.60×10^{-5}	2.26×10^{-1}	5.32×10^{-2}
Mg	2.53×10^{-8}	3.68×10^{-10}	2.51×10^{-9}
Na	4.79×10^{-3}	4.01×10^{-2}	1.90×10^{-2}
S (6)	3.29×10^{-3}	1.56×10^{-4}	4.17×10^{-6}
Si	4.52×10^{-5}	2.91×10^{-5}	2.57×10^{-6}

7.5.2 Influence of the waste domain (#19)

This case studies the impact of assuming that the waste domain does not contribute to the alkalinity of the system. The case considers a closed boundary at the concrete-waste interface, excluding the waste domain from the simulation. This assumption substantially limits the mass of concrete in the system (the total concrete mass in the waste domain is 2.26 times higher than in the concrete structure, see Section 4).

In this scenario, portlandite is almost completely degraded after 90 000 years. In terms of montmorillonite degradation, ~25 % of the initial mass of montmorillonite is dissolved after 100 000 years. The absence of the contribution from the waste domain results in complete depletion of portlandite in the concrete structure, in contrast to the reference case. After 100 000 years, CSH1.6 is replaced by CSH1.2 in 20 cm of the concrete structure. Moreover, sodium saponite precipitates instead of potassium saponite in the reference case (Figure C-3 in Appendix C).

7.6 Effect of bentonite backfill composition

7.6.1 Effect of cation exchange (#20)

One of the main changes between the simplified and full analysis is the cation exchange in the bentonite interlayer water. In the full analysis model presented in Section 4, a sodium-dominated interlayer is described and cation exchange reactions with sodium, calcium, magnesium and potassium are included. On the other hand, the simplified analysis presented in Section 6 considers a calcium-dominated bentonite interlayer, assuming that cation exchange reactions are much faster than montmorillonite dissolution and considering these as uncoupled processes. Case 20 assesses the implications of this simplification by excluding cation exchange reactions and considering a Ca-dominated montmorillonite.

The results indicate that the mass of montmorillonite dissolved after 100 000 years is very similar to the reference case (Figure 7-13). A slower degradation is observed during the first 25 000 years. This is related to a reduced degradation of the concrete structure due to an increase in C-S-H gel precipitation (favoured by the calcium-dominated bentonite). Small differences are found on the bentonite side, where the montmorillonite dissolution front is almost identical to the reference case after 100 000 years. The greater amount of calcium is reflected in a greater precipitation of calcium heulandite at the expense of sodium phillipsite (Figure C-4 in Appendix C). Near the concrete–bentonite interface, lower maximum concentrations of clinochlore and calcite precipitate compared to the reference case.

7.6.2 Effect of zeolites (#21)

To further study the role of secondary minerals, this case considers a simulation with a different group of zeolites proposed by Soler (2013). The phillipsite and heulandite mineral phases considered in the reference case have been replaced by mordenite, stilbite, natrolite and gismondine. The main motivation of this simulation case is that the zeolites considered in the reference case have an impact on the bentonite system even without any external perturbation. This is due to the fact that precipitation kinetics are not considered in this work given the lack of reliable data. As a result, the bentonite porewater is initially supersaturated with respect to some of the zeolites considered as secondary phases in the reference case, even though these phases are only expected to form under highly alkaline conditions. This supersaturation drives a fast dissolution of albite (an accessory mineral in bentonite, see Table 4-3) and a much slower partial dissolution of montmorillonite, even in the bentonite backfill analysed as a closed system (6 % after 100 000 years, results not shown). On the other hand, the use of zeolites proposed by Soler (2013) leads to a stable bentonite composition, with much slower changes, even in the long term.

Appendix D shows the number of moles of OH^- needed to dissolve 1 mol of montmorillonite and the corresponding moles of zeolite precipitating. To this end, it is assumed that the limiting factor is the aluminium released by montmorillonite (1.66 moles of Al^{3+}, see Equation 4-1 or 8-2). The results of considering different zeolites are based on the stoichiometry in ThermoChimie v9b and the assumed speciation of Al and Si corresponding to alkaline conditions (pH > 10). These values should be considered as indicative only, since a sequence of minerals is expected to form, and not just one. Moreover, in an open system such as the one studied here, transport processes also need to be considered. The results in Appendix D are thus not representative of the overall hydroxyl mass balance but give an idea of the relative contribution to pH of different zeolites precipitating.

The results of case 21 indicate that after 100 000 years, 25 % of the initial mass of montmorillonite has dissolved, i.e. 5 % less than in the reference case (Figure 7-13). Also, the decrease in the dissolution rate of montmorillonite in the long term is remarkable compared to the reference case, as observed in Figure 7-13. Figure C-5 in Appendix C shows the mineralogical profiles after 100 000 years. Near the concrete–bentonite interface, secondary minerals precipitate in higher concentrations, in this case mainly analcime. Next to the rock-bentonite interface, almost no chemical alteration is observed in the bentonite, as opposed to the reference case (see discussion in paragraph above). On the concrete side, chemical alteration is more advanced in the concrete structure, with a C-S-H degradation sequence that shows less 1.6 Ca/Si gel left, a larger concentration of 1.2 Ca/Si gel and precipitation of some 0.8 Ca/Si gel near the concrete–bentonite interface. In this case, no saponite and almost no calcite is observed, as opposed to the reference case, mainly due to the concentration increase of minerals precipitating in the bentonite backfill.

In the bentonite backfill, an increase of calcium clinoptilolite precipitation is observed in the mid part of the domain, and also the occurrence of stilbite (one of the alternative zeolites considered in this case). The montmorillonite dissolution front is less sharp in this zone, although the complete dissolution depth is similar to the reference case. Phillipsite precipitation is now replaced by analcime, while lower calcite and chlorite concentrations are found close to the concrete–bentonite interface. Some primary minerals as albite and quartz are less dissolved than in the reference case. The results are again in agreement with the alteration sequence proposed by Savage et al. (2007) and shown in Figure 4-3.

7.7 Summary of results

Figure 7-13 presents the evolution in time of the normalized mass of montmorillonite in the bentonite backfill. After 100 000 years, 30 % has been dissolved in the reference case. The most important parameters controlling montmorillonite dissolution have been revealed to be: the montmorillonite reactive surface area (case 15), the effective diffusion coefficient of solutes in the concrete structure, the inclusion or not of secondary minerals in the bentonite backfill, and the consideration or not of the concrete present in the waste domain. The most aggressive scenario (case 17) is obtained when the diffusion coefficient of solutes in the concrete structure is increased by one order of magnitude (40 % of the montmorillonite is dissolved). If this coefficient is reduced by a factor of 3.5 (case 16) from the reference case value, degradation is reduced to 22 % of the initial montmorillonite mass. Not accounting for secondary mineral precipitation in the bentonite (case 13) leads to a non-conservative scenario, where only 6.5 % has dissolved. If small changes in the set of secondary minerals are considered (case 21), the final degradation is only 5 % less than in the reference case. Another non-conservative assumption is to exclude the waste domain from the model and replace it by a closed boundary condition (case 19). This results in the dissolution of 25 % of the initial montmorillonite mass. In turn, the impact of including (or not) cation exchange reactions is small in terms of montmorillonite dissolution. Finally, assuming a concrete composition with initially leached alkalis (case 18) results in 5 % less dissolved montmorillonite compared to the reference case.

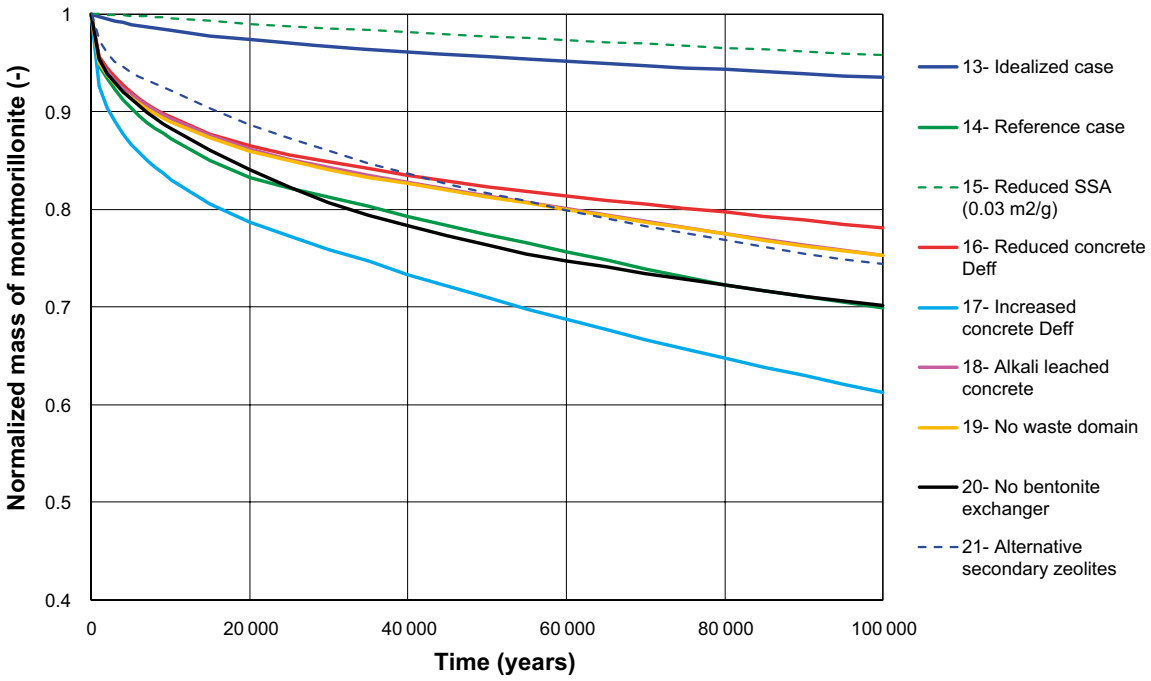

Figure 7-13. *Normalized mass or mass fraction of montmorillonite (remaining mass divided by initial mass) in the bentonite backfill as a function of time (years). Comparison between integrated mass of bentonite at each time step for all simulated cases.*

8 Analytical estimations of montmorillonite dissolution depth

In this section, a simple analytical solution is used to calculate the evolution of the montmorillonite dissolution depth as a function of time. Two analytical models are presented, one for a fixed (concrete water composition) boundary condition based on Levenspiel (1972) in Section 8.1, and one that also includes concrete degradation based on Neretnieks (2014) in Section 8.2.

8.1 "Only bentonite backfill" case

First, the shrinking core model (SCM) with parameters corresponding to a slab geometry is used (Levenspiel 1972). This model, applied to the bentonite backfill, considers diffusion-driven transport and dissolution of a mineral phase under thermodynamic equilibrium conditions. The dissolution depth is simply expressed as:

$$h_{mmt} = \sqrt{2\frac{D_e \cdot C_{BC}^{OH^-} \cdot t}{m_0^{OH^-}}} \quad (8\text{-}1)$$

where h_{mmt} (m) is the depth of complete montmorillonite dissolution (the analytical model assumes a drop of solid concentration from the initial value to zero in an infinitely narrow distance), D_e (m^2/s) is the effective diffusion coefficient (constant in this model, in agreement with the reactive transport simulations). $C^{OH^-}{}_{BC}$ and $m^{OH^-}{}_0$ are the concentration of OH^- ions at the boundary and the total amount of OH^- ions needed to dissolve the initial amount of montmorillonite at a given point in the backfill, respectively. For a pH value at the boundary of 12.83 (Table 6-1), the corresponding $C^{OH^-}{}_{BC}$ is 6.84×10^{-2} M. The value of $m^{OH^-}{}_0$ is calculated from the multiplication of the initial amount of montmorillonite in the backfill (3.573 $mol \cdot l_{medium}^{-1}$, Table 4-3) by the number of moles of OH^- ions that are needed to dissolve 1 mol of montmorillonite. The latter is equal to 4.64 moles OH/mol montmorillonite, as calculated from the ThermoChimie 9b database used in the reactive transport simulations following the reaction path described in Savage and Benbow (2007) and Gaucher and Blanc (2006):

$$Ca_{0.17}Mg_{0.34}Al_{1.66}Si_4O_{10}(OH)_2 + 2H_2O + 4.64OH^- \leftrightarrow 0.17Ca^{2+} + 0.34Mg^{2+} + 1.66Al(OH)_4^- + 4HSiO_3^- \quad (8\text{-}2)$$

This reaction assumes that no other reactions occur that can consume or generate OH^- ions (i.e. the dissolution or precipitation of other minerals in bentonite is not considered) and also that no dilution of OH^- in groundwater occurs. It follows from Equation (8-1) that the dissolution depth is linearly dependent on the square root of time, which is a characteristic feature of diffusion-driven processes. No secondary minerals are considered in this simple model.

Figure 8-1 presents the evolution of the montmorillonite dissolution front as a function of the square root of time. Results obtained from the SCM model and the 1D reactive transport model (for the simplified analysis cases 1-3) are shown. By definition, the SCM results show a linear relation between dissolution depth and the square root of time. The results obtained from 1D modelling also present an almost linear relation, except during the first few thousands of years. Comparison of the SCM (with a pH of 12.83) with the reference case results shows a surprisingly good agreement. For comparison, the sensitivity of the SCM prediction to small changes in pH are also presented as upper (pH = 13.0) and lower (pH = 12.6) thresholds. The slope of the SCM solution (for pH = 12.83) is higher compared to the reference case, which indicates that the dissolution front in the reactive transport model is slowed down by some process not accounted for in the analytical solution. This process is not the kinetics rate of montmorillonite dissolution, as this is shown to be irrelevant (Section 6.7). It is also not related to the effect of secondary minerals or other primary minerals (case 1 in Figure 8-1).

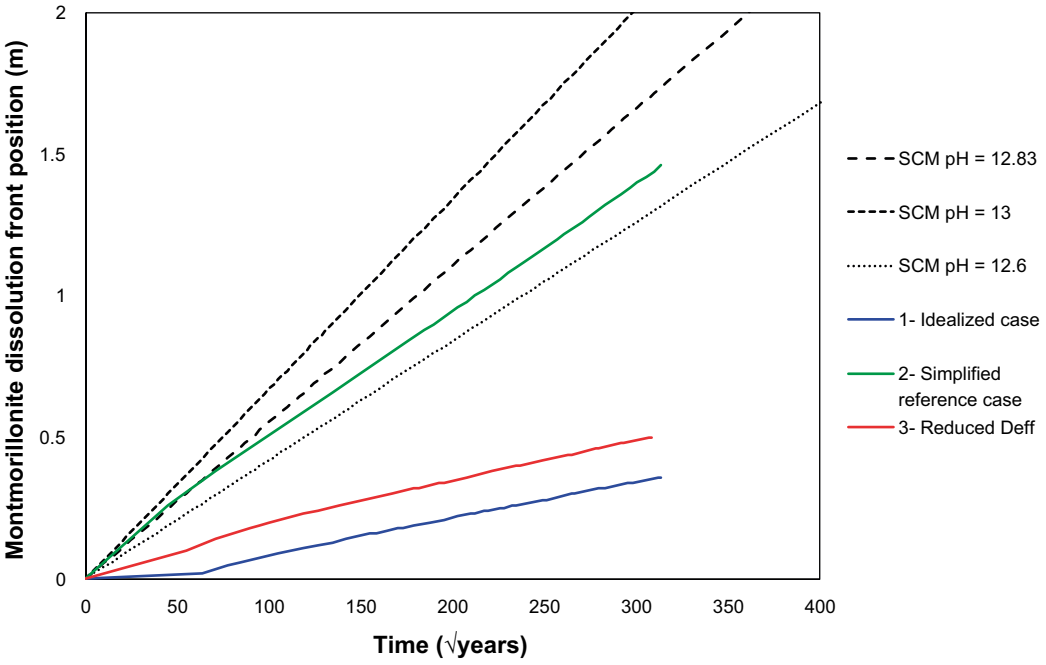

Figure 8-1. *Evolution of the dissolution front calculated using the shrinking core model (SCM) for different pH values and obtained from the 1D reactive transport model (defined in this case as the distance at which the montmorillonite concentration is half of its initial value) for simplified analysis cases 1, 2 and 3, plotted against the square root of time (years$^{1/2}$).*

8.2 Concrete–Bentonite interaction

The shrinking core model (SCM) can also be used to model the interaction between concrete and bentonite (i.e. including concrete degradation), as recently proposed by Neretnieks (2014). The two media are represented by a single mineral: on the concrete side portlandite dissolution leads to OH^- generation and subsequent diffusion to the interface, while on the bentonite side, OH^- ions react with montmorillonite at thermodynamic equilibrium. The main assumptions, as in the model described in Section 8.1, are that (1) concentrations of minerals forming/dissolving are much higher than the dissolved solute concentration in the porewater and (2) reactions are sufficiently fast so that equilibrium is maintained. This justifies a pseudo steady-state approximation and the use of the shrinking core model.

The model presented in Neretnieks (2014) can be used to calculate dissolution depths in portlandite (concrete, subscript 1) and montmorillonite (bentonite, subscript 2) as a function of time. These dissolution depths, represented in Figure 8-2, can be calculated using three simple algebraic equations:

$$x_1 = \sqrt{\frac{2D_1(c_1 - c_i)t}{q_1 f_1}} \tag{8-3}$$

$$x_2 = -x_1 \frac{q_1 f_1}{q_2 f_2} \tag{8-4}$$

$$c_i = \frac{D_2 c_2 + D_1 c_1 \cdot \frac{q_1 f_1}{q_2 f_2}}{D_2 + D_1 \cdot \frac{q_1 f_1}{q_2 f_2}} \tag{8-5}$$

where x_1 and x_2 are the dissolution depths in portlandite and smectite/montmorillonite (in meters), respectively, c_1 and c_2 are the hydroxyl concentrations in the unaffected domains (mol/m^3), q_1 and q_2 are the initial concentrations of dissolving minerals (mol/m^3), f_1 and f_2 are the stoichiometric factors releasing/reacting OH^- per mole of mineral ($mol_{OH}/mol_{mineral}$), and D_1 and D_2 (m^2/s) are the unaltered effective diffusion coefficient of the concrete and bentonite domains, respectively. Finally, c_i (mol/m^3) represents the OH^- concentration at the interface (Figure 8-2), assumed constant over time.

The dissolution depth is again linearly dependent on the square root of time, as any diffusion-driven process. This simple model assumes constant values for all entities presented in Equation 8-3 to 8-5. Acknowledging these simplifications, the model is used to represent the reference case scenario including cementitious and bentonite domains with the properties given in Table 8-1. The hydroxyl concentrations correspond to pH values of 12.8 in concrete and 8 in bentonite. With these values, the concentration of hydroxyl at the interface, c_i, is equal to 0.304 mol/m^3, corresponding to a pH of ~10.5. This fixed value can be compared to the pH at the interface of the reactive transport models, see e.g. Figure 7-4. In this figure, the pH at both sides of the concrete–bentonite interface approaches a value of 10.5–10.8 after 30 000 to 40 000 years. However, the pH is not constant with time, especially during the first 30 000 years. The stoichiometric factor f_2 is set to a value of 4.64 in accordance to Equation 8-2 that follows the reaction path described in Savage and Benbow (2007). This is equivalent to assume that no secondary minerals are formed, and no accessory minerals are dissolved when exposed to an alkaline plume. This is of course a simplification and it is acknowledged that it is not a realistic assumption. Still, it can be used as a first approximation. However, it is noted that Neretnieks (2014) proposed a factor of 2, as derived from the reaction:

$$Al_2Si_4O_{10}(OH)_2(s) + Ca(OH)_2(s) \rightarrow CaAl_2Si_4O_{12}(s) + 2H_2O \qquad (8\text{-}6)$$

In Equation 8-6, it is implicitly assumed that a zeolite is formed in the process, in this case laumontite (as previously used in reactive transport modelling by e.g. Savage et al. 2002). This equation assesses smectite dissolution and interaction with portlandite through its alumino-silicate "cells" to form laumontite. It is then assumed by Neretnieks (2014) that f_2 will take a value of around 2 irrespective of the smectite composition. Another analytical estimation of the dissolution depth has been performed based on this assumption, results of which are presented in Figure 9-1. Appendix D presents the OH^- mass balance under alkaline conditions when precipitating different zeolites at the expense of the dissolution of 1 mol of montmorillonite. It may be observed that very different results can be obtained depending on the zeolite formed, ranging from net consumption of OH^- to net release of OH^- ions.

Table 8-1. Concrete and bentonite properties corresponding to the reference case simulation.

Parameter	Concrete (1)	Bentonite (2)
D_i (m^2/s)	3.5×10^{-12}	1.2×10^{-10}
f_i (mol/mol)	2.0	4.64
c_i (mol/m^3)	63.09	0.01
q_i (mol/m^3)	1 372	3 573

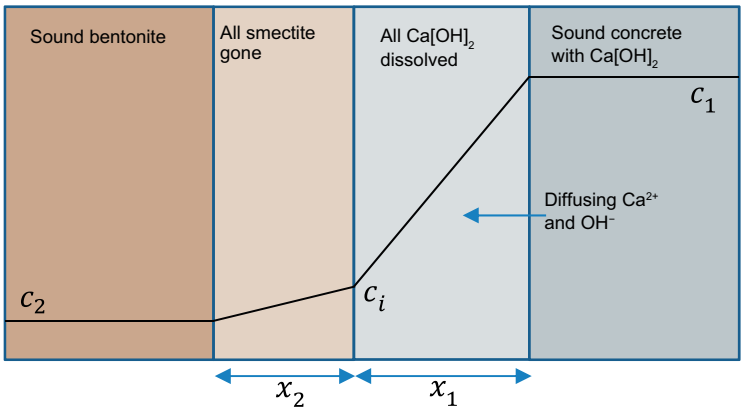

Figure 8-2. *Schematic representation of portlandite and smectite depletion with hydroxyl concentration in each domain (adapted from Neretnieks 2014).*

Concrete and bentonite degradation are presented in Figure 8-3 in terms of portlandite and montmorillonite dissolution depths. Results of the analytical model obtained using the parameter values in Table 8-1 are compared with the 1D reactive transport simulation (full analysis reference case). The analytical model predicts dissolution depths after 100 000 years of 0.71 m and 0.11 m for concrete and bentonite, respectively, while reactive transport modelling indicates depths of 0.55 m and 0.69 m, respectively. The differences between model results are remarkable, since the analytical model predicts one order of magnitude less montmorillonite. In turn, closer values are found for the concrete side, although the analytical model predicts 20 % more concrete degradation. It should be noted that the concentration profiles of the reactive transport model are not piecewise linear with sharp gradients, as in the analytical model, but smooth (Figure 7-5). Therefore, a comparison is not straightforward. The values of dissolution depth, h_{mmt} (m), presented in Figure 8-3 for the reactive transport model are obtained from the integrated mass of montmorillonite in the entire backfill thickness, L (m) as:

$$h_{mmt} = \frac{M_{mmt}(t)}{M_{mmt,0}} \cdot L \qquad (8\text{-}7)$$

where $M_{mmt,0}$ and $M_{mmt}(t)$ are the initial mass of montmorillonite and the remaining mass of montmorillonite at time 't', respectively. A perhaps better approach for comparison is presented in Figure 9-1, where analytical results in terms of dissolved mass of montmorillonite (also from Equation 8-7) instead of dissolution depth are shown.

The sensitivity of the analytical model in terms of montmorillonite dissolution (x_2) for different values of the parameter f_2 (stoichiometric factor releasing/reacting OH^- per mole of mineral ($mol_{OH}/mol_{mineral}$) is shown in Table 8-2.

Table 8-2. Sensitivity of the analytical model to parameter f2.

Time (yr)	f_2	0.5	1	2	3	4	5
	c_i (mol/m^3)	10.8	5.5	2.78	1.86	1.40	1.12
	pH_i	12.03	11.74	11.44	11.27	11.15	11.05
	x_1 (m)	x_2 (m)					
1 000	0.141	0.217	0.109	0.054	0.036	0.027	0.022
10 000	0.447	0.687	0.343	0.172	0.114	0.086	0.069
100 000	1.414	2.171	1.086	0.543	0.362	0.271	0.217

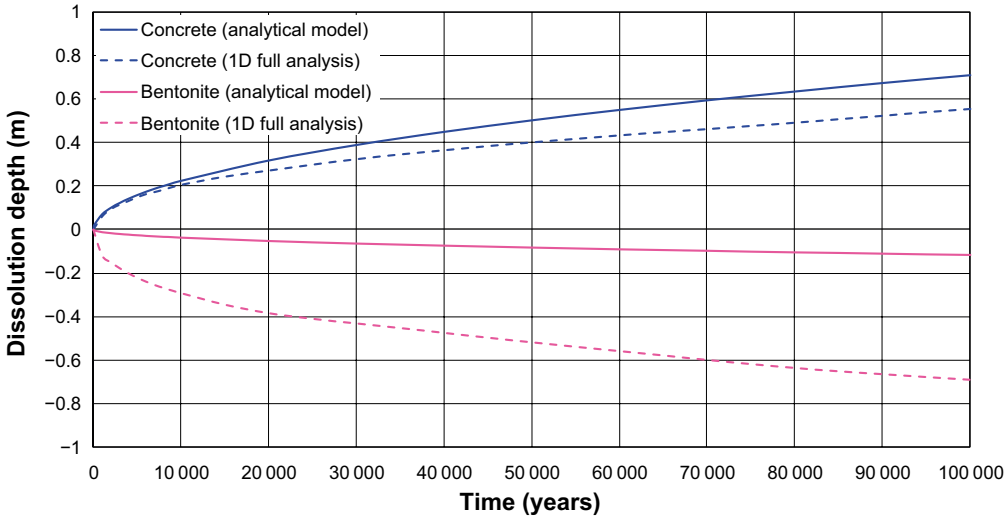

Figure 8-3. *Dissolution depth result for concrete and bentonite domains, comparison between analytical model and reactive transport full analysis reference case (case 14) (defined in the latter case as the distance at which the montmorillonite concentration is half of its initial value).*

An important outcome of these results is that the montmorillonite dissolution depth is inversely proportional to f_2. The higher the number of moles of OH needed to dissolve 1 mol of montmorillonite, the lower the dissolution depth, with a factor that is $f_{2,ref}/f_2$ ($f_{2,ref} = 2$ in this case). Thus, to obtain a dissolution depth of 0.92 m, as in the full reference case, f_2 should be equal to 1.18. The factor f_2 is in fact not corresponding to a single reaction (as for example shown in Appendix D for different zeolites) but should be regarded as a value gathering the overall contribution of the whole sequence of mineral alteration.

The fact that the dissolution depth is inversely proportional to f_2 can be derived from Equations 8-3 to 8-5 assuming the following inequalities:

- $D_1 \cdot q_1 \cdot f_1 \cdot c_1 \gg D_2 \cdot q_2 \cdot f_2 \cdot c_2$
- $D_2 \cdot q_2 \cdot f_2 \gg D_1 \cdot q_1 \cdot f_1$

These inequalities are fulfilled when using the data of Table 8-1. With these assumptions, and plugging Equations 8-3 and 8-5 into Equation 8-4, the montmorillonite dissolution depth is calculated as:

$$x_2 = \frac{(q_1 \cdot f_1)^{\frac{1}{2}}}{q_2 \cdot f_2} \sqrt{2D_1 \cdot c_1 \cdot t} \qquad (8\text{-}8)$$

It may be observed that x_2 is inversely proportional to f_2 and also that it depends of the square root of f_1, which is the moles of OH^- per mol of dissolved portlandite. This result is also important, since concrete degradation cannot be oversimplified to the dissolution of portlandite. Höglund (2014) additionally considered the coupling with the dissolution of C-S-H in a similar analytical equation. Moreover, and perhaps more importantly, secondary minerals also form in concrete as a result of the interaction with bentonite, as shown in Section 7. Thus, for estimation of the factor f_1 a similar approach as used for bentonite should be considered. Still, the fact that x_2 depends on the square root of f_1 indicates a lower impact of the uncertainty in f_1 on montmorillonite dissolution compared to f_2.

It may be concluded from this study that although the analytical model proposed by Neretnieks (2014) is appealing due to its simplicity, additional knowledge of the geochemistry and mineralogical alteration of the concrete–bentonite system is needed to parametrize the model. In this respect, reactive transport modelling appears as the best available tool to explicitly include all the geochemical complexity of the system to make predictions. Of course, reactive transport is very demanding in terms of cpu time, while the analytical equation can be readily solved in a spreadsheet. It should be possible to extract meaningful parameters for the analytical model from a reactive transport calculation, as done above for f_2, but this needs a more in depth understanding of the mineralogical alteration and the overall mass balance of OH^- and is outside the scope of this study.

Other issues with the analytical model of Neretnieks (2014) are related to the potential spatial variations in the diffusion coefficient of solutes in each material and the kinetic nature of montmorillonite dissolution if for example a low reactive surface area is considered.

9 Discussion and conclusions

Two sets of 1D reactive transport models were implemented in iCP to simulate the degradation of the bentonite backfill in the BHA vault of the proposed repository concept for legacy waste, named SFL. The main component of the engineered barrier system of this vault is a bentonite backfill that surrounds a concrete structure that contains the waste. The backfill is assumed here to be composed of MX-80 bentonite (e.g. SKB 2011), which contains a large fraction of montmorillonite. This mineral is the main responsible for the swelling capacity of bentonite and most of its related safety functions. It is well known that montmorillonite in contact with high-pH solutions gradually dissolves with time (Cama et al. 2000, Gaucher and Blanc 2006).

The focus of this study was on the evaluation of montmorillonite dissolution in the barrier as a result of interaction with cementitious materials over a time span of 100 000 years. Kinetic dissolution of montmorillonite following the rate law proposed by Sato et al. (2004) and Oda et al. (2014) was considered in the simulations. This kinetic rate depends both on pH and temperature. At repository conditions (15 ºC), the rate law predicts a small increase in the rate even for large changes in pH (from 8 to 13), which is in agreement with experimental data.

Two types of analysis are presented: (1) a simplified analysis where the cementitious source is modelled as a constant boundary condition; and (2) a full analysis where bentonite and concrete degradation are coupled, explicitly considering the cementitious domains (waste domain and concrete structure). A sensitivity case studied the impact of not considering the contribution of the waste domain (case 19), only the contribution of the concrete structure. The reactive transport code iCP (interface between Comsol Multiphysics and Phreeqc, Nardi et al. 2014) is used in the modelling work, as well as PHAST (Parkhurst et al. 2010).

For each analysis, an idealized case, where only montmorillonite is considered in the bentonite backfill was studied first. This case may be regarded as an academic exercise, which aim is to gain system understanding, and for comparison with more realistic setups.

A reference case was proposed for each analysis (simplified and full) considering repository conditions and what is thought to be a plausible scenario in terms of processes. In addition, and given the relatively high degree of uncertainty related to several of the model parameters and variables, a set of sensitivity cases for each analysis was proposed (Table 3-1 and Table 3-2). The parameters analysed were the effective diffusion coefficient of solutes in the bentonite and concrete barriers, the reactive montmorillonite surface area, the set of primary and secondary minerals, the concrete porewater composition, bentonite chemical description, and the boundary conditions at the concrete–bentonite and rock-bentonite interfaces.

The results of the full analysis reference case predict a dissolution of montmorillonite after 100 000 years of 30 % of the initial mass in the backfill (Figure 9-1). Although montmorillonite full depletion is predicted over only 0.25 m after 100 000 years, the entire backfill is partially affected (Figure 7-5). As expected, the results of the reference case from the simplified analysis indicate a much higher dissolution of montmorillonite (77 % of the initial mass). This is due to the fact that in the simplified case the pH at the interface is much higher than in the full case, and also that the low solute diffusivity in the concrete structure is not considered. In the simplified reference case, the montmorillonite dissolution depth reaches a depth of 1.5 m and only 23 % of the initial montmorillonite remains in the barrier after the studied period (Figure 9-1). A first conclusion is that including the concrete barriers explicitly in the analysis leads to a much more realistic representation of the system. The simplified analysis, on the other hand, can be regarded as giving an over-conservative estimate of the degradation.

The main issues identified from the sensitivity analysis are:

(1) Decreasing the reactive surface area of montmorillonite from 800 to 30 $m^2 \cdot g^{-1}$ does not significantly impact the conclusions of the study, neither considering montmorillonite in thermodynamic equilibrium. These results indicate that the degradation process, at least in the simplified analysis, is dominated by diffusion rather than by kinetics of reaction. However, the results are much more sensitive to reactive surface areas in the range 0–30 m^2/g. When the correlation derived by Terada et al. (2019) is used, a value of 0.03 $m^2 \cdot g^{-1}$ is obtained, and the montmorillonite dissolution process is drastically reduced. In fact, in the full analysis case (Section 7), the mass of remaining montmorillonite is larger than the idealized case (case 13).

(2) The impact of the effective diffusion coefficient of solutes in concrete and especially in bentonite is very high under water-saturated conditions and is shown to be one of the most important parameters studied here.

(3) The effect of including the concrete barrier and its alteration at the concrete–bentonite interface is also very important, leading to a much more realistic representation.

(4) Finally, the set of secondary minerals considered in the models has a relatively high impact on the dissolution depth (Figure 9-1): the higher the mass of secondary minerals precipitated, the higher the mass of dissolved montmorillonite, at least when considering a rate expression that includes the proximity-to-equilibrium term (Equation 4-4) or when considering thermodynamic equilibrium.

Not considering the influence of the concrete mass within the waste domain leads to a reduction of the mass of dissolved montmorillonite. Only ~25 % of the initial montmorillonite is dissolved after 100 000 years. In the same way, omitting the initial alkalis present in concrete has a similar effect, the reduction in total dissolution is equivalent (from 30 % of the initial mass in the full reference case to ~25 %). However, these cases are not conservative and may not be realistic given that the present design of the vault considers a bentonite backfill entirely surrounding the cementitious materials. Under these conditions, any initial alkalinity inside the backfill will need to diffuse through bentonite to be dissipated. Including cation exchange reactions in the bentonite interlayer does not impact total degradation results, which is to be expected since cation exchange and montmorillonite dissolution take place at different time scales.

Analytical models were also applied to the studied system to predict the dissolution depth of montmorillonite (Section 8). The shrinking core model (Levenspiel 1972) was used first for the bentonite backfill assuming the concrete domain as a constant boundary condition, as in the simplified analysis. The analytical model considers a diffusion-dominated system, where dissolution occurs instantaneously following a pseudo-steady state evolution of the dissolution depth. The results compare qualitatively well with the corresponding reactive transport models (Section 8.1). A second analytical model that also considers the concrete side of the interface, as proposed by Neretnieks (2014) was also used to predict the dissolution of montmorillonite (Section 8.2). The main difference with the preceding model is that the pH at the interface not only depends on the concrete composition but also on its transport properties. Naturally, the pH at the interface is much lower in this later model (10.5 instead of 12.8 in the only backfill analytical model, Section 8.1). In this case, the comparison with the corresponding reactive transport models (including concrete–bentonite interaction) shows a good agreement if the idealized case is considered. However, analytical models are shown to significantly underestimate montmorillonite dissolution when compared to a full reactive transport simulation (Figure 9-1).

In summary, montmorillonite dissolution in the BHA vault is governed in the present study by:

1. The reactive surface area of montmorillonite if its value is below 30 m^2/g.
2. How the concrete–bentonite interface is treated (boundary condition or explicitly modelled as a porous media).
3. The diffusion coefficient of solutes in the bentonite barrier and the concrete structure.
4. The set of secondary minerals that are allowed to precipitate in the models.
5. The alkali content in the cementitious domains.

It is noted that these conclusions are obtained using two different approaches to the problem. Bentonite and concrete degradation have proved to be highly coupled processes. Thus, representing the cementitious source as a constant concentration boundary condition (Dirichlet) is both unrealistic and over-conservative.

The limitations of the models presented in this report should be recalled here. First, it is assumed that the physical properties of the barriers are not coupled to their chemical alteration. In other words, porosities and diffusion coefficients do not depend on mineral volume changes or changes in the microstructure. A more realistic model could be obtained by including these couplings. However, it is expected that changes in porosity and solute diffusivity will also be very much affected by the mechanical response near the interface. On the bentonite side, significant changes in terms of swelling pressure and porosity are expected. On the concrete side, mechanical couplings are expected to be less important, except in the cases where significant sulphate-bearing phases form in the cementitious matrix (ettringite, gypsum). In that case, cracking due to expansive reactions could lead to an increase in solute diffusivity (diffusion coefficient).

Another limitation of the analytical models is the required estimate of the moles of OH^- ions needed to dissolve one mol of montmorillonite. This parameter depends to a large extent on the mineral degradation sequence in the bentonite backfill. Sensitivity of the results to changes in this parameter is shown to be significant (values of 2, as used by Neretnieks (2014), and 4.64 are tested here). In principle, it should be possible to determine this value from reactive transport simulations, although it is not straigthforward. Future efforts could be aimed at combining the benefits of both the analytical and the geochemical (i.e. without transport) models.

A final remark is on the treatment of the precipitation of secondary minerals. Given the lack of reliable kinetic data for precipitation reactions (see e.g. Soler et al. 2014), thermodynamic equilibrium is considered in this work for secondary mineral formation. This may have implications on the results, especially when introducing zeolites that are only expected to form under highly alkaline conditions (Section 7.6.2). In principle, assuming thermodynamic equilibrium is a conservative choice due to the fact that it favours montmorillonite dissolution by maintaining the pore solution undersaturated with respect to this mineral.

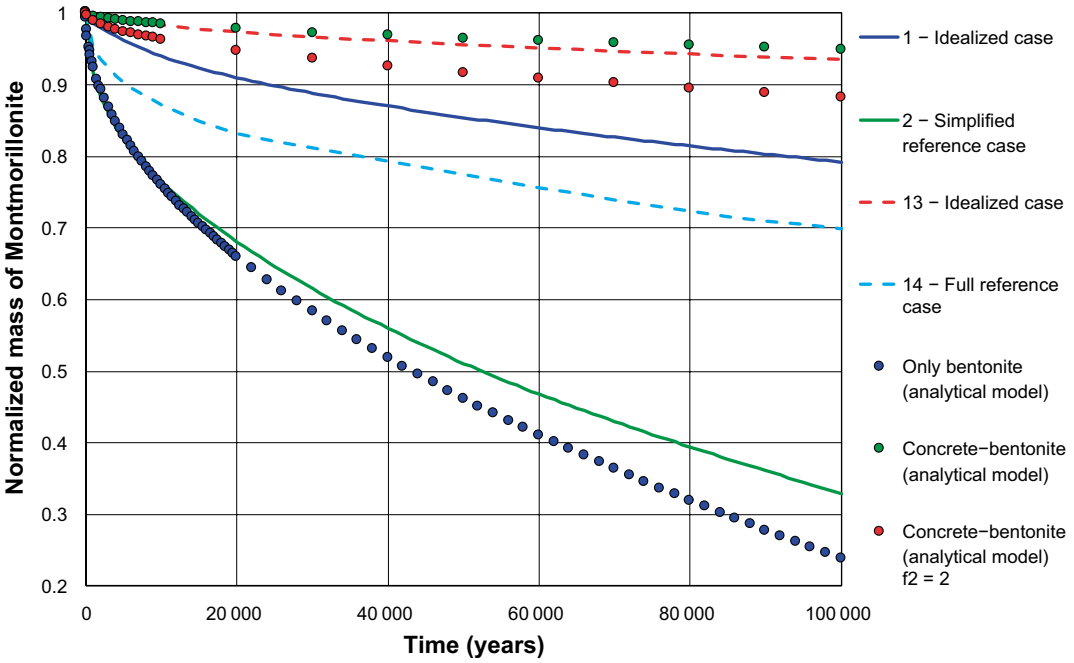

Figure 9-1. *Normalized mass or mass fraction of montmorillonite (remaining mass divided by initial mass) in the bentonite backfill as a function of time (years). Comparison between integrated mass of montmorillonite at each time step for simplified, full and analytical models.*

References

SKB's (Svensk Kärnbränslehantering AB) publications can be found at www.skb.com/publications. SKBdoc documents will be submitted upon request to document@skb.se.

Bergaya F, 1995. The meaning of surface area and porosity measurements of clays and pillared clays. Journal of Porous Materials 2, 91–96.

Bickmore B R, Bosbach D, Hochella M F, Charlet L, Rufe E, 2001. In situ atomic force microscopy study of hectorite and nontronite dissolution: Implications for phyllosilicate edge surface structures and dissolution mechanisms. American Mineralogist 86, 411–423.

Bildstein O, Claret F, 2015. Stability of clay barriers under chemical perturbations. In Tournassat C, Steefel C I, Bourg I C, Bergaya F (eds). Natural and engineered clay barriers. Amsterdam: Elsevier. (Developments in Clay Science 6), 155–188.

Bosbach D, Charlet L, Bickmore B, Hochella M F, 2000. The dissolution of hectorite: In situ, real-time observations using atomic force microscopy. American Mineralogist 85, 1209–1216.

Bradbury M H, Baeyens B, 2002. Porewater chemistry in compacted re-saturated MX-80 bentonite: physicochemical characterisation and geochemical modelling. PSI Bericht 02-10, Paul Scherrer Institut, Switzerland, Nagra NTB 01-08, Nagra, Switzerland.

Bradbury M H, Baeyens B, 2011. Physico-chemical characterisation data and sorption measurements of Cs, Ni, Eu, Th, U, Cl, I and Se on MX-80 bentonite. PSI Bericht 11-05, Paul Scherrer Institute, Switzerland.

Cama J, Ayora C, 1998. Modelling the dissolution behaviour of a clayey barrier. Mineralogical Magazine 62A, 271–272.

Cama J, Ganor J, 2015. Dissolution kinetics of clay minerals. In Tournassat C, Steefel C I, Bourg I C, Bergaya F (eds). Natural and engineered clay barriers. Amsterdam: Elsevier. (Developments in Clay Science 6), Chapter 4.

Cama J, Ganor J, Ayora C, Lasaga C A, 2000. Smectite dissolution kinetics at 80 ºC and pH 8.8. Geochimica et Cosmochimica Acta 64, 2701–2712.

Carlson L, 2004. Bentonite mineralogy. Part 1: Methods of investigation – a literature review. Part 2: mineralogical research of selected bentonites. Posiva Working Report 2004-02, Posiva Oy, Finland.

COMSOL, 2015. COMSOL Multiphysics® v. 5.2. COMSOL AB, Sweden.

Cronstrand P, 2016. Long-term performance of the bentonite barrier in the SFR silo. SKB TR-15-08, Svensk Kärnbränslehantering AB.

De Windt L, Pellegrini D, van der Lee J, 2004. Coupled modeling of cement/ claystone interactions and radionuclides migration. Journal of Contaminant Hydrology 68, 165–182.

De Windt L, Marsal F, Tinseau E, Pellegrini D, 2008. Reactive transport modeling of geochemical interactions at a concrete/argillite interface, Tournemire site (France). Physics and Chemistry of the Earth, Parts A/B/C 33, S295–S305.

Elfwing M, Evins L Z, Gontier M, Grahm P, Mårtensson P, Tunbrant S, 2013. SFL concept study. Main report. SKB TR-13-14, Svensk Kärnbränslehantering AB.

Fernández R, Mäder U K, Rodriguez M, Vigil de la Villa R, Cuevas J, 2009. Alteration of compacted bentonite by diffusion of highly alkaline solutions. European Journal of Mineralogy 21, 725–735.

Fernández R, Cuevas J, Mäder U K, 2010. Modeling experimental results of diffusion of alkaline solutions through a compacted bentonite barrier. Cement and Concrete Research 40, 1255–1264.

Gaucher E, Blanc P, 2006. Cement/clay interactions – a review: experiments, natural analogues, and modeling. Waste Management 26, 776–788.

Gaucher E, Blanc P, Matray J M, Michau N, 2004. Modeling diffusion of an alkaline plume in a clay barrier. Applied Geochemistry 19, 1505–1515.

Gaucher E, Tournassat C, Nowak C, 2005. Modelling the geochemical evolution of the multibarrier system of the Silo of the SFR repository. Final report. SKB R-05-80, Svensk Kärnbränslehantering AB.

Giffaut E, Grivé M, Blanc P, Vieillard P, Colàs E, Gailhanou H, Gaboreau S, Marty N M, Madé B, Duro L, 2014. Andra thermodynamic database for performance assessment: ThermoChimie. Applied Geochemistry 49, 225–236.

Grandia F, Galíndez J-M, Arcos D, Molinero J, 2010. Quantitative modelling of the degradation processes of cement grout. Project CEMMOD. SKB TR-10-25, Svensk Kärnbränslehantering AB.

Höglund L O, 2014. The impact of concrete degradation on the BMA barrier functions. SKB R-13-40, Svensk Kärnbränslehantering AB.

Idiart A, Shafei B, 2019. Modelling of concrete degradation – Hydro-chemical processes. Report for the safety evaluation SE-SFL. SKB R-19-11, Svensk Kärnbränslehantering AB.

Idiart A, Olmeda J, Laviña M, 2019. Modelling of concrete degradation in SFL – influence of concrete mix design. Report for the safety evaluation SE-SFL. SKB R-19-14, Svensk Kärnbränslehantering AB.

Idiart A, Laviña M, Kosakowski G, Cochepin B, Meeussen J C L, Samper J, Mon A, Montoya V, Munier I, Poonoosamy J, Montenegro L, Deissmann G, Rohmen S, Hax Damiani L, Coene E, Naves A (2020). Reactive transport modelling of a low-pH concrete/clay interface. Applied Geochemistry, 104562.

Karnland O, 2010. Chemical and mineralogical characterization of the bentonite buffer for the acceptance control procedure in a KBS-3 repository. SKB TR-10-60, Svensk Kärnbränslehantering AB.

Karnland O, Birgersson M, 2006. Montmorillonite stability. With special respect to KBS-3 conditions. SKB TR-06-11, Svensk Kärnbränslehantering AB.

Karnland O, Olsson S, Nilsson U, 2006. Mineralogy and sealing properties of various bentonites and smectite-rich clay materials. SKB TR-06-30, Svensk Kärnbränslehantering AB.

Kaufhold S, Dohrmann R, Klinkenberg M, Siegesmund S, Ufer K, 2010. N_2-BET specific surface area of bentonites. Journal of Colloid and Interface Science 349, 275–282.

Kiviranta L, Kumpulainen S, 2011. Quality control and characterization of bentonite materials. Posiva Working Report 2011-84, Posiva Oy, Finland.

Knauss K, Wolery T J, 1988. The dissolution kinetics of quartz as a function of pH and time at 70 °C. Physics and Chemistry of the Earth, Parts A/B/C 52, 43–53.

Kosakowski G, Berner U, 2013. The evolution of clay rock/cement interfaces in a cementitious repository for low- and intermediate-level radioactive waste. Physics and Chemistry of the Earth, Parts A/B/C 64, 65–86.

Koskinen K, 2014. Effects of cementitious leachates on the EBS. Posiva 2013-04. Posiva Oy, Finland.

Kuwahara Y, 2006. In situ AFM study of smectite dissolution under alkaline conditions at room temperature. American Mineralogist, 91, 1142–1149.

Köhler S J, Dufaud F, Oelkers E H, 2003. An experimental study of illite dissolution kinetics as a function of pH from 1.4 to 12.4 and temperature from 5 to 50 ºC. Physics and Chemistry of the Earth, Parts A/B/C 67, 3583–3594.

Lehikoinen J, 2009. Bentonite-cement interaction – preliminary results from model calculations. Posiva Working Report 2009-37, Posiva Oy, Finland.

Levenspiel O, 1972. Chemical reaction engineering. 2nd ed. New York: Wiley.

Liu S, Jacques D, Govaerts J, Wang L, 2014. Conceptual model analysis of interaction at a concrete–Boom Clay interface. Physics and Chemistry of the Earth, Parts A/B/C 70–71, 150–159.

Luna M, Arcos D, Duro L, 2006. Effects of grouting, shotcreting and concrete leachates on backfill geochemistry. SKB R-06-107, Svensk Kärnbränslehantering AB.

Marty N M, Tournassat C, Burnol A, Giffaut E, Gaucher E C, 2009. Influence of reaction kinetics and mesh refinement on the numerical modelling of concrete/clay interactions. Journal of Hydrology 364, 58–72.

Marty N M, Cama J, Sato T, Chino D, Villiéras F, Razafitianamaharavo A, Brendlé J, Giffaut E, Soler J M, Gaucher E C, Tournassat C, 2011. Dissolution kinetics of synthetic Na-smectite. An integrated experimental approach. Geochimica et Cosmochimica Acta 75, 5849–5864.

Marty N M, Munier I, Gaucher E, Tournassat C, Gaboreau S, Vong C, Giffaut E, Cochepin B, Claret F, 2014. Simulation of Cement/clay interactions: feedback on the increasing complexity of modelling strategies. Transport in Porous Media 104, 385–405.

Marty N M, Claret F, Lassin A, Tremosa J, Blanc P, Madé B, Giffaut E, Cochepin B, Tournassat C, 2015. A database of dissolution and precipitation rates for clay-rocks minerals. Applied Geochemistry 55, 108–118.

Miller W M, Alexander W R, Chapman N A, McKinley I G, Smellie J T, 2000. Geological disposal of radioactive wastes and natural analogues. Oxford: Pergamon.

Mon A, Samper J, Montenegro L, Naves A, Fernández J, 2017. Long-term non-isothermal reactive transport model of compacted bentonite, concrete and corrosion products in a HLW repository in clay. Journal of Contaminant Hydrology 197, 1–16.

Nakabayashi R, 2014. Evaluation of bentonite/hyperalkaline-fluids interaction in compacted system by X-ray computed tomography. PhD thesis. Hokkaido University, Japan.

Nardi A, Idiart A, Trinchero P, de Vries L M, Molinero J, 2014. Interface COMSOL-PHREEQC (iCP), an efficient numerical framework for the solution of coupled multiphysics and geochemistry. Computers & Geosciences 69, 10–21.

Neaman A, Guillaume D, Pelletier M, Villiéras F, 2003. The evolution of textural properties of Na/Ca-bentonite following hydrothermal treatment at 80 and 300 °C in the presence of Fe and/or Fe oxides. Clay Minerals 38, 213–223.

Neretnieks I, 2014. Development of a simple model for the simultaneous degradation of concrete and clay in contact. Applied Geochemistry 43, 101–113.

Ochs M, Talerico C, 2004. SR-Can. Data and uncertainty assessment. Migration parameters for the bentonite buffer in the KBS-3 concept. SKB TR-04-18, Svensk Kärnbränslehantering AB.

Oda C, Walker C, Chino D, Ichige S, Honda A, Sato T, Yoneda T, 2014. Na-montmorillonite dissolution rate determined by varying the Gibbs free energy of reaction in a dispersed system and its application to a coagulated system in 0.3 M NaOH solution at 70 °C. Applied Clay Science 93–94, 62–71.

Olmeda J, Henocq P, Giffaut E, Grivé M, 2017. Modelling of chemical degradation of blended cement-based materials by leaching cycles with Callovo-Oxfordian porewater. Physics and Chemistry of the Earth, Parts A/B/C 99, 110–120.

Parkhurst D L, Appelo C A J, 2013. Description of input and examples for PHREEQC Version 3 – A computer program for speciation, batch-reaction, one-dimensional transport, and inverse geochemical calculations. Techniques and Methods 6–A43, U.S. Geological Survey, Denver, Colorado.

Parkhurst D L, Kipp K L, Charlton S R, 2010. PHAST version 2: a program for simulating ground-water flow, solute transport, and multicomponent geochemical reactions. Techniques and Methods 6–A35, U.S. Geological Survey, Denver, Colorado.

Pękala M, Olmeda J, Grivé M, Bruno J, 2015 . Assessment of Redox State and its Impact on the Solubility and Speciation of Selected Radionuclides in the SFL Repository. SKBdoc 1533627 ver 1.0, Svensk Kärnbränslehantering AB.

Read D, Glasser F P, Ayora C, Guardiola M T, Sneyers A, 2001. Mineralogical and microstructural changes accompanying the interaction of Boom Clay with ordinary Portland cement. Advances in Cement Research 13, 175–183.

Rozalén M L, Huertas F J, Brady P V, Cama J, García-Palma S, Linares J, 2008. Experimental study of the effect of pH on the kinetics of montmorillonite dissolution at 25 °C. Geochimica et Cosmochimica Acta 72, 4224–4253.

Rozalén M L, Huertas F J, Brady P V, 2009. Experimental study of the effect of pH and temperature on the kinetics of montmorillonite dissolution. Geochimica et Cosmochimica Acta 73, 3752–3766.

Sato T, Oda C, 2015. Kinetics of smectite dissolution at high pH conditions for long-term safety assessment of radioactive waste disposal: effect of Gibbs free energy and secondary minerals. In Proceedings of International Conference on Clay Science and Technology (EUROCLAY 2015), Edinburgh, UK, 6 July 2015.

Sato T, Kuroda M, Yokoyama S, Tsutsui, M, Fukushi K, Tanaka T, Nakayama S, 2004. Dissolution mechanism and kinetics of smectite under alkaline conditions. In Proceedings of International Workshop on Bentonite–Cement Interaction in Repository Environments, Tokyo, 14–16 April 2004. A3-38.

Satoh H, Ishii T, Owada H, 2013. Dissolution of compacted montmorillonite at hyperalkaline pH and 70 °C: in situ VSI and ex situ AFM measurements. Clay Minerals 48, 285–294.

Savage D, Benbow S, 2007. Low pH Cements. SKI Report 2007:32, Swedish Nuclear Power Inspectorate.

Savage D, Noy D J, Mihara M, 2002. Modelling the interaction of bentonite with hyperalkaline fluids. Applied Geochemistry 17, 207–223.

Savage D, Walker C, Arthur R, Rochelle C, Oda C, Takase H, 2007. Alteration of bentonite by hyperalkaline fluids: a review of the role of secondary minerals. Physics and Chemistry of the Earth, Parts A/B/C 32, 287–297.

Savage D, Arthur R, Watson, C, Wilson J, 2010. An evaluation of models of bentonite pore water evolution. SSM Report 2010:12, Swedish Radiation Safety Authority.

Sena C, Salas J, Arcos D, 2010. Aspects of geochemical evolution of the SKB near field in the frame of SR-Site. SKB TR-10-59, Svensk Kärnbränslehantering AB.

Sidborn M, Marsic N, Crawford J, Joyce S, Hartley L, Idiart A, de Vries L M, Maia F, Molinero J, Svensson U, Vidstrand P, Alexander R, 2014. Potential alkaline conditions for deposition holes of a repository in Forsmark as a consequence of OPC grouting. SKB R-12-17, Svensk Kärnbränslehantering AB.

SKB, 2011. Long-term safety for the final repository for spent nuclear fuel at Forsmark. Main report of the SR-Site project. SKB TR-11-01, Svensk kärnbränslehantering AB.

SKB, 2019. Initial state report for the repository for the safety evaluation SE-SFL. SKB TR-19-03, Svensk Kärnbränslehantering AB.

Soler J M, 2013. Reactive transport modeling of concrete-clay interaction during 15 years at the Tournemire Underground Rock Laboratory. European Journal of Mineralogy 25, 639–654.

Soler J M, 2016. Two-dimensional reactive transport modeling of the alteration of a fractured limestone by hyperalkaline solutions at Maqarin (Jordan). Applied Geochemistry 66, 162–173.

Soler J M, Mäder U K, 2010. Cement–rock interaction: Infiltration of a high-pH solution into a fractured granite core. Geologica Acta 8, 221–233.

Soler J M, Vuorio M, Hautojärvi A, 2011. Reactive transport modeling of the interaction between water and a cementitious grout in a fractured rock. Application to ONKALO (Finland). Applied Geochemistry 26, 1115–1129.

Soler J M, Watson C, Wilson J, Wakiya A, Oda C, Akagi Y, Honda A, Walker C, Savage D, Rüedi J, Giroud N, 2014. LCS: NA modelling report – Tournemire. NAB 13-91, Nagra, Switzerland.

Sverdrup H, Warfvinge P, 1995. Estimating field weathering rates using laboratory kinetics. Reviews in Mineralogy 31, 485–542.

Terada K, Tani A, Harada S, Satoh H, Hayashi D, 2019. Monte Carlo analysis of montmorillonite particle structures and modeling of dissolution rate reduction. Materials Research Express 6, 035514. doi:10.1088/2053-1591/aaf829

Tournassat C, Neaman A, Villieras F, Bosbach D, Charlet L, 2003. Nanomorphology of montmorillonite particles: estimation of the clay edge sorption site density by low-pressure gas adsorption and AFM observations. American Mineralogist 18, 1989–1995.

Tournassat C, Steefel C I, Bourg I C, Bergaya F (eds), 2015. Natural and engineered clay barriers. Amsterdam: Elsevier. (Developments in Clay Science 6)

Tournassat C, Davis J A, Chiaberge C, Grangeon S, Bourg I C, 2016. Modeling the acid–base properties of montmorillonite edge surfaces. Environmental Science & Technology 50, 13436–13445.

Trotignon L, Peycelon H, Bourbon X, 2006. Comparison of performance of concrete barriers in a clayey geological medium. Physics and Chemistry of the Earth, Parts A/B/C 31, 610–617.

Watson C, Benbow S J, Savage D, 2007. Modelling the interaction of low pH cements and bentonite issues affecting the geochemical evolution of repositories for radioactive waste. SKI Report 2007:30, Swedish Nuclear Power Inspectorate.

Watson C, Hane K, Savage D, Benbow S, Cuevas J, Fernández R, 2009. Reaction and diffusion of cementitious water in bentonite: results of 'blind' modelling. Applied Clay Science 45, 54–69.

Watson C, Savage D, Wilson J, Benbow S, Walker C, Norris S, 2013. The Tournemire industrial analogue: reactive-transport modelling of a cement–clay interface. Clay Minerals 48, 167–184.

Yamaguchi T, Sakamoto Y, Akai M, Takazawa M, Iida Y, Tanaka T, Nakayama S, 2007. Experimental and modeling study on long-term alteration of compacted bentonite with alkaline groundwater. Physics and Chemistry of the Earth, Parts A/B/C 32, 298–310.

Yokoyama S, Kuroda M, Sato T, 2005. Atomic force microscopy study of montmorillonite dissolution under highly alkaline conditions. Clays and Clay Minerals 53, 147–154.

Appendix A

Saturation indices for bentonite and concrete porewaters

Table A-1. Saturation indices (SI) for bentonite and concrete porewater compositions used for the full reference case and the equilibrium constants (log K) of the mineral reactions written as the dissolution of 1 mole of mineral.

Mineral	SI bentonite porewater	SI concrete porewater	log K	Dissolution reactions used to calculate solubility products (log K)
Montmorillonite	−1.05	−18.40	2.20	$Ca_{0.17}Mg_{0.34}Al_{1.66}Si_4O_{10}(OH)_2$ à $0.17Ca^{+2} + 0.34Mg^{+2} + 1.66Al^{+3} - 6H^+ + 4H_4(SiO_4) - 4H_2O$
Illite	−1.50	−11.18	9.69	$K_{0.85}Mg_{0.25}Al_{2.35}Si_{3.4}O_{10}(OH)_2$ à $0.25Mg^{+2} + 0.85K^+ + 2.35Al^{+3} - 8.4H^+ + 3.4H_4(SiO_4) - 1.6H_2O$
Calcite	0	−2.00	−8.48	$CaCO_3$ à $Ca^{2+} + CO3^{2-}$
Quartz	0	−3.74	−3.74	SiO2 à $H_4(SiO_4) - 2H_2O$
Gypsum	0	−3.57	−4.61	$CaSO_4 \cdot 2H_2O$ à $Ca^{2+} + SO_4^{2-} + 2H_2O$
Feldspar	−1.39	−11.49	2.74	$NaAlSi^3O^8$ à $Na^+ + Al^{+3} - 4H^+ + 3H_4(SiO_4) - 4H_2O$
Portlandite	−11.34	0	22.81	$Ca(OH)_2$ à $Ca^{+2} - 2H^+ + 2H_2O$
CSH 1.6	−13.06	0	28.00	$Ca_{1.6}SiO_{3.6} \cdot 2.58H_2O$ à $1.6Ca^{+2} - 3.2H^+ + H_4(SiO_4) + 2.18H_2O$
CSH 1.2	−9.00	−0.47	19.30	$Ca_{1.2}SiO_{3.2} \cdot 2.06H_2O$ à $1.2Ca^{+2} - 2.4H^+ + H_4(SiO_4) + 1.26H_2O$
CSH 0.8	−5.40	−1.41	11.05	$Ca_{0.8}SiO_{2.8} \cdot 1.54H_2O$ à $0.8Ca^{+2} - 1.6H^+ + H_4(SiO_4) + 0.34H_2O$
Illite-Al	−0.81	−10.33	10.13	$K_{0.85}Al_{2.85}Si_{3.15}O_{10}(OH)_2$à $0.85K^+ + 2.85Al^{+3} - 9.4H^+ + 3.15H_4(SiO_4) - 0.6H_2O$
Analcime	−1.73	−6.58	6.65	$Na_{0.99}Al_{0.99}Si_{2.01}O_6 \cdot H2O$ à $0.99Na^+ + 0.99Al^{+3} - 3.96H^+ + 2.01H_4(SiO_4) - 1.04H_2O$
Heulandite-Ca	−2.40	−25.55	2.46	$Ca_{1.07}Al_{2.14}Si_{6.86}O_{18} \cdot 6.17H_2O$à $1.07Ca^{+2} + 2.14Al^{+3} - 8.56H^+ + 6.86H_4(SiO_4) - 3.27H_2O$
Heulandite-Na	−1.42	−25.28	2.80	$Na_{2.14}Al_{2.14}Si_{6.86}O_{18} \cdot 6.17H_2O$ à $2.14Na^+ + 2.14Al^{+3} - 8.56H^+ + 6.86H_4(SiO_4) - 3.27H_2O$
Clinoptilolite-Ca	−2.87	−21.75	−2.35	$Ca_{0.55}(Si_{4.9}Al_{1.1})O_{12} \cdot 3.9H_2O$ à $0.55Ca^{+2} + 1.1Al^{+3} - 4.4H^+ + 4.9H_4(SiO_4) - 3.7H_2O$
Clinoptilolite-Na	−4.46	−23.69	−0.09	$Na_{1.1}(Si_{4.9}Al_{1.1})O_{12} \cdot 3.5H_2O$ à $1.1Na^+ + 1.1Al^{+3} - 4.4H^+ + 4.9H_4(SiO_4) - 4.1H_2O$
Brucite	−5.79	−1.74	17.10	$Mg(OH)_2$ à $Mg^{+2} - 2H^+ + 2H_2O$
C_3AH_6	−33.59	0	80.32	$Ca_3Al_2(OH)_{12}$ à $3Ca^{+2} + 2Al^{+3} - 12H^+ + 12H_2O$
C_4AH_{13}	−45.06	−0.14	103.65	$Ca_4Al_2(OH)_{14} \cdot 6H_2O$ à $4Ca^{+2} + 2Al^{+3} - 14H^+ + 20H_2O$
Ettringite	−22.88	0	56.97	$Ca_6Al_2(SO_4)_3(OH)_{12} \cdot 26H_2O$ à $6Ca^{2+} + 2Al^{+3} - 12H^+ + 3SO_4^{2-} + 38H_2O$
Hydrotalcite	−15.79	0	73.74	$Mg_4Al_2(OH)_{14} \cdot 3H_2O$ à $4Mg^{+2} + 2Al^{+3} - 14H^+ + 17H_2O$
Hydrotalcite C	−12.92	−10.88	50.86	$Mg_4Al_2(OH)_{12}CO_3 \cdot 2H_2O$ à $4Mg^{+2} + 2Al^{+3} - 12H^+ + CO_3^{-2} + 14H_2O$
Monocarboaluminate	−31.58	0	70.30	$(CaO)_3Al_2O_3{:}CaCO_3 \cdot 10.68H_2O$ à $4Ca^{+2} + 2Al^{+3} - 12H^+ + CO_3^{-2} + 16.680H_2O$
Monosulphoaluminate	−30.68	−0.66	73.07	$Ca_4Al_2(S\_siO_4)(OH)_{12} \cdot 6H_2O$ à $4Ca^{+2} + 2Al^{+3} - 12H^+ + SO_4^{-2} + 18H_2O$
Strätlingite	−17.94	−0.77	49.66	$Ca_2Al_2SiO_3(OH)_8 \cdot 4H_2O$ à $2Ca^{+2} + 2Al^{+3} - 10H^+ + H_4(SiO_4) + 11H_2O$
Syngenite	−5.06	−6.91	−7.45	$K_2Ca(S\_siO_4)_2 \cdot 6H_2O$ à $1Ca^{+2} + 2K^+ + 2SO_4^{-2} + 6H_2O$

Mineral	SI bentonite porewater	SI concrete porewater	log K	Dissolution reactions used to calculate solubility products (log K)
Saponite-Ca	−6.68	−11.25	31.21	$Ca_{0.17}Mg_3Al_{0.34}Si_{3.66}O_{10}(OH)_2$ à $0.17Ca^{+2} + 3Mg^{+2} + 0.34Al^{+3} - 7.36H^+ + 3.66H_4(SiO_4) - 2.640H_2O$
Saponite-Na	−4.83	−9.50	29.64	$Na_{0.34}Mg_3Al_{0.34}Si_{3.66}O_{10}(OH)_2$ à $3Mg^{+2} + 0.34Na^+ + 0.34Al^{+3} - 7.36H^+ + 3.66H_4(SiO_4) - 2.640H_2O$
Saponite-K	−4.83	−8.49	28.94	$K_{0.34}Mg_3Al_{0.34}Si_{3.66}O_{10}(OH)_2$ à $3Mg^{+2} + 0.34K^+ + 0.34Al^{+3} - 7.36H+ + 3.66H_4(SiO_4) - 2.64H_2O$
Saponite-Mg	−6.91	−12.71	31.93	$Mg_{0.17}Mg_3Al_{0.34}Si_{3.66}O_{10}(OH)_2$ à $3.17Mg^{+2} + 0.34Al^{+3} - 7.36H^+ + 3.66H_4(SiO_4) - 2.64H_2O$
Phillipsite-Ca	−1.57	−11.34	2.32	$Ca_{0.5}AlSi_3O_8 \cdot 3H_2O$ à $0.5Ca^{+2} + Al^{+3} - 4H^+ + 3H_4(SiO_4) - H_2O$
Phillipsite-Na	−0.00	−10.10	1.45	$NaAlSi_3O_8 \cdot 3H_2O$ à $Na^+ + Al^{+3} - 4H^+ + 3H_4(SiO_4) - H_2O$
$SiO_{2(am)}$	−1.08	−6.16	−2.71	SiO_2 à $H_4SiO_4 - 2H_2O$
Clinochlore	−3.45	1.16	61.72	$Mg_5Al_2Si_3O_{10}(OH)_8$ à $5Mg^{+2} + 2Al^{+3} - 16H^+ + 3H_4(SiO_4) + 6H_2O$
Jennite	−64.75	6.82	147.33	$Ca_9Si_6O_{16}(OH)_{10} \cdot 6(H_2O)$ à $9Ca^{+2} - 18H^+ + 6H4(SiO_4) + 8H_2O$
Tobermorite	−26.73	−0.51	62.94	$Ca_5Si_6O_{16.5}(OH) \cdot 10H_2O$ à $5Ca^{+2} - 10H^+ + 6H4(SiO_4) + 3.5H_2O$
Gyrolite	−10.17	−2.73	22.34	$Ca_2Si_3O_{7.5}(OH) \cdot 2H_2O$ à $2Ca^{+2} - 4H^+ + 3H_4(SiO_4) - 1.5H_2O$
Hillebrandite	−17.62	−0.02	36.95	$Ca_2SiO_3(OH)_2 \cdot 0.17H_2O$ à $2Ca^{+2} - 4H^+ + H_4(SiO_4) + 1.17H_2O$
Foshagite	−30.82	−0.70	65.96	$Ca_4Si_3O_9(OH)_2 \cdot 0.5H_2O$ à $4Ca^{+2} - 8H^+ + 3H_4(SiO_4) - 0.5H_2O$
Okenite	−4.93	−3.75	9.18	$CaSi_2O_5 \cdot 2H_2O$ à $Ca^{+2} - 2H^+ + 2H_4(SiO_4) - H_2O$
Gismondine	−5.88	−4.36	39.01	$Ca_2Al_4Si_4O_{16} \cdot 9H_2O$ à $2Ca^{+2} + 4Al^{+3} - 16H^+ + 4H_4(SiO_4) + 9H_2O$
Scolecite	−3.96	−8.28	16.65	$CaAl_2Si_3O_{10} \cdot 3H_2O$ à $Ca^{+2} + 2Al^{+3} - 8H^+ + 3H_4(SiO_4) + H_2O$
Wairakite	−5.66	−15.05	14.44	$CaAl_2Si_4O_{12} \cdot 2H_2O$ à $Ca^{+2} + 2Al^{+3} - 8H^+ + 4H_4(SiO_4) - 2H_2O$
Stilbite	−11.06	−50.10	23.05	$NaCa_2(Al_5Si_{13})O_{36} \cdot 16H_2O$ à $2Ca^{+2} + Na^+ + 5Al^{+3} - 20H^+ + 13H_4(SiO_4)$
Natrolite	−5.37	−10.35	19.33	$Na_2(Al_2Si_3)O_{10} \cdot 2H_2O$ à $2Na^+ + 2Al^{+3} - 8H^+ + 3H_4(SiO_4)$
Mordenite Ca	−3.51	−23.12	−4.16	$Ca_{0.289}Na_{0.362}Al_{0.94}Si_{5.06}O_{12} \cdot 3.47H_2O$ à $0.29Ca^{+2} + 0.36Na^+ + 0.94Al^{+3} - 3.76H^+ + 5.06H_4(SiO_4) - 4.77H_2O$

Appendix B

Model comparison with Cronstrand (2016)

Table B-1. Simulation cases used as complementary validation of the implementation of the reactive transport models, comparison with simulation results from Cronstrand (2016).

Model Description	D_e (m^2/s)	Reactive Surface Area (m^2/g)	Mineral assemblage	Left boundary condition	Right boundary condition
Fresh cementitious porewater	5.0×10^{-11}	800	Cronstrand (2016)	SFR groundwater	Fresh cementitious water

Table B-2. List of minerals included in each of the simulation cases, taken from Cronstrand (2016).

Albite	Illite
Analcime	Kaolinite
Brucite	Phillipsite Ca
Chalcedony	Phillipsite K
Dolomite	Phillipsite Na
Gibbsite	Portlandite
Goethite	Saponite Ca
Gypsum	Saponite K
Gyrolite	Saponite Na
Heulandite	Tobermorite

- Boundary conditions and secondary minerals are in agreement with Cronstrand (2016).
- Differences compared to Cronstad (2016): primary minerals, thermodynamic database used (here ThermoChimie 9b versus Thermoddem) and assumed dissolution rates (here Sato-Oda versus Rozalén et al. 2008).

A qualitative comparison of the results for the case considering a fresh cement water boundary condition is shown in Figure B-1. It may be observed that the results are qualitatively in good agreement, with similar montmorillonite dissolution depths.

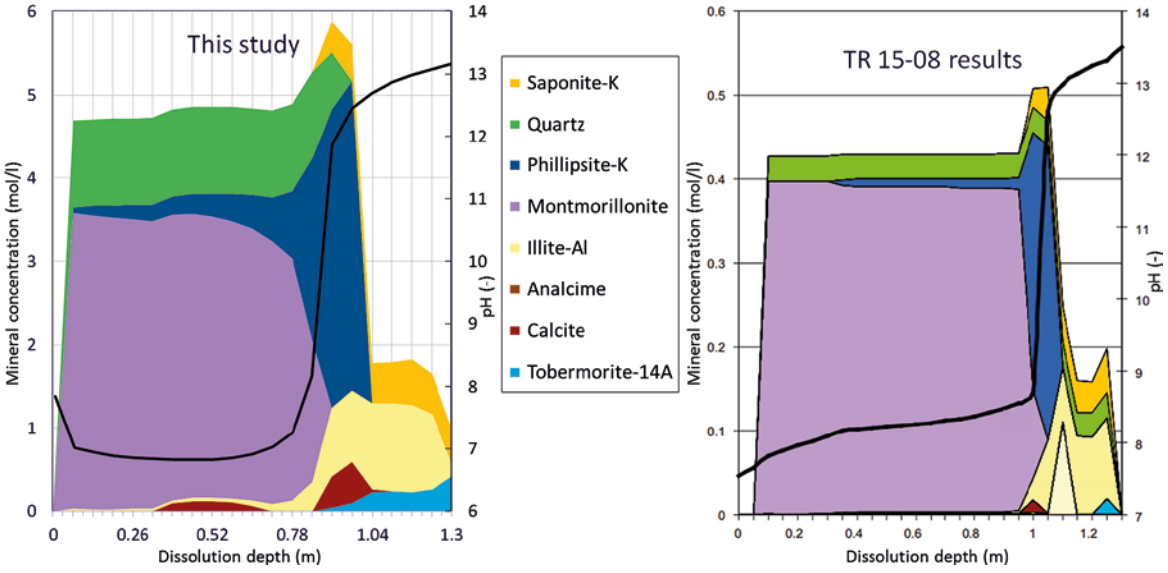

Figure B-1. Qualitative comparison between spatial mineral phase concentration profiles (mol/litre of medium) after 3 000 years from the reactive transport model proposed by Cronstrand (2016) (right, Figure 4-6 from Cronstrand 2016) and the similar model used in this study (left).

Appendix C

Results of sensitivity cases

This appendix includes additional results to those presented in Section 7 of some simulation cases corresponding to the full analysis (concrete–bentonite interaction).

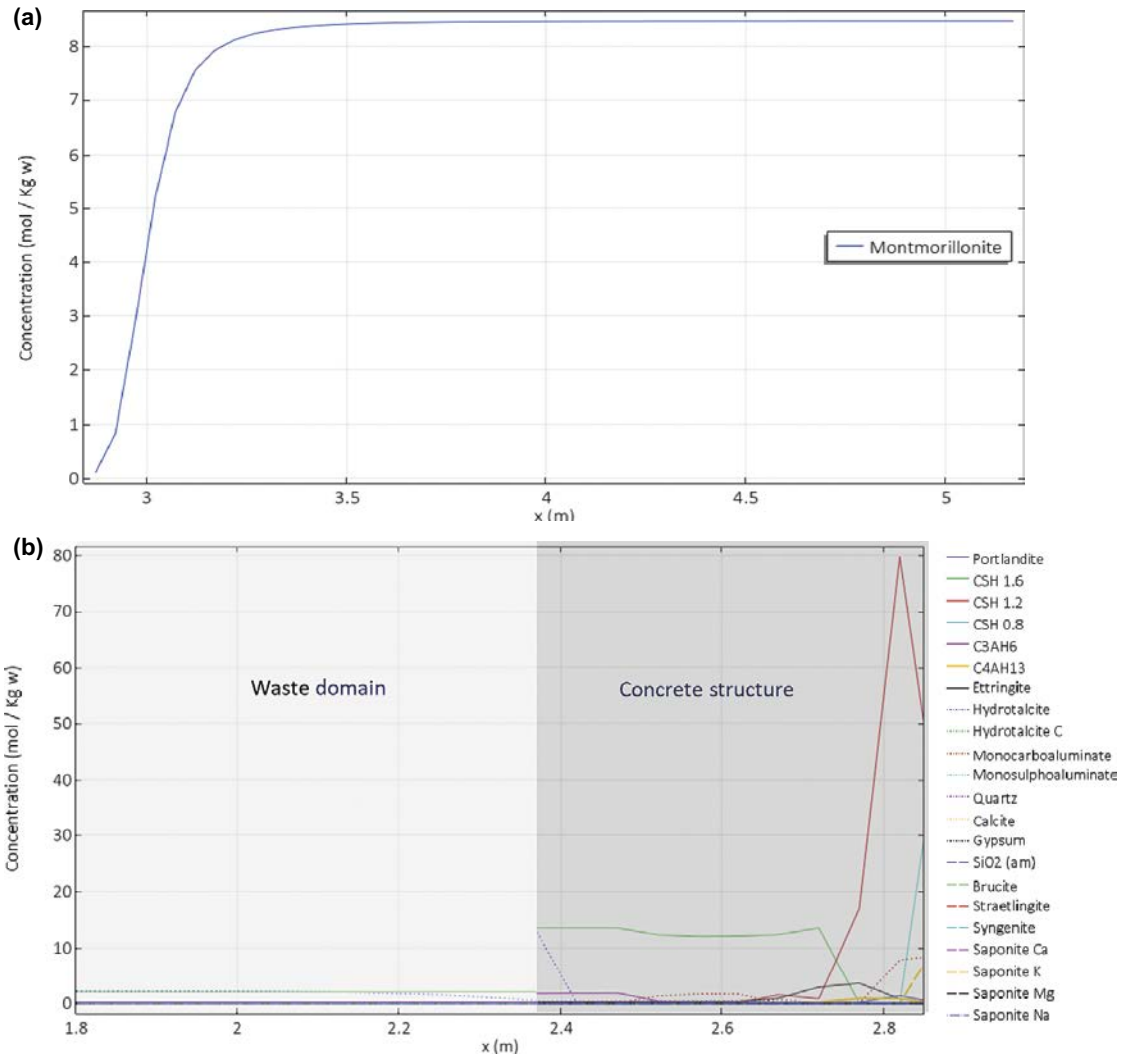

Figure C-1. *Results of the idealized case, case 13 (only montmorillonite): mineral phase spatial concentration profiles (mol/kgw) after 100 000 years in (a) the bentonite backfill and (b) the cementitious domains.*

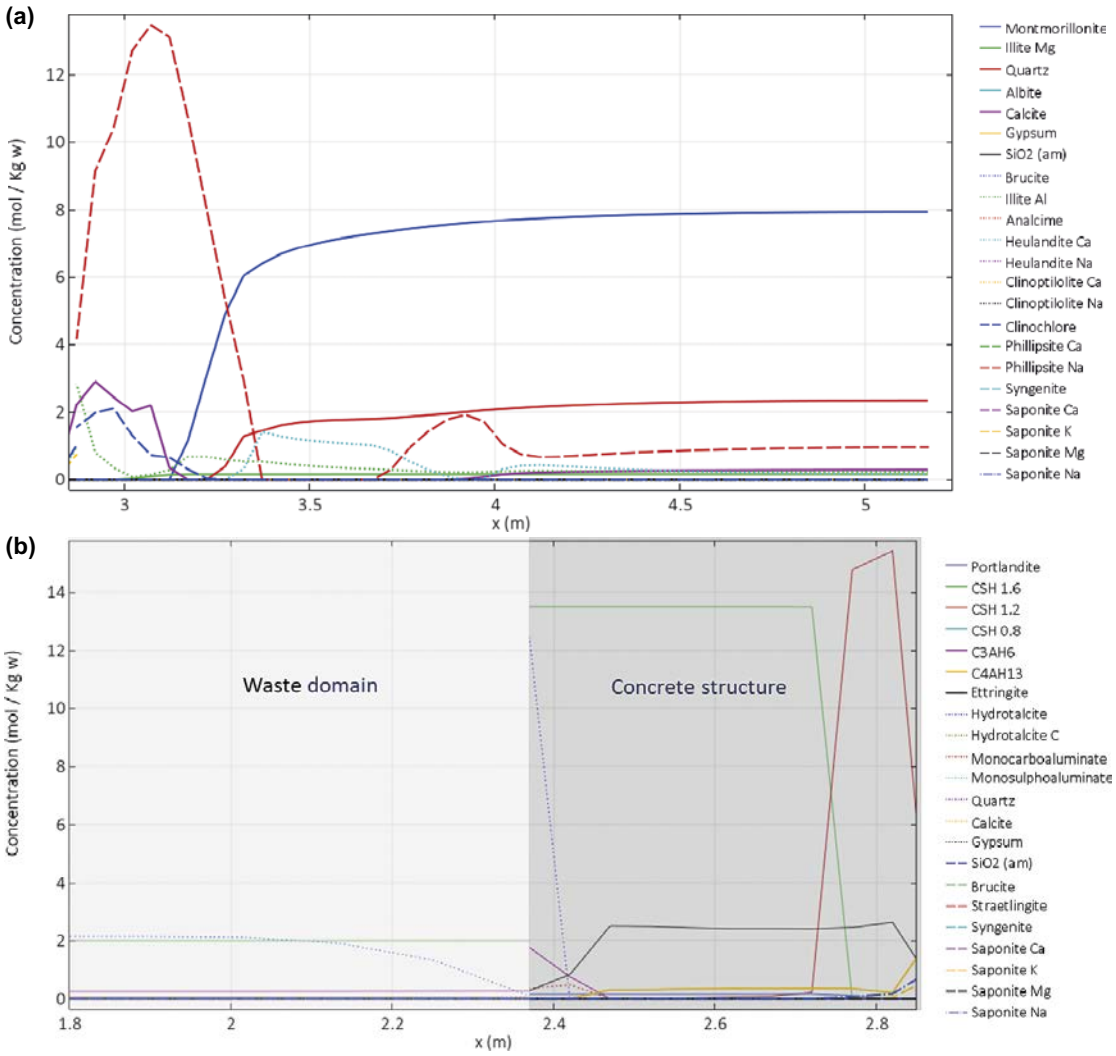

Figure C-2. *Results of case 18 (alkali-leached concrete): mineral phase spatial concentration profiles (mol/kgw) after 100 000 years in (a) the bentonite backfill and (b) the cementitious domains.*

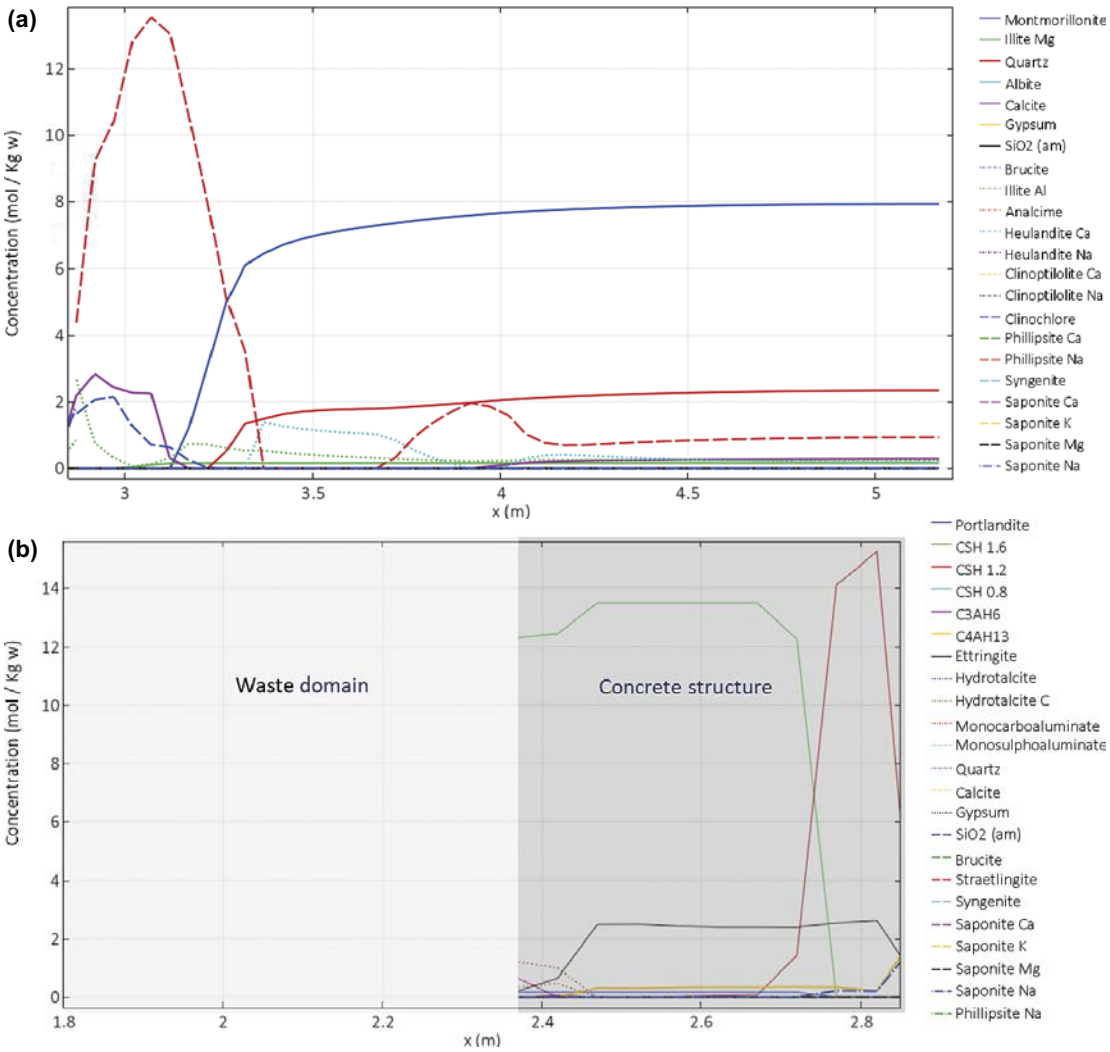

Figure C-3. *Results of case 19 (no waste domain): mineral phase spatial concentration profiles (mol/kgw) after 100 000 years in (a) the bentonite backfill and (b) the cementitious domains.*

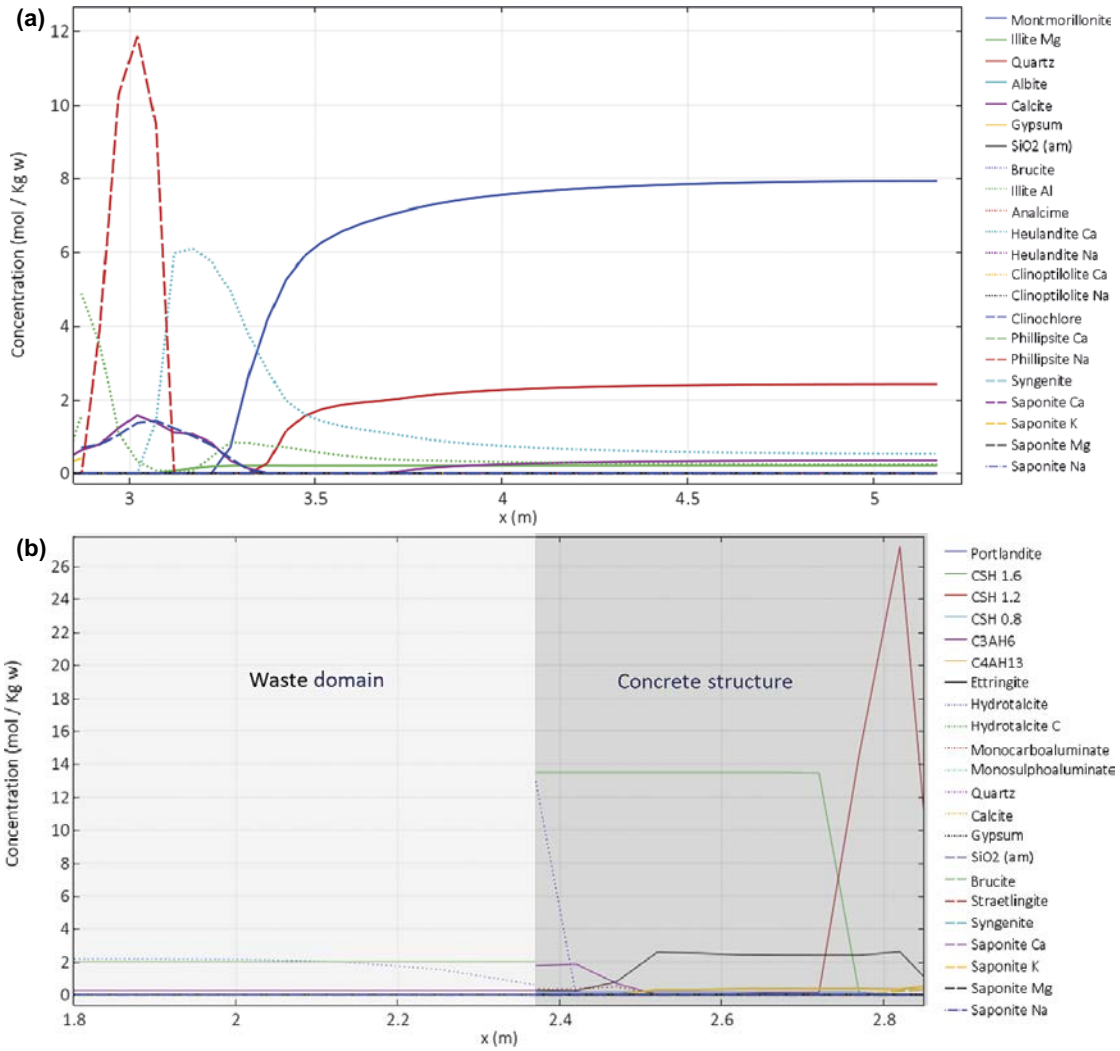

Figure C-4. *Results of case 20 (no bentonite exchanger): mineral phase spatial concentration profiles (mol/kgw) after 100 000 years in (a) the bentonite backfill and (b) the cementitious domains.*

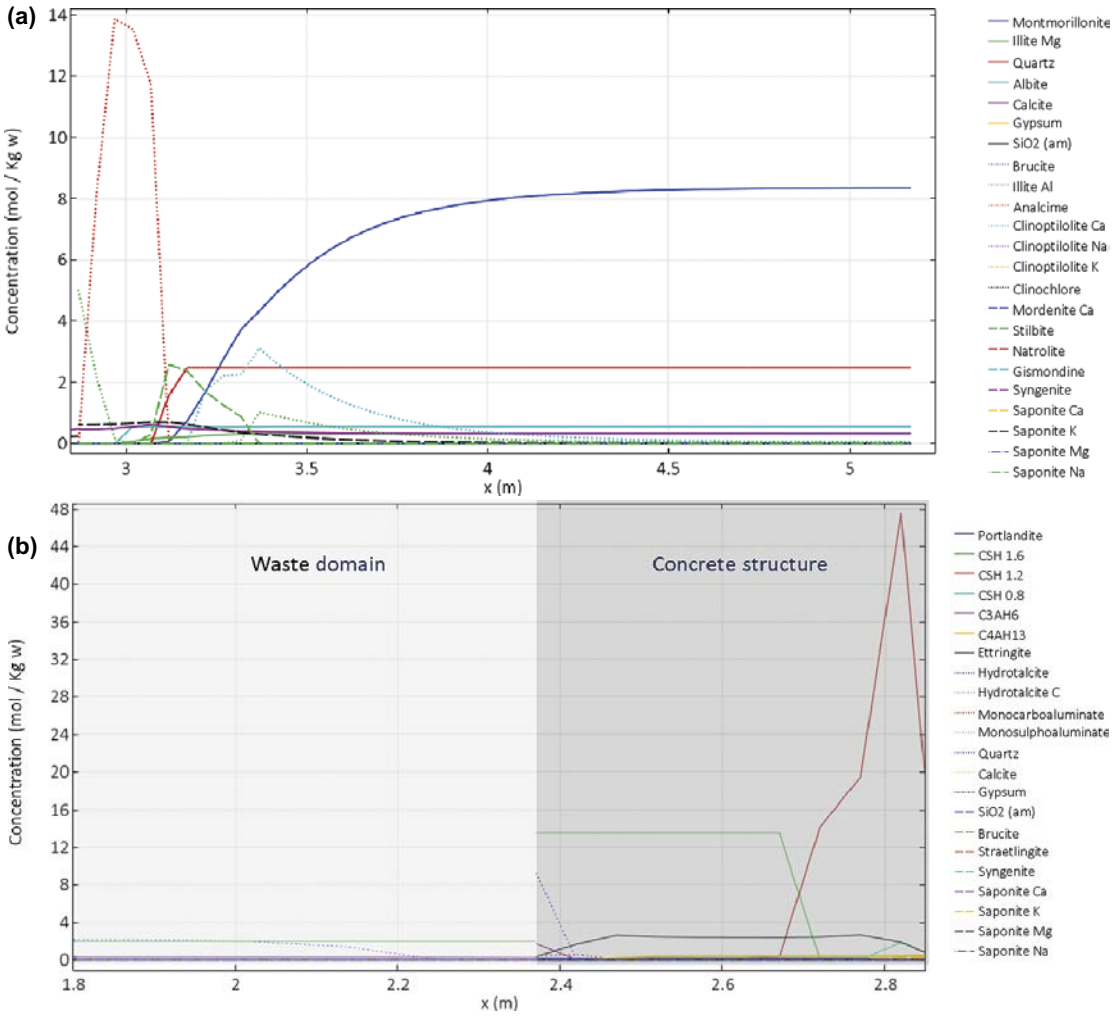

Figure C-5. *Results of case 21 (alternative zeolites): mineral phase spatial concentration profiles (mol/kgw) after 100 000 years in (a) the bentonite backfill and (b) the cementitious domains.*

Appendix D

Mass balance of hydroxyl ions

Table D-1. Mass balance (moles) of hydroxyl ions in the dissolution of 1 mol of montmorillonite and the precipitation of different zeolites using ThermoChimie v9b. The speciation of Al and Si considered in the calculation corresponds to the relevant species under alkaline conditions (pH > 10): Al(OH)4− for Al (1.0Al3+ − 4.0H+ + 4.0H2O = Al(OH)4−), and H3(SiO4)− for Si (1.0H4(SiO4) − 1.0H+ = H3(SiO4)−).

Zeolite	Ca^{2+}	Na^{+}	Al^{3+}	H^{+}	$H_4(SiO_4)$	H_2O	OH^- per mol of zeolite formed*	OH^- per mol of montmorillonite dissolved*
Analcime		0.99	0.99	−3.96	2.01	1.04	2.01	−1.27
Heulandite_Ca	1.07		2.14	−8.56	6.86	−3.27	6.86	0.68
Heulandite_Na		2.14	2.14	−8.56	6.86	−3.27	6.86	0.68
Phillipsite_Ca	0.5		1	−4	3	−1	3	0.34
Phillipsite_Na		1	1	−4	3	−1	3	0.34
Clinoptilolite_Ca	0.55		1.1	−4.4	4.9	−3.7	4.9	2.75
Clinoptilolite_Na		1.1	1.1	−4.4	4.9	−3.7	4.9	2.75
Mordenite_Ca	0.515		1.03	−4.12	4.97	−4.78	4.97	3.37
Stilbite	2	1	5	−20	13		13	−0.32
Natrolite		2	2	−8	3		3	−2.15
Zeolite_CaP	2		4	−16	4	9	4	−2.98

* Negative values indicate consumption of OH^- ions, while positive values mean release of OH^- ions.

Arkitektkopia AB, Bromma, 2020

SKB is responsible for managing spent nuclear fuel and radioactive waste produced by the Swedish nuclear power plants such that man and the environment are protected in the near and distant future.

skb.se